Neutron-Deuteron Elastic Scattering and the Three-Nucleon Force

by

Maxim B. Chtangeev

B. S. in Physics Northwest Nazarene University, June 1999

Submitted to the Department of Physics
in partial fulfillment of the requirements for the degree of

Master of Science

at the

MASSACHUSETTS INSTITUTE OF TECHNOLOGY

June 2005

Signature of Author ....
Department of Physics
May 11, 2005

Certified by ....
June L. Matthews
Professor of Physics
Thesis Supervisor

Accepted by ....
Thomas J. Greytak
Professor of Physics
Associate Department Head for Education

Neutron-Deuteron Elastic Scattering and the Three-Nucleon Force

by

Maxim B. Chtangeev

Submitted to the Department of Physics
on May 11, 2005, in partial fulfillment of the
requirements for the degree of
Master of Science

Abstract

The differential cross section for neutron-deuteron elastic scattering was measured at six angles over the center-of-mass angular range 65° - 130° and incident neutron energies 140 - 240 MeV at the LANSCE/WNR facility of the Los Alamos National Laboratory. Witala *et al.* (H. Witala *et al.*), Phys. Rev. Lett. 81, 1183 (1998) have suggested that the differential cross section for nucleon-deuteron scattering at large angles may be sensitive to the presence of a three-nucleon force. In the present experiment, a liquid deuterium target was exposed to the pulsed neutron beam, with incident neutron energy determined by time of flight. Scattered neutrons, detected by a horizontal array of plastic scintillator bars, and recoil deuterons, detected by Δ E-E (plastic scintillator – CsI) telescopes, were observed in coincidence. The resulting angular distributions for several incident neutron energies are compared with theoretical predictions and previous measurements in both nd and pd systems.

Thesis Supervisor: June L. Matthews
Title: Professor of Physics

Acknowledgments

Throughout my graduate work at MIT I have been surrounded by some of the most knowledgeable and generous people. Their guidance and support proved essential to the success of my studies in general and this experimental work in particular. I feel honored to be the one presenting the findings of this group fully realizing that it is only through the expertise of its members and their generous contributions that this measurement and this document have been completed. It has been my great pleasure to work among them and I appreciate the opportunity to give them thanks.

Taylan Akdoğan: Thank you for your sincere desire to help, be it in deriving the Jacobian for an interaction with a three body final state or coming back to the lab at night to give me a ride to the hotel. Your insightful comments and suggestions have encouraged me to work harder, to look deeper. Thank you for your friendship. **Art Bridge:** Thank you for keeping our refrigeration system going year after year, for coming to the lab on weekends to check on the target and for always remembering to restock our supply of nitrogen. **Bill Franklin:** Thank you for your expert advice on experimental techniques and data analysis. You taught me how to extract the most information from the available data. **Joanne Gregory:** Thank you for allowing me to concentrate on my studies without worrying about the airplane tickets, hotel reservations, payroll reimbursements, etc. **Michael Kovash:** Thank you for contributing the neutron detectors for use in this experiment, for teaching me how best to troubleshoot electronics problems, and for offering suggestions on how to resolve the questions I faced during the data analysis. **June Matthews:** I appreciate your expert guidance and flexibility which enabled me to take advantage of multiple opportunities such as presenting, teaching, and contributing to several research projects. Thank you for your time and patience. **Yaşar Safkan:** Thank you for your help with my classes, for your encouragement and for the example of your enthusiastic approach to nuclear physics and computer games. **Mark Yuly:** Your love of nuclear physics has influenced me to pursue a graduate degree in this field. Your high standard of academic performance has kept me trying to do my best in both graduate and undergraduate studies. Your friendship has helped me through the tougher sides of school and has enriched my life. Thank you.

Finally, I would like to thank my wife Diane and our kids Corey and Ashley for their encouragement and for enabling me to concentrate on this work by taking on my share of family responsibilities. I am so fortunate to have your love and support, thank you.

To Diane, Corey and Ashley

Contents

List of Figures

List of Tables

Chapter 1

Introduction

The differential cross section for neutron-deuteron elastic scattering was measured at six angles over the center-of-mass angular range 65° - 130° and incident neutron energies 140 - 240 MeV at the LANSCE/WNR facility of the Los Alamos National Laboratory. Witala *et al.* (H. Witala *et al.*), Phys. Rev. Lett. 81, 1183 (1998) have suggested that the differential cross section for nucleon-deuteron scattering at large angles may be sensitive to the presence of a three-nucleon force. In the present experiment, a liquid deuterium target was exposed to the pulsed neutron beam, with incident neutron energy determined by time of flight. Scattered neutrons, detected by a horizontal array of plastic scintillator bars, and recoil deuterons, detected by Δ E-E (plastic scintillator – CsI) telescopes, were observed in coincidence. The resulting angular distributions for several incident neutron energies are compared with theoretical predictions and previous measurements in both nd and pd systems.

1.1 Three-Nucleon Force

Thanks to recent advances in theoretical formulations and computational techniques, today's two-nucleon (NN) potentials are remarkably consistent and describe most of the available experimental data for bound and free light nuclei quite well. Yet, an increasing amount of experimental evidence suggests that these two-nucleon potentials are unable to mimic the interactions in

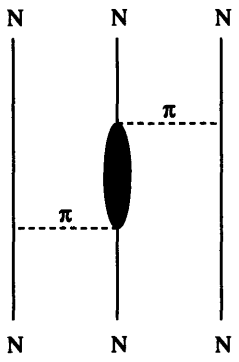

Figure 1-1: Feynman diagram of a 2π exchange model of 3NF. The mechanism of a 2π exchange between three nucleons with an intermediate Δ excitation is incorporated into both the Tucson-Melbourne parametrization (TM) [3] and the Urbana IX three-body interaction [4].

three-nucleon systems with similar degree of precision. For instance, NN only potentials underestimate ^{3}H binding energy by about 800 keV out of 8.48 MeV [1]. For scattering observables, the agreement between theory and experiment deteriorates in the region of cross section minima as one considers *n–d* and *p–d* systems at beam energies above about 60 MeV.

The inconsistencies between theory and experiment for multi-nucleon systems suggest two possibilities. On one hand, they may be an indication that modern NN forces are not yet complete and require further modifications to reconcile the disagreements. On the other hand, they may be a manifestation of new processes which arise only in the presence of three or more nucleons. The question whether the unperturbed free two-nucleon (NN) interaction is predominant or is significantly modified due to the presence of an additional nucleon has become one of the basic questions about the dynamics of three interacting nucleons.

Today, a number of three-nucleon force (3NF) models exists. Examples of the often used modern 3NF are the Tucson-Melbourne (TM) force and the Urbana IX three-body interaction. Both of these models are based on the Fujita-Miyazawa force [2] – a 2π exchange between three nucleons with an intermediate Δ excitation. Figure 1-1 shows a Feynman diagram describing this interaction. Modern computational techniques permit full-fledged Faddeev calculations which explicitly include the contributions of 3NF for three-nucleon systems.

In recent paper, Witala *et al.* published predictions for *n–d* differential cross section at energies 65, 140, and 200 MeV [5]. The calculations were performed with and without the contributions of the Tucson-Melbourne three-nucleon force. Figures 1-2 and 1-3 show the

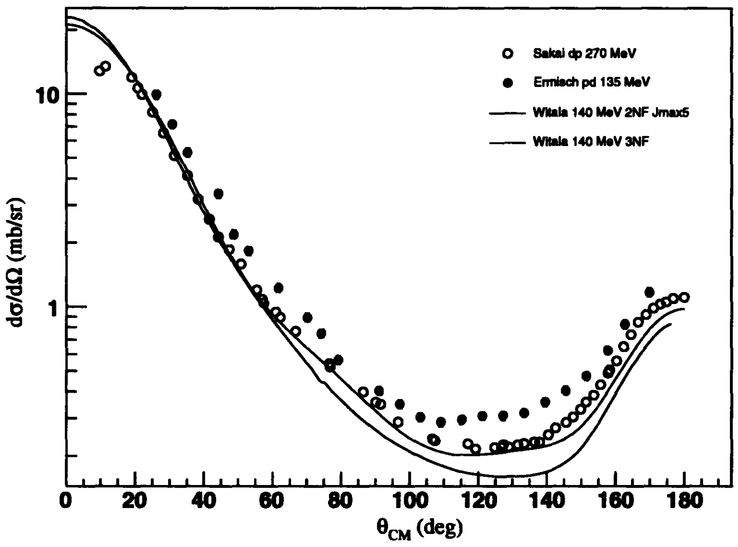

Figure 1-2: Nucleon-deuteron elastic scattering cross section for 140 MeV incident neutron energy. Solid curves show theoretical predictions with and without the 3NF effects for *n–d* elastic scattering and do not include any Coulomb contributions.

predictions and experimental results for nucleon-deuteron elastic scattering cross section at 140 and 200 MeV respectively. A comparison with existing *p–d* data revealed that predictions based on NN only forces underestimate experimental data in the minimum region of the *n–d* elastic cross section. The inclusion of the 3NF effects helped remove the discrepancy completely at some energies while only partially at others. For example, inclusion of the TM force in the calculation of *n–d* elastic cross section at 140 MeV brought theory to a good agreement with the available *d–p* data from Sakai *et al.* [6]. However, the same was not sufficient to reconcile the disagreement at 200 MeV. Furthermore, recent *p–d* data from KVI [7] disagreed with both the modified calculation and the previous data even at 140 MeV.

It is evident that additional precise measurements of *p–d* and *n–d* scattering are needed to resolve these differences.

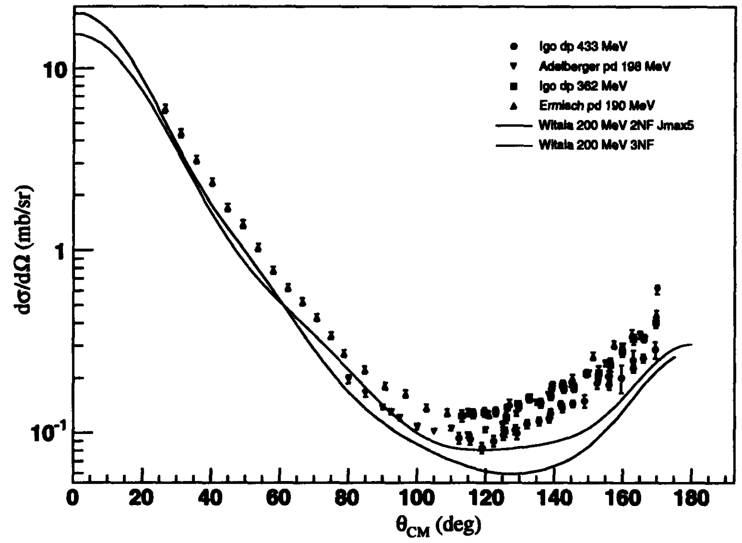

Figure 1-3: Nucleon-deuteron elastic scattering cross section for 200 MeV incident neutron energy. Solid curves show theoretical predictions with and without the 3NF effects for *n–d* elastic scattering and do not include any Coulomb contributions.

1.2 Previous Measurements

This section summarizes two of the latest published measurements of *p–d* and *d–p* scattering. These data along with others help establish an experimental basis with which to constrain current and future theoretical work. Contributing to this basis is the primary goal of the present measurement of *n–d* elastic scattering.

In 2003, K. Ermisch *et al.* [7] published high quality results of the systematic investigation of the elastic *p–d* differential cross section for incident proton energies of 108, 120, 135, 150, 170, and 190 MeV. The measurement was completed using a polarized proton beam from the superconducting cyclotron AGOR incident on mixed solid CD_2-CH_2 targets at the KVI (Kernfysisch Versneller Institute) facility in the Netherlands. The target thickness was determined by comparing the results of the simultaneously measured differential cross section for elastic *p–p* scattering to the results of NN calculations based on Nijmegen-I, Nijmegen-II, and Reid93 potentials. The big-bite spectrometer (BBS) helped to differentiate between recoil protons and deuterons which were produced in the $^2\mathrm{H}(p,pd)$ reaction. The experiment contributed high precision *p–d* differential cross section and analyzing power data with a statistical uncertainty of the order of 2% and systematic uncertainty $\lesssim 7\%$ for c.m. angles between 30° and 170° for all six incident energies. The results are in agreement with existing data sets [6, 8, 9] to within experimental uncertainties and taking into account differences in incident beam energies.

In 2000, H. Sakai *et al.* [6] obtained high precision results for the *d–p* cross section and the complete set of analyzing powers for scattering at 270 MeV incident deuteron energy. The results spanned a c.m. angular range of 10°–180°. This experiment took place at the RIKEN Accelerator Facility. Vector and tensor polarized deuteron beams of 270 MeV were incident on a solid CH_2 target. The scattered protons and deuterons were momentum analyzed using the magnetic spectrometer SMART. The $p + p$ scattering cross section was also measured and compared to the predictions of SAID to help estimate the uncertainties in the target thickness. The statistical error for the *d–p* cross section was better than ±1.3% while the systematic error was estimated to be better than 2%. H. Sakai *et al.* found that while the calculations involving NN forces only underestimate the measured cross section, the calculations which also include the Tucson-Melbourne 3NF reproduce the data quite well. It is interesting to note that the cross section results of this measurement disagree appreciably with the results for *p–d* elastic scattering at 135 MeV by E. Ermisch *et al.* [7] as seen in figure 1-2.

The results of both of these measurements are included in figures 6-12 through 6-15.

1.3 Physics Motivation

To better constrain 3NF calculations more high quality experimental data on nucleon-nucleon elastic scattering is required. While both *n–d* and *p–d* scattering observables are theoretically accessible, the *n–d* process lacks the significant complications of the Coulomb interaction and is preferred. Furthermore, it is necessary to obtain such data over a wide range of energies and angles as contributions to the *n–d* scattering amplitude from both two-nucleon and three-nucleon forces are energy dependent.

Chapter 2

Experimental Setup

2.1 Overview

This experiment was performed at the Los Alamos Neutron Science Center of the Los Alamos National Laboratory. At the WNR (Weapons Neutron Research) facility, which housed the experimental apparatus, a "white" neutron beam with energies ranging from below a few MeV up to 800 MeV was incident on a liquid deuterium target. The scattered neutron and the recoil deuteron were detected in coincidence. The recoil deuterons were detected by six charged particle telescopes, each consisting of a thin plastic ΔE counter and a CsI calorimeter, positioned at 24°, 30°, 36°, 42°, 48°, and 54°. The scattered neutrons were detected by a wall made of five plastic scintillator bars placed horizontally on their sides in a stack of five high. Four thin veto detectors completely covered the face of the resulting 50 cm × 200 cm neutron wall. These four plastic scintillators helped discriminate against charged particles which also triggered the neutron wall. The pulsed structure of the incident beam permitted the use of time of flight techniques for determination of kinetic energies of scattered neutrons and recoil deuterons. The CsI pulse height information aided in defining kinematic variables of the three body final state during the measurement of the quasielastic n–p process, while the pulse height information from neutron bars helped determine their neutron detection efficiency.

2.2 Beam Production

The mile-long LANSCE linear accelerator accelerates protons to 800 MeV before directing them into the neutron production target at the WNR. The cylindrical water-cooled target which measures 3 cm in diameter and 7.5 cm in length is suspended in a vacuum chamber. The neutrons which are produced through spallation reactions have a continuous energy spectrum, with energies ranging from below a few MeV up to 800 MeV. After all charged particles are swept away by a magnetic field, the neutrons are delivered to the experimental areas located on several flight paths via evacuated beam pipes. The experimental apparatus for the n–d elastic measurement was set up roughly 16 meters downstream from the spallation target, on flight path 15R, i.e. 15° to the right of the incident beam direction. Figure 2-1 shows a schematic view of the WNR facility. The flight path 15R is marked as "ND2002".

The beam to this flight path is controlled by two depleted Uranium shutters of 14"(Y) and 18"(X) thickness. A shutter opening of 1 in. × 1 in. was used for this experiment. To further reduce the diameter of the incident beam, fixed iron sleeves were fitted into the beam pipe. The evacuated beam pipe passed through a large magnetite shielding structure to minimize the background due to neutrons which scattered in the collimator walls. The final beam size of 0.5 in. was defined by a 108 in. long iron collimator which was fitted inside iron sleeves as shown in figure 2-2.

To determine the exact size, position and intensity profile of the neutron beam at the target, we employed a standard procedure which involves the use of FUJI storage-phosphor image plates. When bombarded by neutrons, these plates effectively store neutron flux information via nuclear-chemical reactions. A scan with a focused laser beam and a photo-detector can reveal the stored information. Figure 2-3 shows a sample beam profile. Our plates were scanned with a digitizer drum with a resolution of $\frac{1}{6}$ mm/pixel, which corresponded to an uncertainty in the beam position of one millimeter. See ref. [10] for more information concerning this procedure.

The pulsed nature of the incident neutron beam allows the determination of particle kinetic energies via time of flight analysis. Its pulse structure closely resembles that of the primary proton beam and consists of macro and micropulses. Figure 2-5 shows a diagram of the time structure. During the normal operation the accelerator produces 120 macropulses per second with a typical width of 625 μsec. Twenty of these macropulses are shared among other experimental areas in the lab, while the remaining 100 pulses per second are delivered to WNR. Each macropulse consists of micropulses separated by 1.8 μsec. The length of each micropulse is about 0.2 nsec. The short duration of each micropulse and the large separation time between

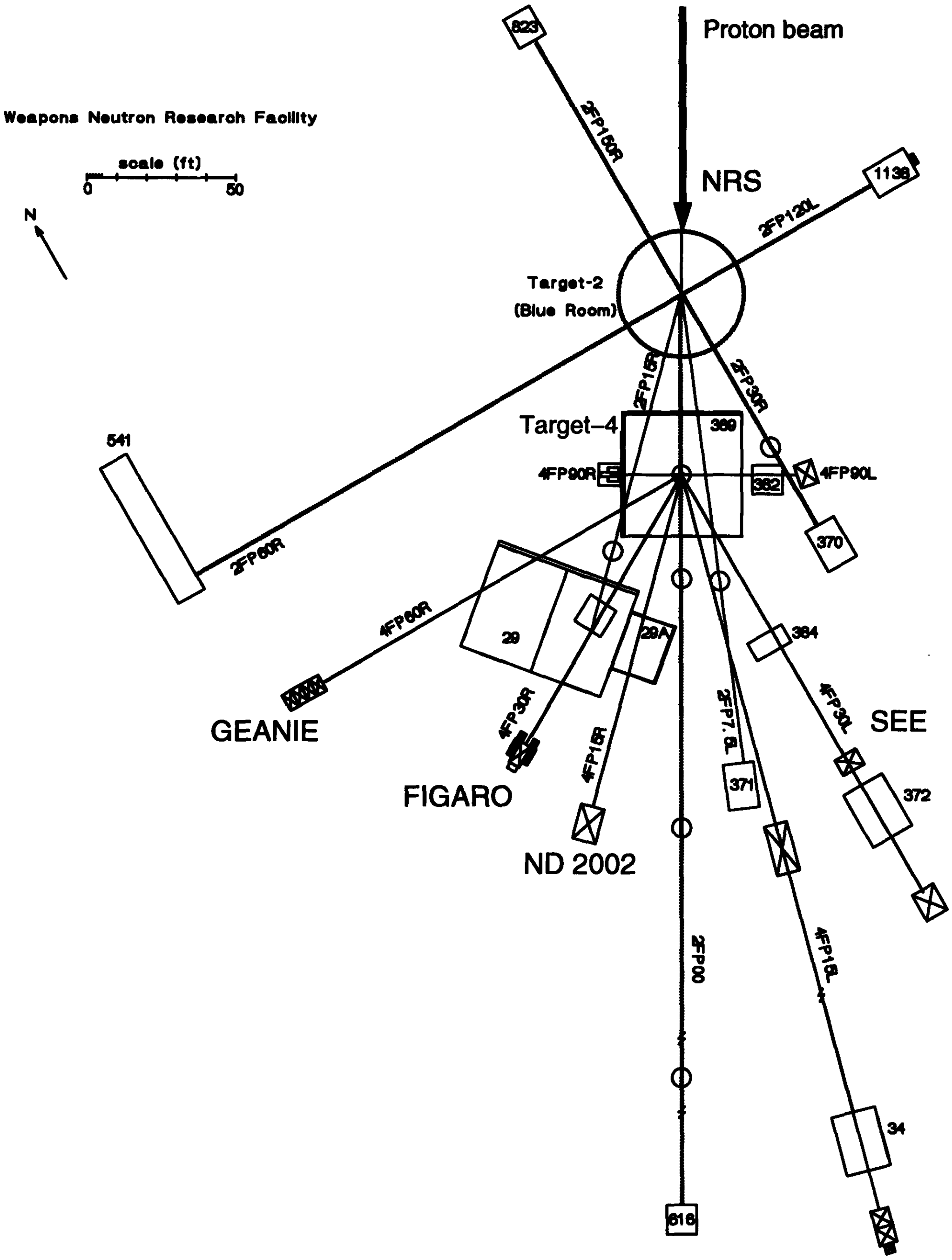

Figure 2-1: Schematic of Weapons Neutron Research facility. Present experiment occupied flight path 4FP15R, marked as "ND2002".

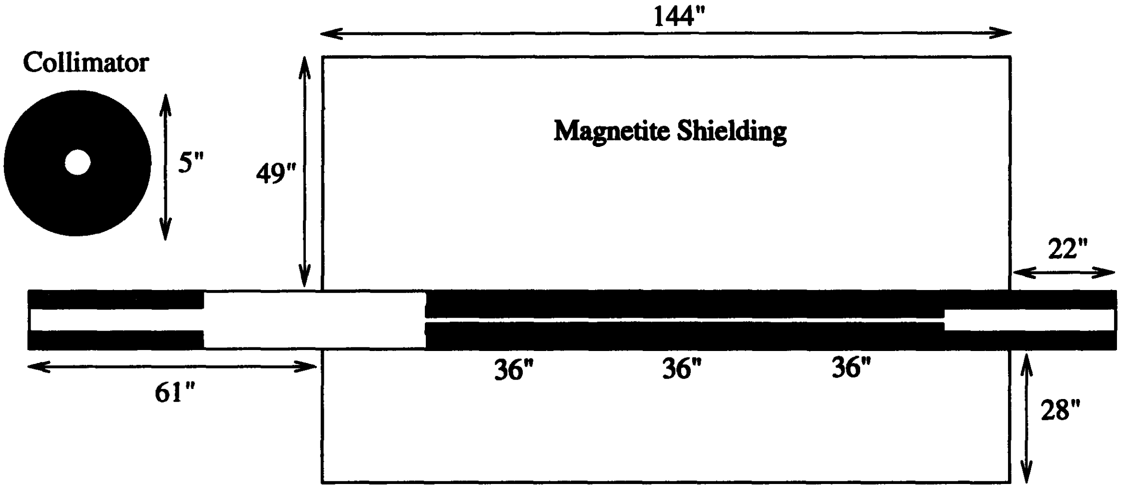

Figure 2-2: Beam collimation setup used in ND2002 experiment. Iron sleeves (blue), fitted into the beam pipe, house 18 iron rings (red) which define the beam size of 0.5″ in diameter. The magnetite shielding wall (yellow) reduces the background due to neutrons scattered in the collimator walls.

micropulses ensured that even the fastest events from one beam burst could not catch up with the slowest events of the previous burst.

2.3 Fission Chamber

The flux of incident neutrons is determined using a fission ionization detector, or *fission chamber*. The aluminum housing of the fission chamber contains eight 0.0013 cm thick stainless steel foils which provide backing to the deposits of fissionable material, such as ^{238}U, see figure 2-6. The foils are positioned 0.51 cm apart and double as electrodes. The electrical wiring diagram is depicted in figure 2-7. The fission chamber is position such that the beam passes through the backing first before striking the fissionable material deposit. The ionization induced by the charged fission products, such as alpha particles and heavy fragments, produces a pulse at the signal output. In this experiment we used the output connected to the foil containing ^{238}U. The incident neutron flux was then determined by measuring the yield of the neutron induced fission of ^{238}U.

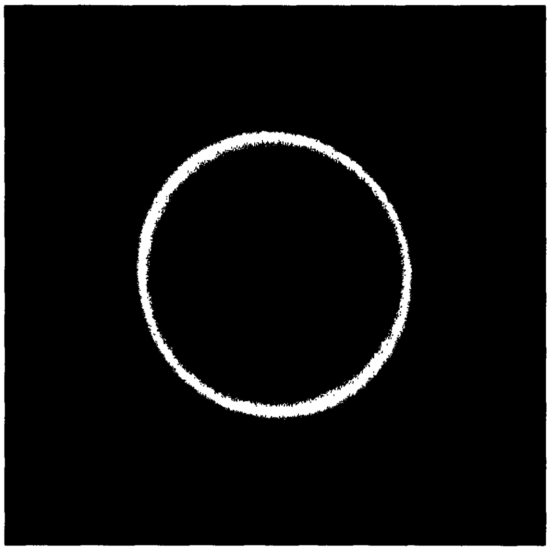

Figure 2-3: Incident beam intensity profile false color image was produced by exposing a FUJI storage-phosphor image plate in the beam. The plate was used to determine the precise position of the beam in the target region.

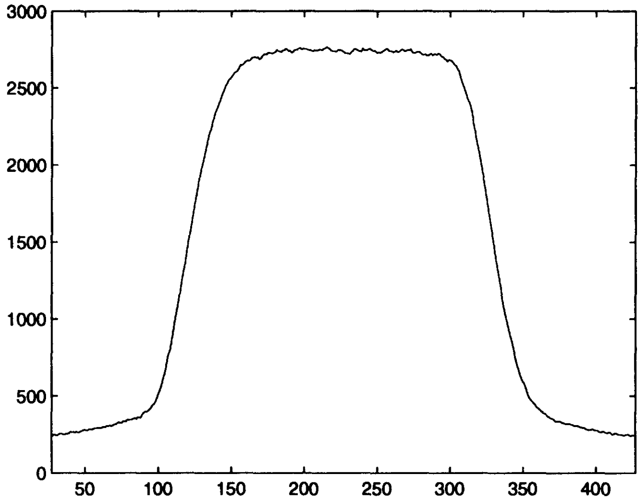

Figure 2-4: Incident beam intensity profile cross section. This section was made through the "center-of-mass" of the intensity profile.

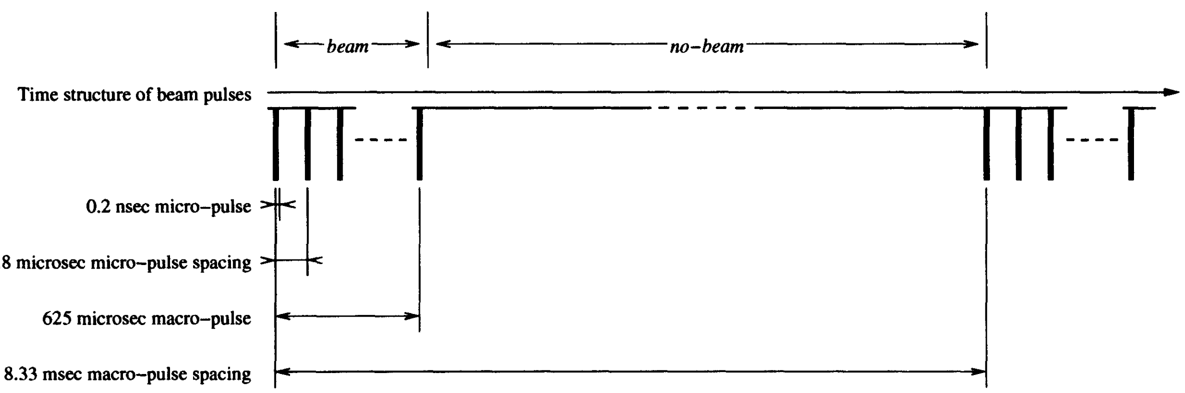

Figure 2-5: Sketch of the time structure of the pulsed proton beam. The narrow width of the micro-pulses of 0.2 nsec, and large micro-pulse spacing of 1.8 μs, allows for use of time-of-flight techniques with no danger of micropulse overlap.

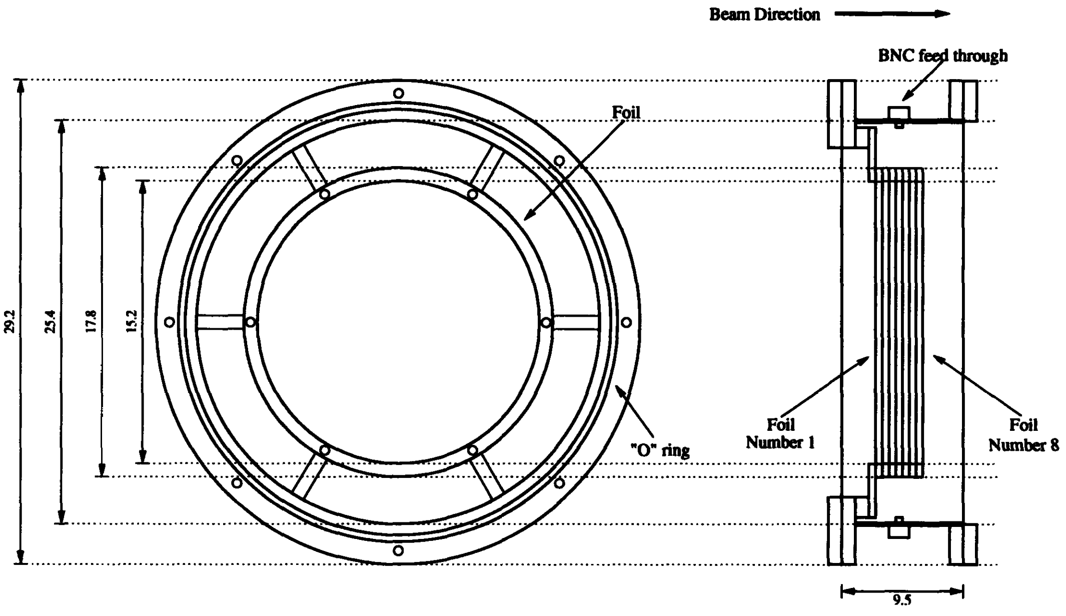

Figure 2-6: Schematic diagram of the ionization chamber (*Fission Chamber*) housing. Dimensions are in cm. See [11] for more details on fission chamber construction.

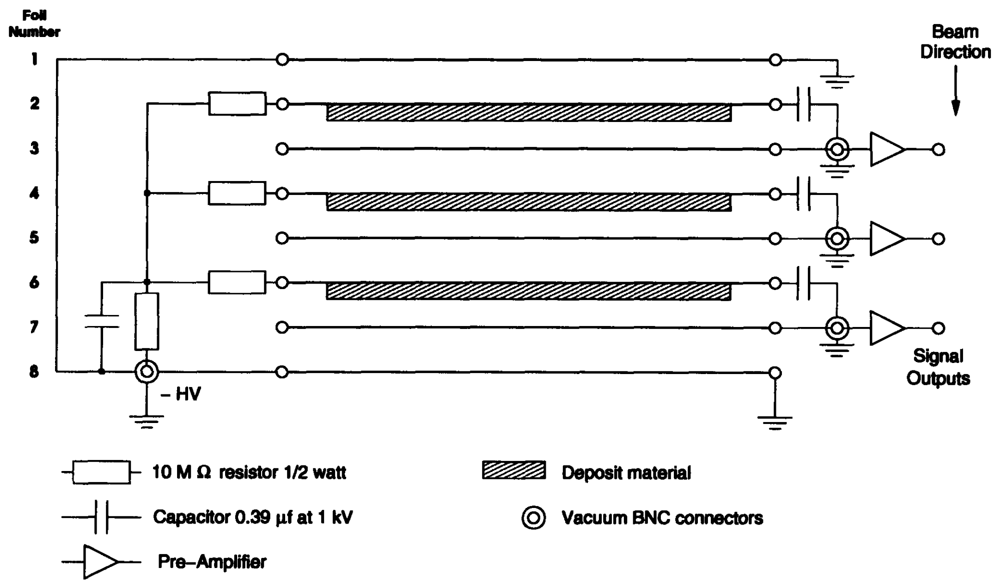

Figure 2-7: Electrical wiring diagram of the ionization chamber.See [11] for more details on fission chamber construction.

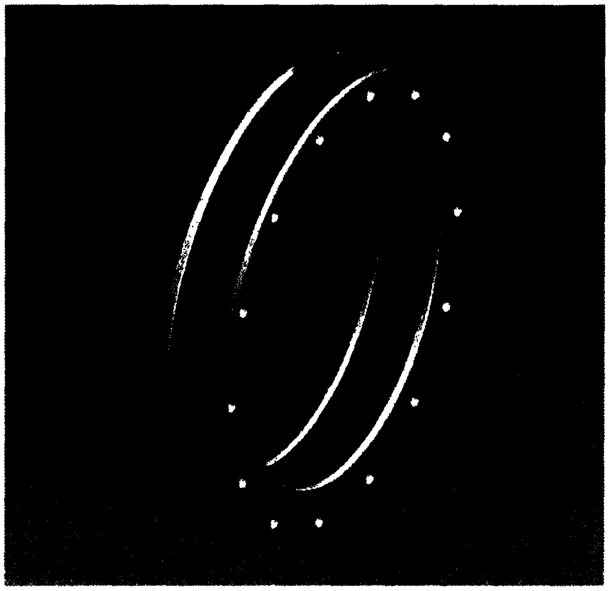

Figure 2-8: Cryogenic target flask.

2.4 Liquid Deuterium Target

A horizontal cylindrical flask, which measures 5 inches in diameter and 0.5 inches in thickness, with 2 mil mylar windows served as the liquid deuterium target. Figure 2-8 shows a computer rendering of the flask. During the experiment the target could be filled with either liquid deuterium or liquid hydrogen. Running with liquid hydrogen enabled a dedicated measurement of the elastic n–p process using essentially the same apparatus. This proved to be very valuable as it allowed us to verify the incident beam flux normalization, target thickness, and other systematic variables.

The target flask assembly was placed inside of a larger vacuum chamber to ensure adequate thermal insulation. Having a shape of a vertical cylinder with a diameter of about 32 cm, the body of the vacuum chamber was made of $\frac{3}{16}''$ stainless steel. To minimize energy loss of recoil charged particles, the chamber was equipped with a 5 mil kapton window with an opening angle of $\theta_p = 70°$ on the proton detector side and $\theta_n = 110°$ on the neutron detector side. The target flask itself was rotated about its vertical axis so that the normal to the plane of the target face was at 50° with respect to the direction of the incident neutron beam. This further reduced

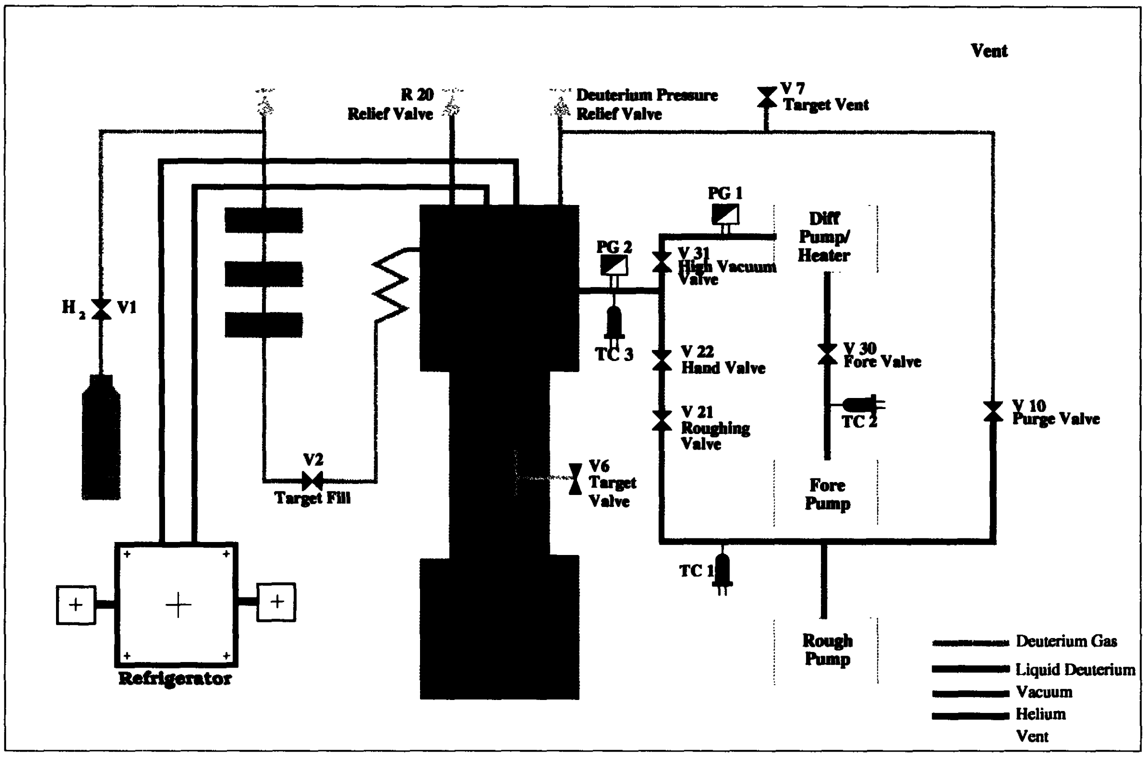

Figure 2-9: Liquid deuterium target and refrigerator system.

the average amount of energy loss for recoil deuterons. Section 5.2 offers more details on target angle optimization.

Figure 2-9 shows a schematic view of the refrigeration system used with the liquid deuterium target. The system consists of a CTI Model 1020 cooler which has a nominal cooling capacity of 10 Watts at 20 Kelvin. The liquid nitrogen trap and oxygen filter help purify the deuterium or hydrogen gas before it is liquefied in the system's condensing chamber. Purified gaseous deuterium flows through condensing fins attached to the cold head. The liquid is collected at the bottom of the system, filling the target flask. A simple resistive heater was used to control the system pressure.

2.5 Detectors

2.5.1 Proton Telescopes

Each of the six identical proton telescopes consists of the pure CsI crystal and a thin ΔE detector. The CsI calorimeter has a cross section of 9.2 cm square and measures 30 cm in length. The thin ΔE plastic scintillator has the dimensions of 2.5 mm × 9.2 cm × 9.2 cm so that it exactly covers the face of the CsI detector. Since a thin ΔE detector is better than a CsI crystal at localizing the location of the particle hit along the direction of particles velocity vector and because its output pulse is narrower than that of the CsI crystal, the ΔE detector is configured to define the timing information for any ΔE-E coincidence event. Furthermore, the ΔE-E detector combination allows for discrimination among various charged particle species.

Six telescopes, positioned such that their faces are 100 cm away from the center of the cryogenic target cell, define a horizontal scattering plane. The centers of these detectors are at 24°, 30°, 36°, 42°, 48°, and 54° with respect to the incident beam.

2.5.2 Neutron "Wall"

During the early stages of this experiment, a set of discrete neutron detectors was replaced by a continuous neutron wall, which was used in all measurements reported in this paper. This ensured that the charged particle telescopes defined the solid angle of the measured interaction, and that the neutron side did not introduce any geometrical acceptance parameters in to the cross section calculations. The neutron wall is comprised of five plastic scintillator bars, each measuring 10 cm × 10 cm × 200 cm. The bars are placed horizontally on their sides into a stack of five high, resulting in a wall of 50 cm × 200 cm. Each bar is equipped with two phototubes, one at each end. Having two phototubes per bar helps overcome the dependence of pulse height on the distance of the detected event from a phototube. Ordinarily, this effect is caused by the attenuation of the propagating light in the scintillation material. In addition, the difference of the detection times from the two phototubes can be mapped to the position of the event along the bar's length. For more information on the design and construction of the bars see [12].

The face of the neutron wall is completely shielded by four veto detectors. These are thin plastic scintillator paddles with dimensions of 25 cm × 100 cm. Their primary purpose is to

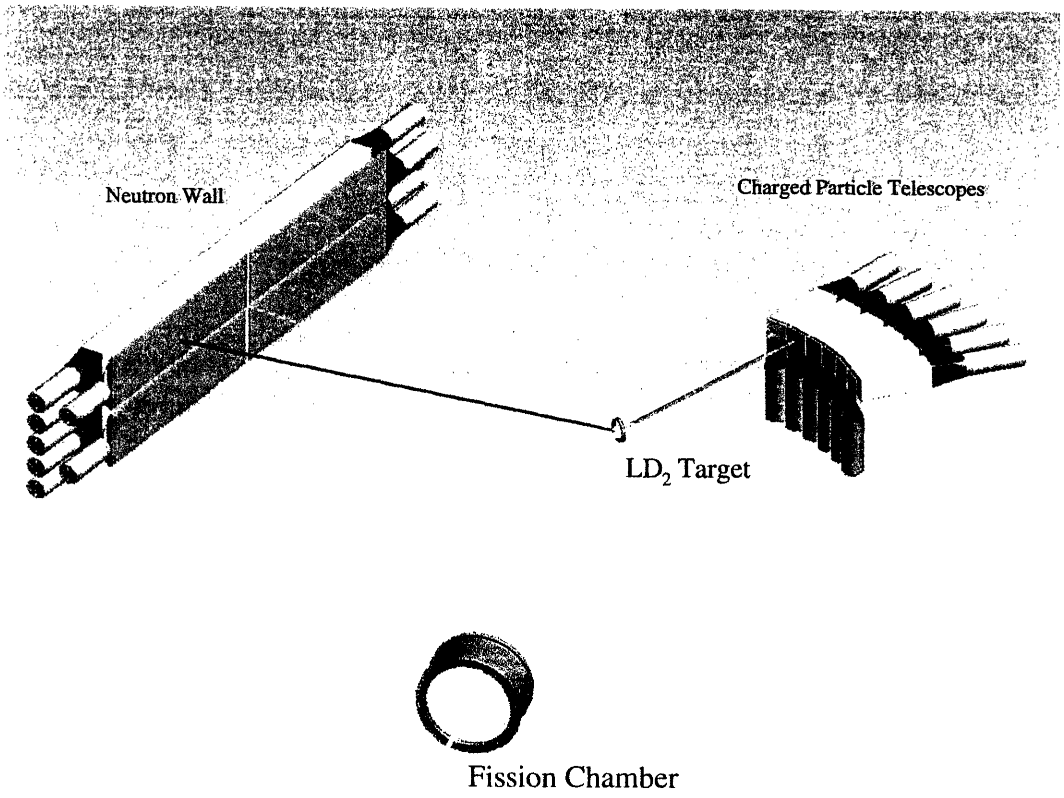

Figure 2-10: Experimental detector layout. The neutron beam (white) passes through the fission chamber and is incident on the liquid deuterium target. Recoil deuteron (red) is detected by a charged particle telescope while the scattered neutron (blue) is detected by the neutron wall.

form an anti-coincidence with the neutron bars thereby discarding any triggers due to charged particles.

The center of the neutron wall is 132 cm away from the center of the target flask, while the normal to the wall's face forms an angle of 71.0° with the direction of the incident neutron beam. The vertical alignment of the wall is such that the middle bar lies in the scattering plane, defined by the beam, the target and the charged particle telescopes. In this configuration the neutron wall subtends a range of scattered neutron angles from 33.9° to 108.1°. This angular range accommodates conjugate neutrons for all six coincidence *n–d* pairs and for four most forward coincidence *n–p* pairs.

2.6 Data Acquisition System and Electronics

The remainder of this chapter addresses the issue of the signal processing electronics for various detectors employed in the experiment. In the instances where multiple detectors of the same type were implemented, e.g. six identical proton telescopes, five identical neutron bars, etc., a schematic diagram for one such detector will be given. The electronic setups for the remaining detectors in each type are identical to the one presented here.

2.6.1 Charged Particle Telescope Electronics

Figure 2-11 shows a block diagram of the signal processing electronics for a charged particle telescope. The telescope consists of a thin plastic scintillator, dE, and a CsI calorimeter crystal.

The analog signal from the CsI detector is split in two. One copy serves as an input to a Constant Fraction Discriminator (CFD) which derives the timing information for the event, while the other is sent via a linear gate to a charge-integrating Analog-to-Digital Converter (ADC) for pulse height analysis . As the integrating gate of the ADC is set to be rather wide, the linear gate helps define the limits of integration for each pulse. The gate input of the linear gate is controlled by one of the outputs of the CFD. An additional discriminator facilitates fine-tuning of the width of the gate. The second output of the CFC starts a Time to Digital Converter (TDC), which is subsequently stopped by a delayed copy of the t_0 pulse. Finally, the third output of the CFD is routed to a coincidence unit to form coincidences with the associated ΔE detector.

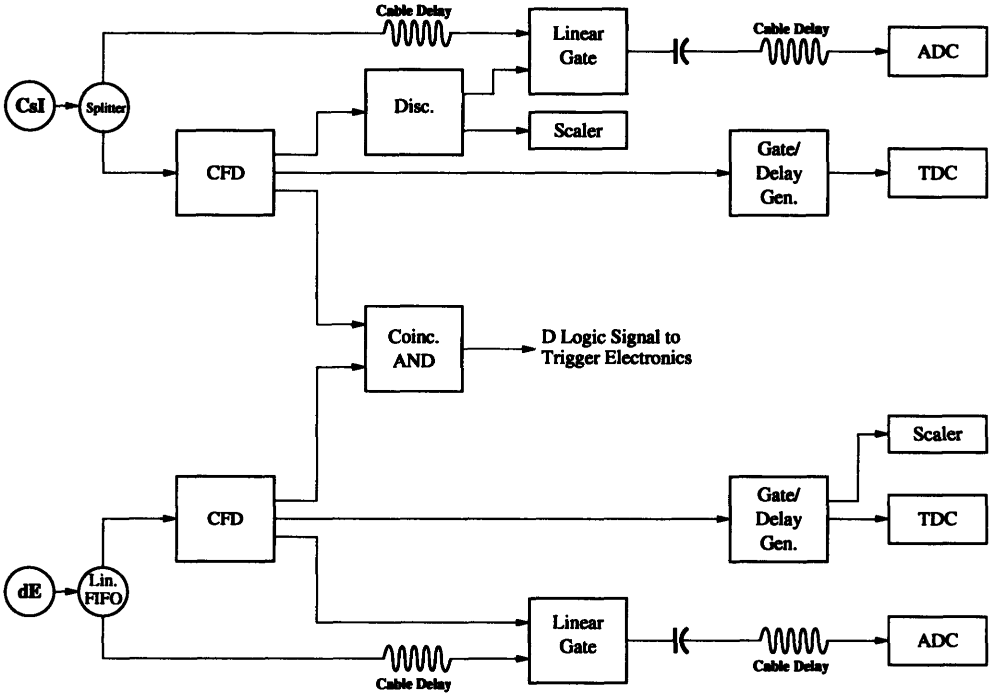

Figure 2-11: Block diagram of the signal processing electronics for a charged particle telescope.

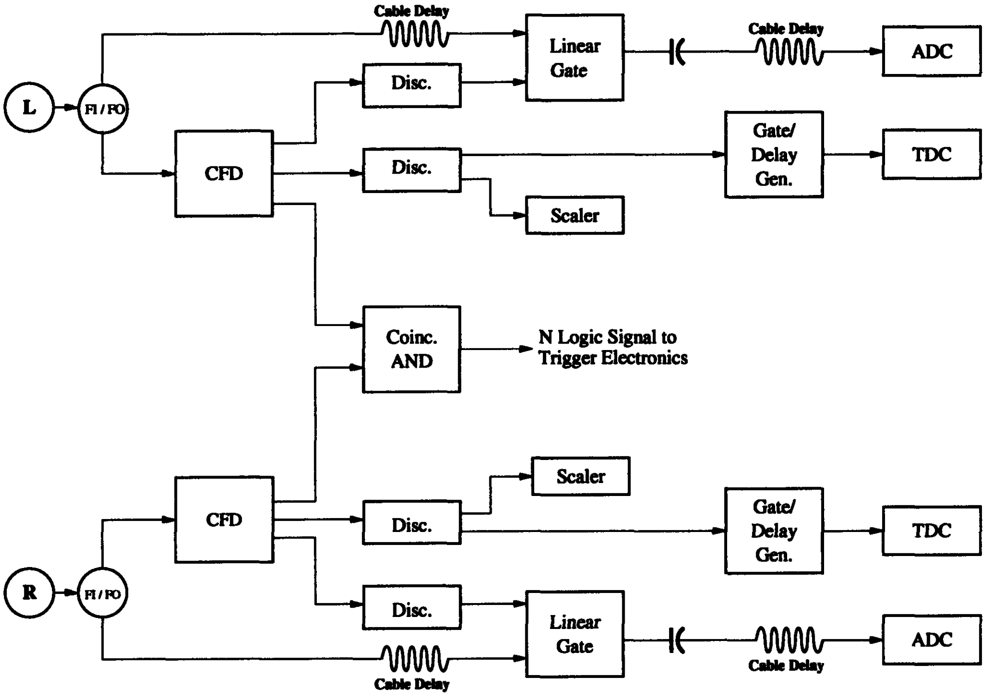

Figure 2-12: Block diagram of the signal processing electronics for a neutron bar.

The ΔE electronics is identical to the CsI electronics in principle, with a few minor variations. For instance, a Linear Fan-in/Fan-out module used to split the original analog signal replaces the Splitter used in the CsI electronics.

The output of the ΔE-E coincidence unit is sent to the trigger logic. This arrangement guarantees that the telescope will respond only to charged particles entering the CsI through the front face, since only the events in which both ΔE and E detectors fired in coincidence can generate a trigger.

2.6.2 Neutron Wall Electronics

Each of the five neutron bars which make up the neutron wall requires a set of two identical electronic channels, one for each phototube. They are labeled as “L” for left and “R” for right in figure 2-12.

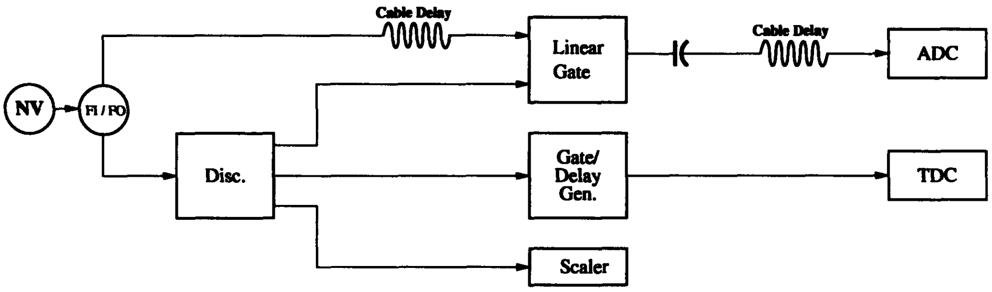

Figure 2-13: Block diagram of the signal processing electronics for a neutron veto.

A Linear Fan-in/Fan-out module generates two identical copies of the original analog signal from each phototube. One copy, trimmed by a linear gate, is sent to the ADC for pulse height determination while the other is fed into a CFD for time analysis. The CFD generates a digital pulse whose time characteristics are independent of signals pulse height. The three copies of the CFD output are distributed in a familiar fashion: the first controls the gate input of the linear gate, the second starts the TDC, while the third is fed into a coincidence unit to form coincidences between L and R phototubes.

Since the two phototubes are separated by 200 (cm), the coincidence window for L-R coincidences must be set wide enough to allow for light propagation delays inside the BC408 plastic scintillator. Furthermore, the thresholds of the two CFDs must be low enough to accommodate uneven light attenuation inside the scintillator material for events far from the middle of the bar. The output of the L-R coincidence is sent to the trigger logic.

In addition to the five neutron bars, the neutron wall contains four thin plastic scintillators, often referred to as Neutron Vetos. Their job is to reject events in the neutron wall caused by charged particles. Unlike the ΔE-E coincidence, the Veto-Bar anti-coincidence is applied in software during the offline analysis, rather then being implemented in hardware. Figure 2-13 shows the block diagram for the signal processing electronics for a neutron veto. We are not concerned so much with the accuracy of the TDC information from the neutron vetos since both the ADC and TDC values are used only to validate, or more appropriately, to invalidate an event. This simplifies the schematic, while the overall logic remains identical to that used for other detectors. Note that no trigger information is derived from the neutron veto signals.

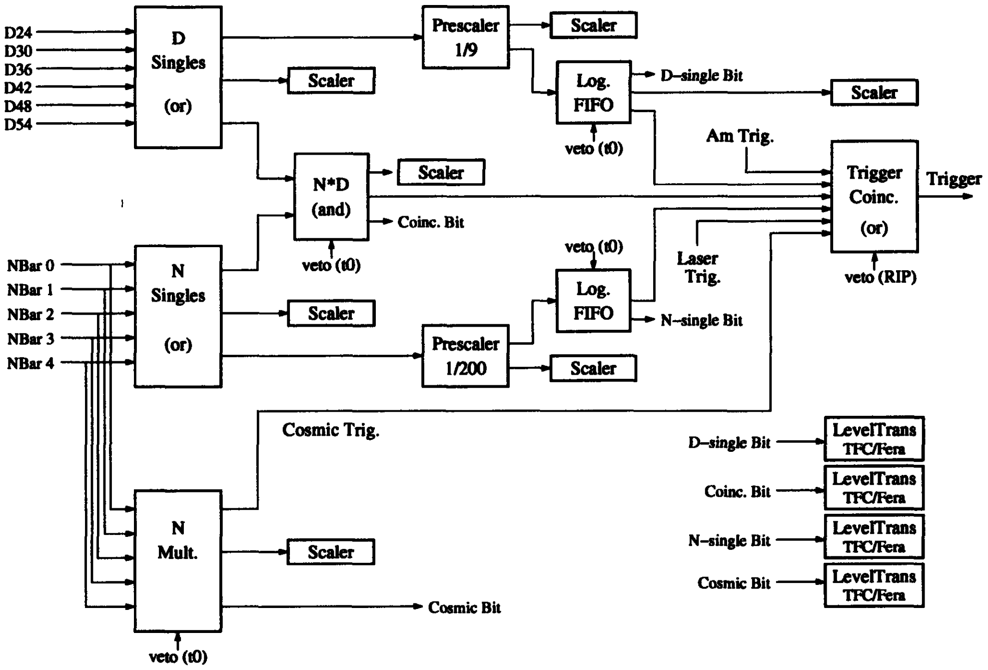

Figure 2-14: Block diagram of the electronics for trigger generation.

2.6.3 Trigger Electronics

Our electronic setup supports six dedicated trigger types: charged particle single, neutron single, *n–d* coincidence, cosmic, laser, fission, and americium. Figure 2-14 shows the way in which signals for each trigger type are generated.

The logic trigger signals from the individual charged particle telescopes, labeled in the figure as D24 ... D54, are OR*ed* together in a logic unit. The logic trigger signals from all neutron bars (L-R coincidences), labeled as NBar0 ... NBar5, are OR*ed* together in another logic unit. The outputs of the "D Singles OR" and "N Singles OR" gates are combined in a coincidence unit, which tags all events in which a signal from any charged particle telescope appeared during the same coincidence window with a signal from any neutron bar. We refer to these events as the "N*D" events. They are, of course, the coincidence events of primary interest during the elastic *n–d* or *n–p* measurements. To designate such an event as a coincidence event the output of the "N*D" AND-gate sets a *coinc* bit. The bit is nothing more than a separate TDC channel. It is set if its value is somewhere between 50 and 2000, and cleared otherwise. Another output of the "N*D" coincidence unit is fed into the master trigger OR-gate, in which all trigger types are combined to generate the master trigger.

In addition to coincidence events, we wish to trigger the data acquisition every time there is a "D Single" or an "N Single" event. To accomplish this, copies of the signals from the "D Single" and "N Single" OR-gates are routed to the master trigger OR-gate via corresponding pre-scaler units. The 1/N pre-scalers help even out the proportion of singles events, which greatly outnumber coincidence events, by accepting only every N^{th} one. The typical value of N for the "D Singles" was 9, while it was 200 for "N Singles".

To minimize the number of uncorrelated coincidences and background singles events written to the disk, we wish to restrict the generation of the *coinc*, *Dsingle*, and *Nsingle* triggers to a specified time interval immediately following each beam burst. This is done using a t_0 veto which voids the inputs to the "D Singles" and "N Singles" OR-gates, as well as to the "N*D" coincidence unit.

The naturally occurring cosmic rays proved to be indispensable during neutron bar calibration, as described in Chapter 3. These are high energy minimum-ionizing events which trigger several neutron bars simultaneously and, therefore, are easily identifiable. Their identification is further simplified by a dedicated trigger type. The *cosmic* trigger is formed by a multiplicity unit. It accepts the copies of individual trigger outputs from the five neutron bars and fires only if the number of individual bar triggers is greater than N. For our purposes N was set to 3. To minimize the probability of uncorrelated coincidences of several neutron bars due to high count rates when beam is on, a modified t_0 veto ensures that the cosmic trigger is generated only between the beam bursts.

2.6.4 t_0 Electronics

The single most important signal in our data acquisition system is a pulse derived from a proton beam inductive peak off near the spallation target. This signal, which is often referred to as "t_0", marks the time of the neutron beam production. It serves three main purposes in our setup. First, its delayed copy stops the TDCs for all detector channels. As you may recall, the TDC for a particular detector is started by the trigger pulse generated by that detector. Such "common stop" arrangement ensures that there are more TDC stops than starts. Second, the t_0 signal provides a way of limiting the trigger generation to a time interval immediately after each beam burst, effectively rejecting all triggers in the absence of the beam. Finally, the t_0

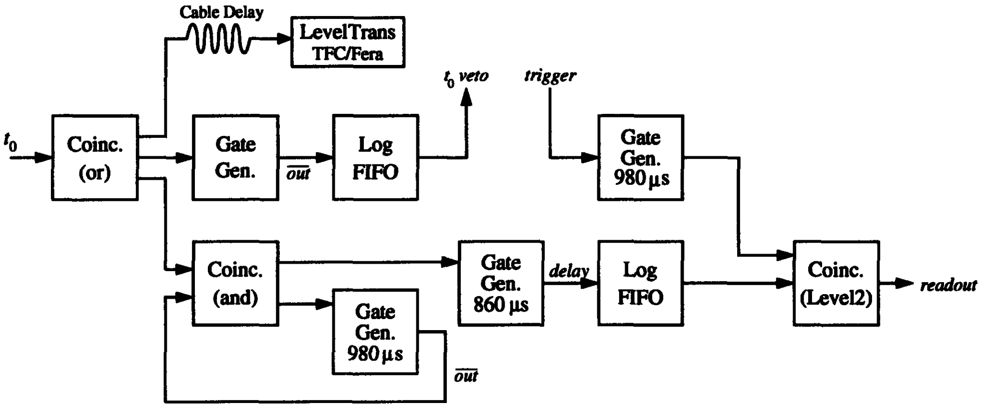

Figure 2-15: Block diagram of the t_0 electronics.

signal helps to ensure that the read out of the FERA memory buffers, which is a slow process requiring 2-3 msec, happens during the interval between beam macropulses. In this way the electronic life time of the system is maximized.

Figure 2-15 shows how these goals are achieved in practice. The logic t_0 signal is split three ways using an OR-gate with multiple outputs. The heavily delayed copy of the signal is fed into the TDC stop. Another copy sets the data acquisition window via a gate generator, whose inverted output allows trigger generation only during the first 1.8 μsec after each beam burst. The readout logic uses the third copy of the t_o signal. The goal here is to ensure that the readout signal is generated only between beam macropulses and only if one or more triggers were generated during the previous macropulse. The feedback loop takes care of the first task. A coincidence unit coupled with a gate generator which produces an inverted 980 μsec-long gate effectively single out the first t_0 signal of each macropulse, blocking all others. A delay of 860 μsec measured from the first t_0 puts us just passed the end of the macropulse. This would be a good time to read out the FERA buffers if one or more triggers happened anytime during the preceding macropulse. This condition is implemented using an AND-gate where the signal from the delayed $first$ t_0 is combined with the master trigger. The master trigger generates a 980 μsec-wide gate to ensure that the triggers produced early in the macropulse will still be on-time to form a readout signal.

2.6.5 Fission Chamber Electronics

The signal processing electronics for the fission chamber were set up as per the instructions of figure 3 in [11]. The diagram is reproduced in figure 2-16 for completeness. A fast pre-amplifier amplified each signal from the ^{238}U sensing foil before passing it to a fan-out unit, where three identical copies of the signal were made. Two of the copies were sent to discriminator circuits in charge of the trigger and timing generation. The use of a constant fraction timing discriminators (CFTD) guaranteed that the timing was independent of the pulse height. Furthermore, having two dedicated circuits for timing and trigger generation enabled the adjustment of lower level cutoff without affecting its timing characteristics. For this to work, the threshold on the timing discriminator was set lower than that on the discriminator used to define the lower level cutoff. Signals from both discriminator circuits were combined with a beam gate in a three-input logic "AND" gate. As is clear from the diagram of proton beam time structure (figure 2-5), the duty cycle of the accelerator is rather small. The primary purpose of the beam gate, therefore, was to restrict data acquisition to times when beam neutrons were incident on the fission chamber. This helped to cut down on the number of acquired time-random alpha decays. Since the number of the incident neutrons is much larger than the number of neutron induced fission events, the TDC was started by the trigger and stopped by a delayed copy of the t_0 pulse.

The third copy of the original amplified signal passed through a linear gate and was recorded by FERA ADC.

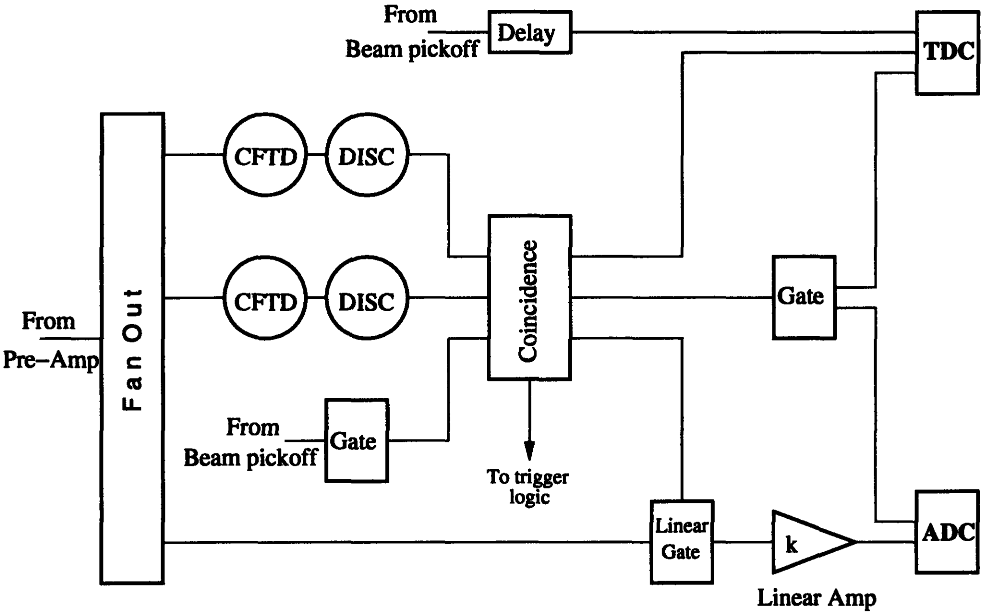

Figure 2-16: Block diagram of the signal processing electronics for the fission chamber from [11].

Chapter 3

Calibration

3.1 Charged Particle Telescopes

The calibration procedure for the six charged particle telescopes can be divided into two parts: time calibration and energy calibration. Accurate time calibration is essential for the success of the measurement of elastic processes since the timing information alone defines all kinematic variables of the interaction. The pulse height data provide valuable supplemental information for particle identification and other tasks. It is also necessary to completely define an inelastic process, such as the n–p quasielastic scattering. Since the approach used to establish the conversion between the CsI pulse height and the kinetic energy of the recoil particle at interaction vertex relies heavily on the results of a Monte Carlo calculation, including the energy loss correction, we defer its discussion until chapter 5. In this section we shall focus on the technique used to perform time calibration of the charged particle telescopes.

3.1.1 Time of Flight

Figure 3-1 defines all observables which are measured directly in the experiment. They are the total times of flight for scattered and recoil particles, TOF_n (one from each phototube) and TOF_p, charged particle telescope pulse heights, $\mathrm{PH}_{\mathrm{CsI}}$ and $\mathrm{PH}_{\Delta\mathrm{E}}$, and the neutron wall pulse heights, PH_{veto} and PH_{bar} (one from each phototube).

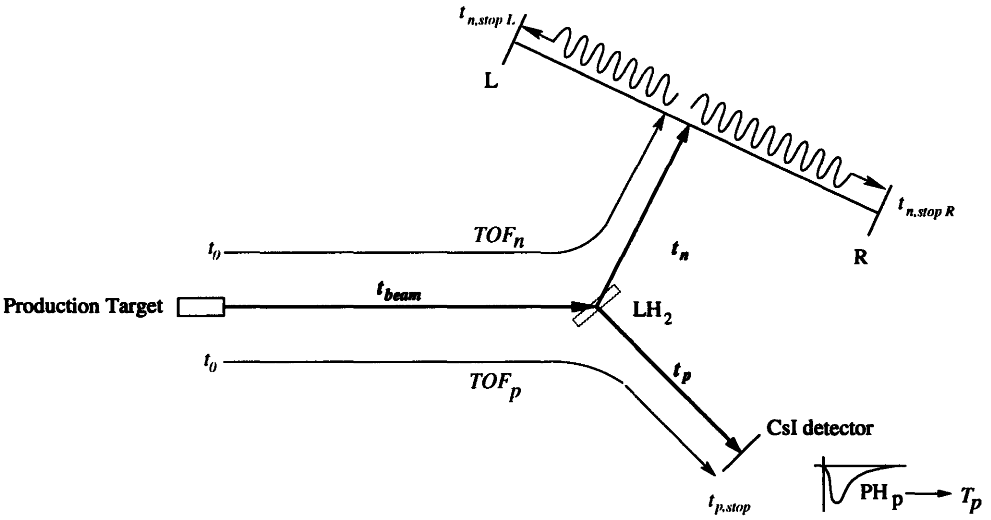

Figure 3-1: Schematic view of measured experimental observables. Quantities t_0, $t_{n,stopL}$, $t_{n,stopR}$, $t_{p,stop}$ and PH_p are measured directly.

As we have already noted in chapter 2, all timing information is collected using a *common stop* scheme. A TDC is started by a particle hit and is stooped by a delayed copy of the "t_0" signal. To find the total time of flight TOF_p it is necessary to find the difference between the detector's TDC readout and the "t_0". A linear relation transforms this difference from TDC channels to the time interval in nanoseconds. This process requires two parameters.

The first one describes the width of each TDC bin in nanoseconds. It is found by connecting each TDC to a pulse calibrator module which generates periodic pulses with a preset period. Dividing the period by the measured TDC value in channels yields the width of each TDC channel. For our setup a typical value of the width was about 1.3 nanoseconds per channel.

The second parameter is a linear offset. It reflects the fact that each detector's signal must traverse a unique length of cable and is subject to a unique amount of delay. To determine this offset we plotted the number of events as a function of the TDC – "t_0" difference for each detector; figure 3-2 shows a typical spectrum. Notice the sharp, well separated peak. It is produced by the large number of photons which are created at the spallation target and travel down the beam pipe just ahead of each neutron burst. Knowing the exact length of the neutron beam path (L_0) and the distances between our cryogenic target and the detectors enables us to find the exact time of arrival for the γ-flash by dividing the total path by the speed of light.

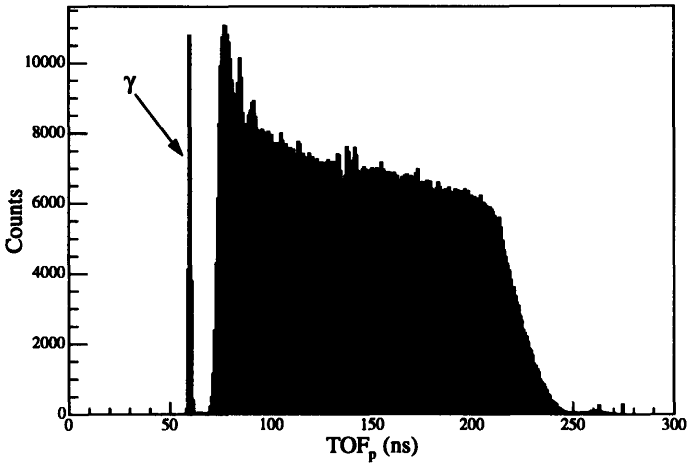

Figure 3-2: Proton time of flight (CsI at 24°).

This, in turn, fixes the linear time offset unambiguously. The difference between the expected and actual time of arrival for γ- flash events appears in figure 3-3 for verification.

3.2 Neutron "Wall"

While the time calibration of CsI detectors proved to be fairly straightforward, additional care had to be taken when applying the γ-flash technique to neutron scintillator bars, as seen in the following illustration. [1]

Since the γ-rays produced at the spallation target are forward peaked, they do not uniformly illuminate the neutron wall. The flux of γ-rays is largest near the right phototube and degrades rapidly as one moves leftward along the wall. As a result, one should expect an uneven γ-ray distribution in the TOF histograms for left and right phototubes. In fact, while the γ-flash peaks appear clearly in the right-hand phototubes of neutron bars the left phototubes do not exhibit easily identifiable γ-flash peaks. Figure 3-4 illustrates this phenomenon. Upon closer examination of the left spectrum one discovers a remnant of the γ-ray peak merged with other,

---

[1] We use the Neutron Bar 2 (middle bar) to demonstrate the steps of the analysis as this bar lies in the plane of the incident neutron beam and proton telescopes; the rest of the bars were observed to exhibit similar behavior.

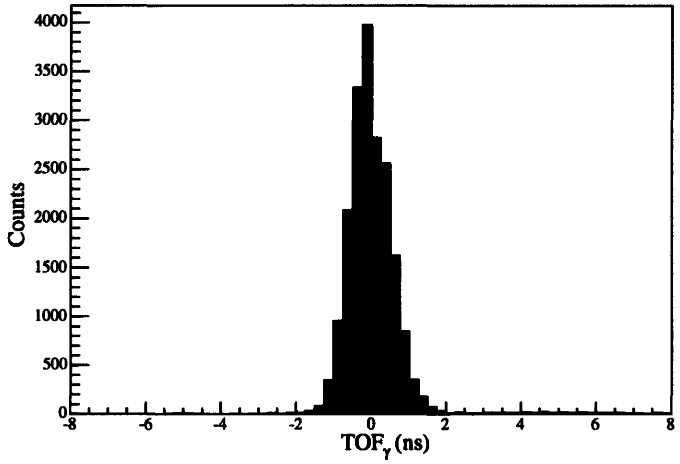

Figure 3-3: Photon time of flight validation. This plot shows the difference between expected and actual times of flight for the γ-flash events in CsI at 24°.

seemingly super-luminal, events. The reason for these events is simple. Since most of the gamma rays strike each bar near its right phototube their time of flight as measured by the left phototube includes a sizable contribution due to the light propagation delays inside each plastic bar. Therefore a fast neutron which strikes a bar near the left phototube may arrive with a shorter time of flight than the majority of photons. This also explains why the issue does not exist for the right phototube.

To accent the γ-flash peaks in the TOF spectra of left phototubes we must better localize all events plotted in the histograms. One way of doing just this is to plot the times of arrival for events detected in a small middle region of the bar. In practice we admit only those events with a difference between times of flight for the left and right phototubes of about 10 TDC channels. This effectively selects the middle region of each bar. The selected regions are roughly 3 cm in length. Figure 3-5 demonstrates that while the γ-flash peak is still clearly visible in the right spectrum, it is now also well defined in the left spectrum.

There are two ways to combine time information from left and right phototubes to arrive at meaningful physical quantities which characterize scattered neutrons. The following two sections examine each of these in turn.

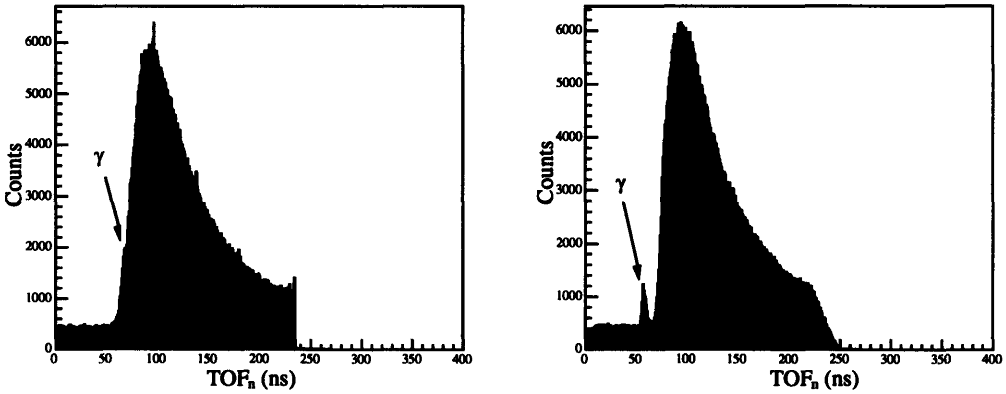

Figure 3-4: These spectra represent events collected along the entire length of Bar 2. The γ-flash peak is hard to identify in the left phototube TOF spectrum (left). The problem does not exist for the right phototube (right).

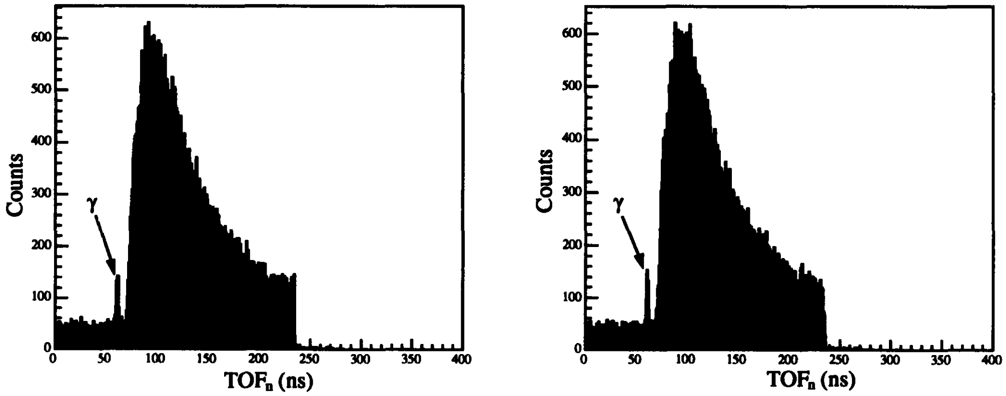

Figure 3-5: These spectra represent events collected from a small region near the middle of Bar 2. The γ-flash peaks are clearly visible in both left and right spectra.

3.2.1 Mean Time of Flight

One of the most desirable observables pertaining to the scattered neutrons is their time of flight. Neutron time of flight maps directly into neutron kinetic energy which helps define the scattering kinematics. Ordinarily, for well localized particle detectors equipped with a single phototube time of flight information is derived from the timing of the signal received from this phototube. It is easy to see that having a large detector with a significant amount of light propagation delay renders time information of any single phototube dependent on the position of a particle hit. This is clearly the case for our neutron bar detectors as has been demonstrated in figure 3-4.

Remarkably, one combination of timing information from left and right phototubes is completely independent of the position of a particle hit. Namely, the sum of the left and right times is proportional to the neutron time of flight. [2]

$$\overline{\mathrm{TOF}}_n = \frac{1}{2}\left[\mathrm{TOF}_{left} + \mathrm{TOF}_{right}\right]. \tag{3.1}$$

The neutron time of flight defined in this way includes the delay associated with light propagation inside the neutron scintillation bars. The amount of delay is exactly equal to the time required for light to propagate through the entire length of the bar. Therefore, this offset is constant for each neutron event independent of position along the bar. It is a simple matter to correct for the delay by adjusting the additive constant during the linear mapping of neutron TDC channel to nsec.

3.2.2 Neutron Angle

Another useful combination of TOF_{left} and TOF_{right}, their difference, defines the neutron scattering angle via simple trigonometric relations. To minimize any systematic errors associated with the uncertainty in geometrical quantities, e.g. detector positions, sizes, etc., we chose to map the time difference directly into neutron angle using the coincidence n–p elastic events and supplementary position detectors.

---

[2] The assumption here is that the variation in neutron path length due to the planar geometry of the neutron wall amounts to insignificant variation in total time of flight for neutrons striking the middle and an end of a bar. That is, the time variation is smaller than the timing resolution of the apparatus. Clearly, this assumption improves with increase in neutron kinetic energy.

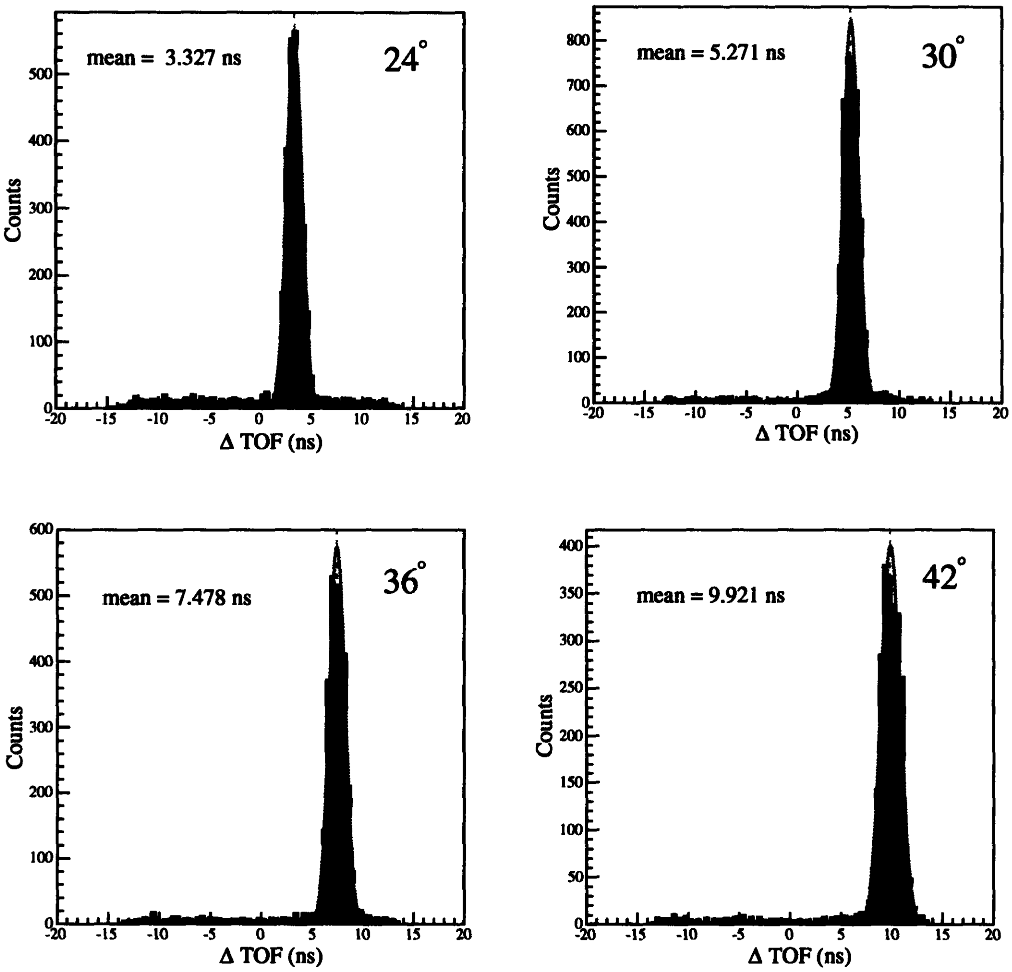

Figure 3-6: *n–p* elastic coincidence events for 200 MeV. The peaks in these spectra are formed by neutrons conjugate to 24°, 30°, 36° and 42° charge particle telescopes. Knowledge of the exact *n–p* kinematics yields a map of ΔTOF to neutron scattering angle.

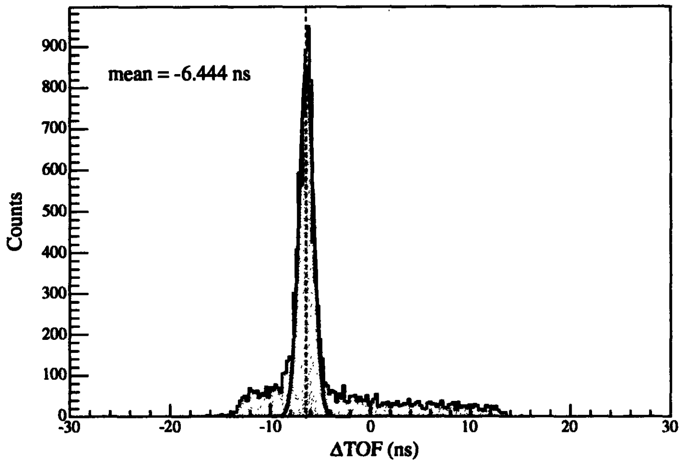

Figure 3-7: Coincidence spectrum of the neutron wall and the left position bar. Contributions of all five neutron bars were added to form this plot.

Figure 3-6 shows spectra of conjugate neutrons in coincidence with four charged particle telescopes as a function of the difference of neutron time of flight for left and right phototubes, $\Delta\mathrm{TOF}_n$. Knowing the exact elastic kinematics for the events in the coincidence peaks, in this case the n–p elastic events at 200 MeV, it is a simple matter to correlate $\Delta\mathrm{TOF}_n$ and the neutron scattering angle. These data are represented by the red circles on figure 3-8. Unfortunately, the n–p elastic coincidence events span only the right half of the neutron wall. To obtain a more accurate transformation, it is advisable to have at least one measurement in the left half of the neutron wall. The left position bar allows us to do just that.

The position detectors are two thin vertical strips of plastic scintillator material each coupled to a phototube and placed across the back face of the neutron wall at 49.5 cm and 149.5 cm from the right so as to overlap with all five neutron bars. The coincidence of a position detector with a neutron bar helps identify a known position along the bar in the $\Delta\mathrm{TOF}_n$ histogram. Figure 3-7 shows a plot of the coincidence of the left position bar with the neutron wall. Contributions of all five neutron bars were added to produce this plot. The coincidence peak yields the desirable position measurement for the left half of the neutron wall. The corresponding data point appears in green in figure 3-8.

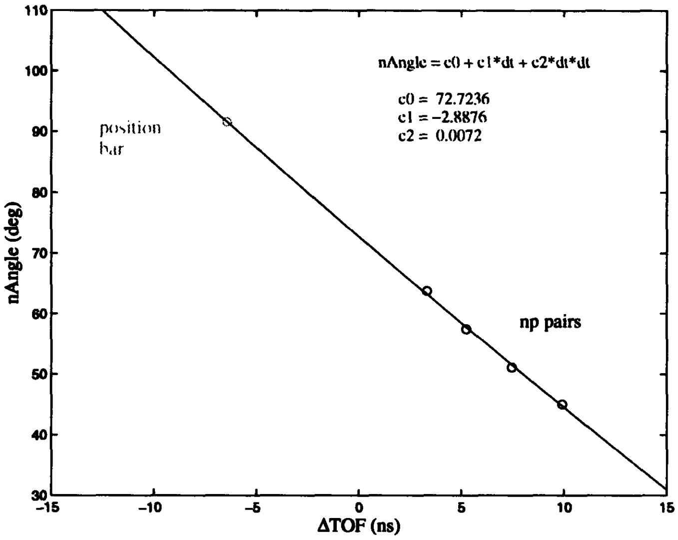

Figure 3-8: Neutron scattering angle as a function of $\Delta\mathrm{TOF}_n$. Measurements of the positions of conjugate neutrons for 200 MeV n–p elastic scattering (red) are combined with the measurement using a supplemental position detector (green) to define a second order polynomial transformation.

3.2.3 Cosmic Ray Time Spectra

In order to verify that the left and right timing information is valid we plotted the difference of TOF_{left} and TOF_{right} for cosmic ray events. These are events in the neutron bars due to spatially-uniform minimum-ionizing cosmic rays. To isolate cosmic ray events from others we limited the time interval during which the electronics could accept such events to the beam-off periods between beam bursts. In addition, a hardware multiplicity module tagged an event as cosmic only if three or more neutron bars fired within a tight time window. The time difference spectra for cosmic ray events appear in figures 3-9 and 3-10.

To our surprise both the calibrated and the raw time difference spectra were not smooth but possessed a periodic structure. Although the bumps in the time difference spectra would ordinarily signal an uneven spatial distribution of events in the detectors, the unlikely hypothesis that the peaks reflected real spatial non-uniformities in cosmic ray distributions was quickly dismissed by looking at the time sum spectra. Raw time sum spectra appear in figure 3-11. As we mentioned previously, the sum signal carries information about the time with respect to t_0 and is independent of position along the bar. The fact that these spectra exhibit similar bumpiness suggests that the cause of the bumps is most likely due to the electronics, e.g. reflections or cross-talk in the cables or NIM modules. It is interesting to note that the overall structure of the time difference and time sum spectra proved to be quite time-independent. Figures 3-12 and 3-13 compare cosmic ray data for three run periods separated by days. All three data sets look amazingly alike.

To gain further insight into this phenomenon we performed the following test. First, all cosmic events were singled out using the cosmic event trigger described above. Among these events we selected only those in which all five neutron bars fired. The TOF_{left} - TOF_{right} information helped determine the position of the hit along each bar. Next, we recreated each cosmic ray track by fitting a first degree polynomial to the hit positions for bars 0, 2, and 4. Finally, we estimated the locations of the cosmic ray interaction in the remaining bars 1 and 3 and compared the estimates with the actual measured positions for these bars. Figure 3-14 offers a schematic view of this process. The results of this test appear in figures 3-15 and 3-16. Both figures display the same information with the single distinction that the hit's position in the second figure has been expressed using the neutron scattering angle scale. While these figures clearly show a correlated deviation of measured position as a function of position along each bar, the magnitude of such deviation appears to be within ±5 centimeters (±2 degrees lab).

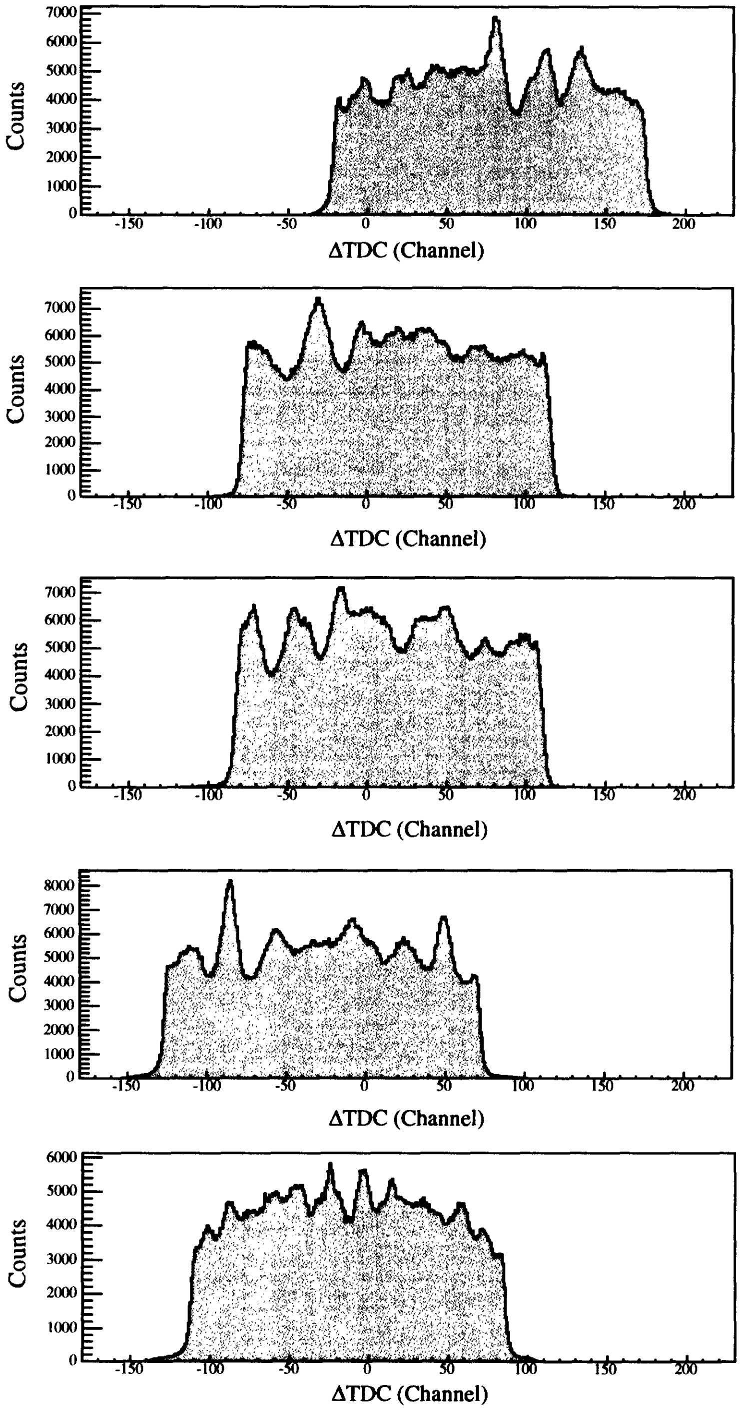

Figure 3-9: Raw time-difference spectra (TDC_{left} - TDC_{right}) for cosmic ray events. Time scale is in TDC channels.

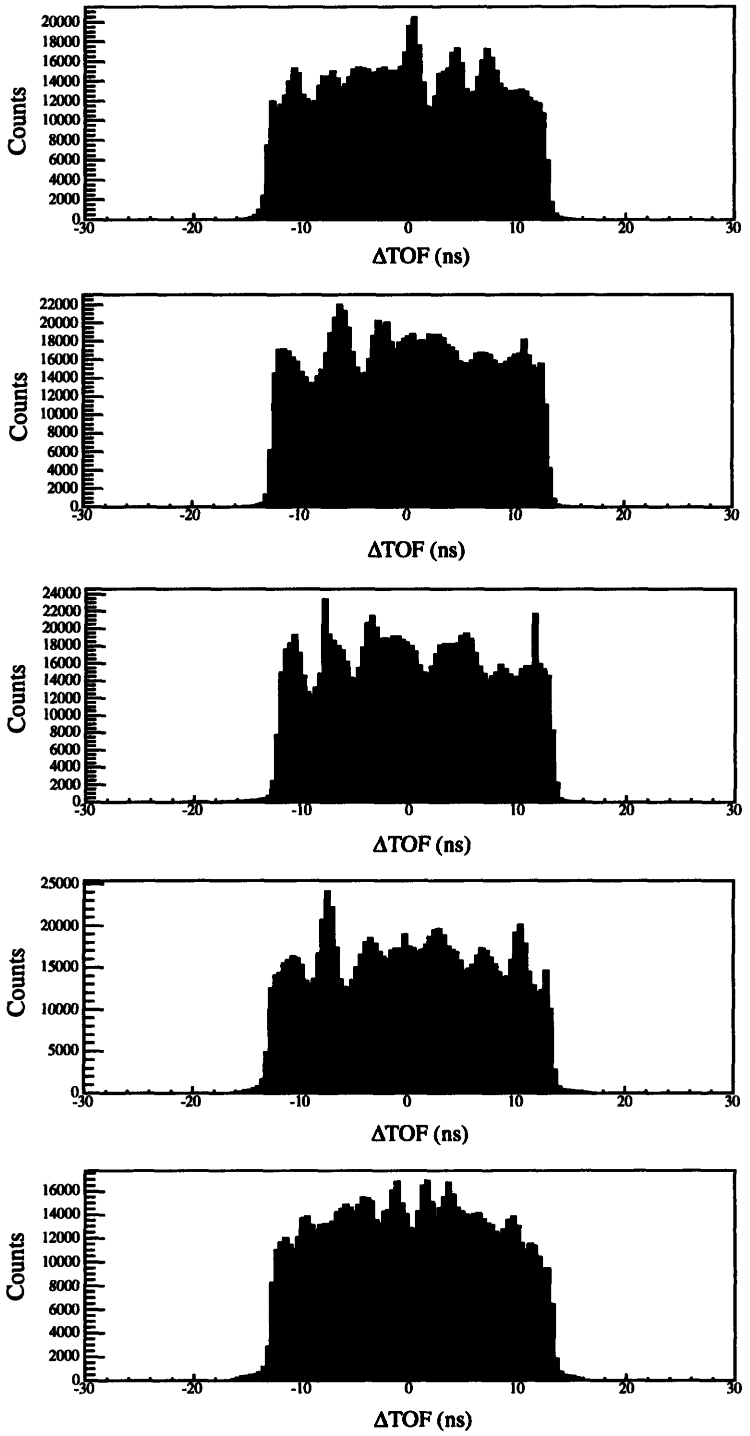

Figure 3-10: Calibrated time-difference spectra (TOF_{left} - TOF_{right}) for cosmic ray events. Time scale is in nanoseconds.

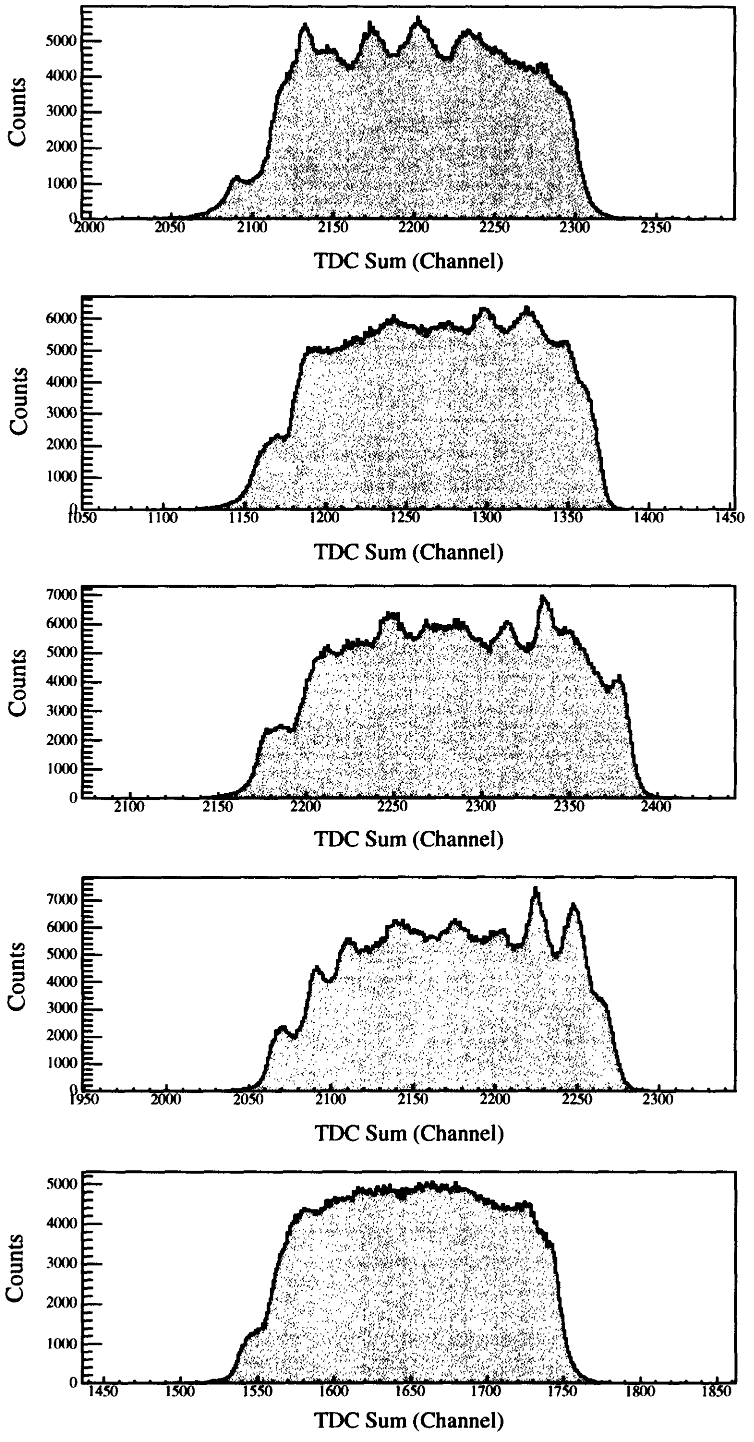

Figure 3-11: Raw time-sum spectra (TDC_{left} + TDC_{right}) for cosmic ray events. Time scale is TDC channels.

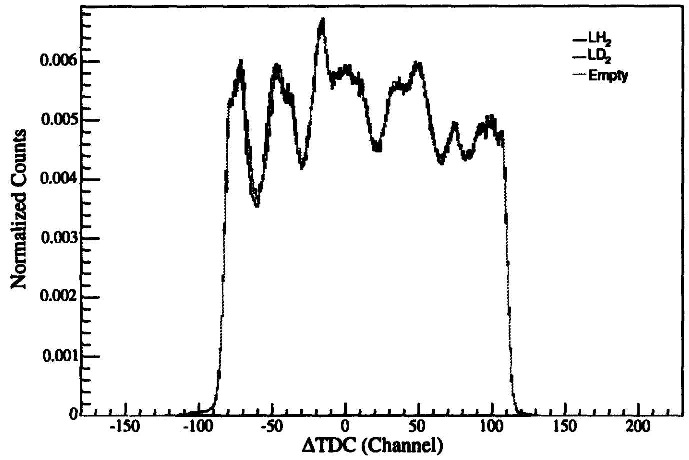

Figure 3-12: Normalized cosmic ray time-difference spectra for middle neutron bar from LH_2, LD_2 and empty target run periods. Each histogram is normalized by the respective total number of events.

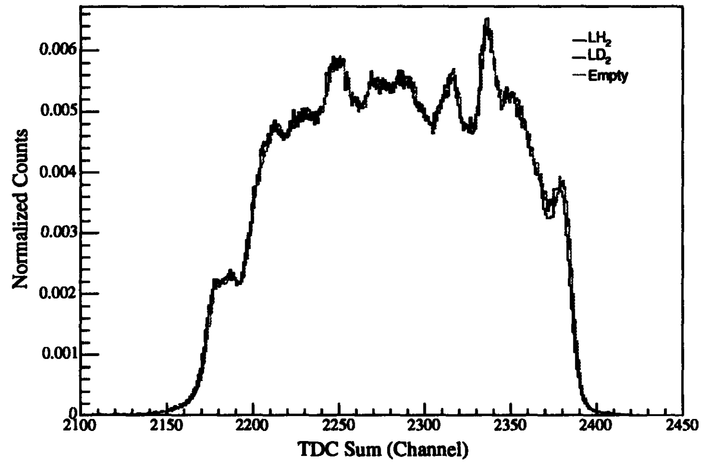

Figure 3-13: Normalized cosmic ray time-sum spectra for middle neutron bar from LH_2, LD_2 and empty target run periods. Each histogram is normalized by the respective total number of events.

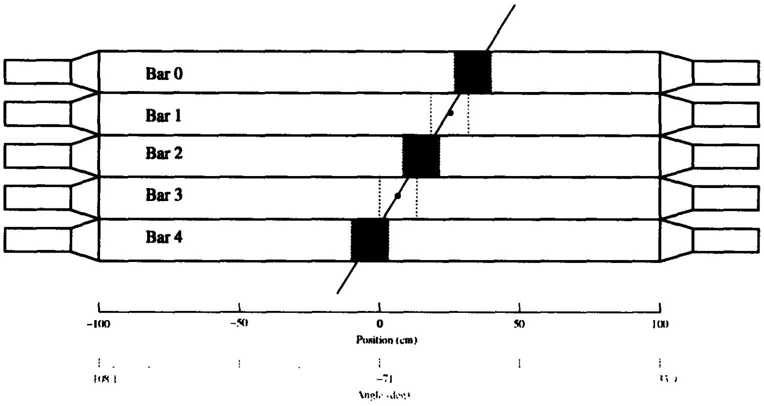

Figure 3-14: Schematic view of a cosmic ray triggering all five neutron bars. Position along each bar was determined using TOF_{left} - TOF_{right}. Information from bars 0, 2 and 4 helped define a first-order polynomial fit which yielded position estimates for the remaining bars 1 and 3. The discrepancy between the estimated and measured positions for these bars appears in figure 3-15.

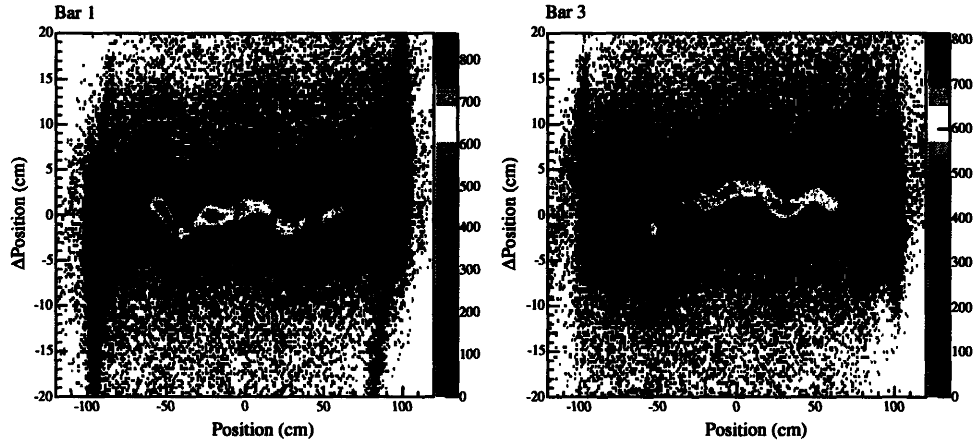

Figure 3-15: Discrepancy between estimated and measured cosmic event positions along bars 1 and 3 as a function of position along the bars (zero corresponds to the center of each bar).

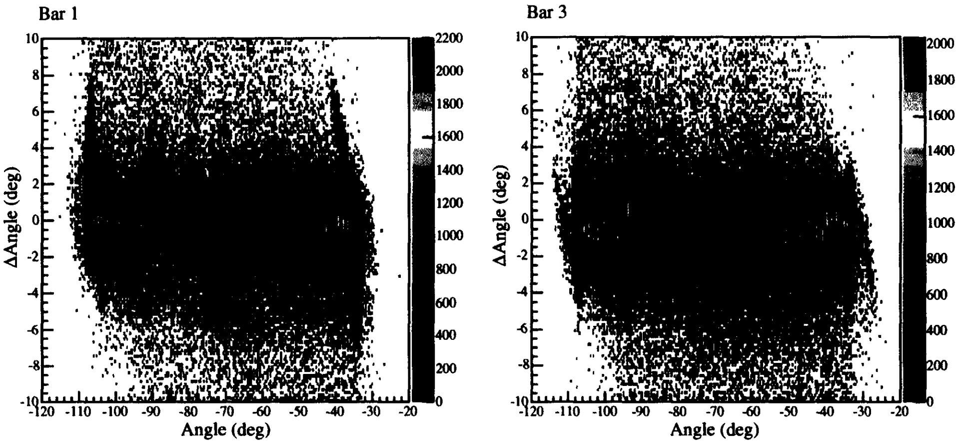

Figure 3-16: Discrepancy between estimated and measured cosmic event angular positions for bars 1 and 3 as a function of neutron scattering angle.

3.2.4 Pulse Height to Energy Conversion

The pulse height information from the five neutron bars is not used directly in the analysis of the data. By this we mean that the pulse height information does not define any kinematic variables of the scattering. Nonetheless, it is essential for establishing the neutron detection efficiency of the neutron bars. Section 4.2 will provide additional details on the procedure for establishing the efficiency of the neutron bars. Here it suffices to say that this efficiency is a strong function of the detector thresholds. To guarantee that all bars operate with the same detection efficiency, their discriminator thresholds are intentionally set quite low while the final thresholds are applied in software. This method relies on an accurate pulse height-to-energy calibration of the bars. The assumption that the pulse height is a linear function of the energy deposited in a bar suggests that two coefficients are required to implement this conversion. Therefore, we need at least two processes which deposit two different amounts of energy in a bar. Furthermore, to improve the accuracy of the applied thresholds, the two calibration energies should straddle the threshold energy, which is on the level of 5 MeVee. Fortunately, the minimum ionizing cosmic rays and the gamma rays from a PuBe source fit the description perfectly. Their use for the neutron bar energy calibration is discussed in the sections which follow.

One subject that must be addressed before we proceed with the discussion of the energy calibration is the issue of light attenuation in the scintillator material of the bars. The effect of the light attenuation is to render the ADC pulse height dependent on the distance of the event from a given phototube. To investigate this dependence, we collected ADC spectra for a collimated ^{60}Co source placed at various locations along the bar. One way to correct for this effect would be to adjust the pulse height of each event according to the light attenuation curves found during this procedure. This approach, however, relies on the accurate determination of the event's position. To avoid possible errors caused by uncertainties in position we chose to use a more robust method, which was first described in ref. [12]. The method is based on the fact that while the pulse heights of the individual left and right phototubes exhibit mild decaying exponential dependence on event's position along the bar, their geometric mean, $\overline{\mathrm{ADC}}_{geo}$, stays approximately constant along the entire length of the bar. The following equation gives a mathematical definition of thle geometric mean:

$$\overline{\mathrm{ADC}}_{geo} = \sqrt{\mathrm{ADC}_{left} \times \mathrm{ADC}_{right}}. \tag{3.2}$$

Therefore, we seek a linear map which will transform the position-independent $\overline{\mathrm{ADC}}_{geo}$ pulse height to the energy deposited in a bar by the event of interest.

3.2.4.1 Minimum Ionizing Energy with Cosmic Rays

The minimum ionizing cosmic rays are naturally occurring high energy events. They are selected via the *cosmic* trigger as was previously discussed in section 2.6.3. Figure 3-17 shows a schematic view of a typical cosmic ray event. In our setup a multiplicity module required that at least three neutron bars fired during each cosmic event. The total amount of energy deposited in each bar is

$$E_{deposited} = \frac{dE}{dx} \cdot \Delta x \cdot \rho_{BC408}, \tag{3.3}$$

where $dE/dx = 2.1$ (MeV cm^2/g) is the amount of energy deposited by a minimum ionizing particle per unit path length, Δx is the total distance traveled in the bar, and $\rho_{BC408} = 1.032$ (g/cm^3) is the density of the plastic scintillator material BC408.

To determine the path length in each bar, we reconstructed the cosmic track by fitting a straight line to the locations of the particle hits in the 5-bar neutron wall. The horizontal coordinates of each hit were derived from the TOF$_{left}$-TOF$_{right}$ spectra, while the vertical coordinates were set to the location of the centerline of the triggered bar. A plot of the slopes of all cosmic tracks appears in figure 3-18. To avoid the infinities in the usual definition of the

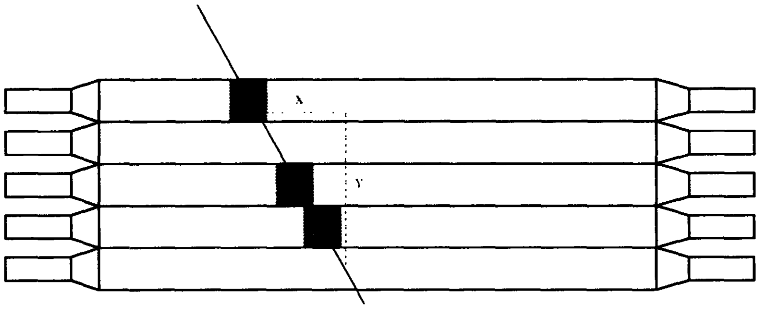

Figure 3-17: Schematic view of a cosmic ray event.

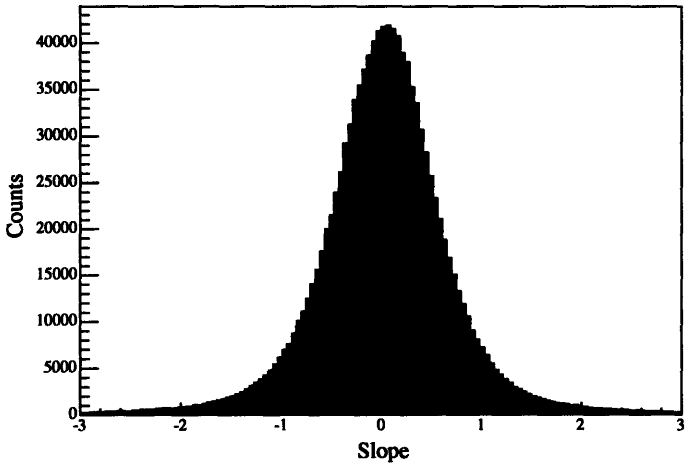

Figure 3-18: Distribution of measured slopes from cosmic ray events. The slope is defined so that the vertical rays would have a slope of zero.

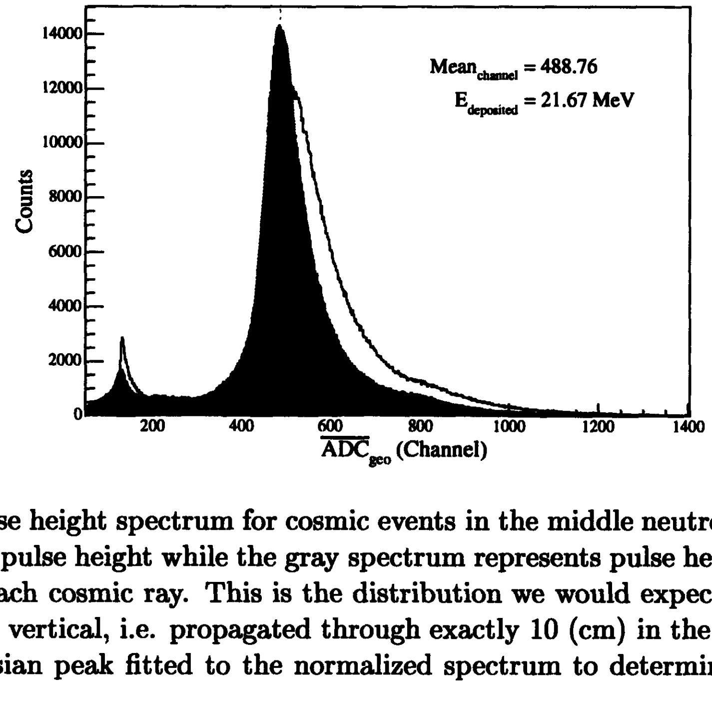

Figure 3-19: Pulse height spectrum for cosmic events in the middle neutron bar. The red curve shows raw mean pulse height while the gray spectrum represents pulse heights scaled according to the slope of each cosmic ray. This is the distribution we would expect to see if all incident cosmic rays were vertical, i.e. propagated through exactly 10 (cm) in the bar. The green curve marks the Gaussian peak fitted to the normalized spectrum to determine the position of the mean.

slope of $\frac{Y}{X}$ for vertical rays, the slope was defined as $\frac{X}{Y}$ instead. Therefore, all vertical cosmic ray events boasted a slope of zero.

Figure 3-19 shows a distribution of cosmic pulse heights measured by the middle bar. The red curve denotes the raw $\overline{\mathrm{ADC}}_{geo}$ pulse heights. These, however, are not terribly useful because they represent energies deposited by the cosmic rays traversing the bar at various angles of incidence, as suggested by their slope distribution in figure 3-18. Since the path length of the cosmic events in the bar, and, therefore, the amount of deposited energy, varies with the angle of incidence, the red spectrum should not be used for energy calibration purposes. Instead, we wish to consider only those rays which leave the same known amount of energy in the bar, e.g. the vertical rays. We can use the slope information for each cosmic event to estimate the pulse height it would produce if it were to strike the bar at normal incidence. This procedure is legitimate if we assume that the pulse height, $\overline{\mathrm{ADC}}_{geo}$, is proportional to the amount of deposited energy, while equation 3.3 tells us that the amount of deposited energy is proportional to the distance traveled in the plastic scintillator, Δx. Then, using our definition of the slope, the required transformation is given by

$$\text{Normalized } \overline{ADC}_{geo} = \frac{\overline{ADC}_{geo}}{\sqrt{1+s^2}}, \tag{3.4}$$

where s is the slope of the incident cosmic ray as we defined it and the $\overline{\mathrm{ADC}}_{geo}$ is the geometric mean of the pulse heights from left and right phototubes. The normalized pulse height spectrum is shown in gray in figure 3-19. This normalization procedure ensures that the peak in this spectrum is produced by the cosmic events which deposit 21.67 MeV in traversing 10 cm of the bar. We fitted a Gaussian function to this peak in order to find the location of the mean. Table 3.1 summarizes peak locations for all five bars.

3.2.4.2 Compton Edge with PuBe Source

The Compton scattering of gamma rays of known energy from the electrons in the scintillator bars provides the second energy calibration point. We chose to use a PuBe source for this measurement. An intimate mixture of ^{238}Pu, which decays primarily by alpha-particle emission, and ^{9}Be emits neutrons and gamma rays in coincidence through a nuclear reaction in which beryllium absorbs an alpha particle and forms ^{12}C in the first excited state.[3] The emitted

---

[3] If ^{12}C is formed in the ground state through the reaction $^{9}\mathrm{Be} + \alpha -- >{}^{12}\mathrm{C}_{g.s.} + n$ no γ-ray is emitted. There is insufficient energy to produce higher excited states of ^{12}C.

Bar N°	PuBe Compton Edge (4.4 MeV)	Cosmic Rays Minimum Ionizing (21.67 MeV)
0	178.0	485.1
1	172.0	478.8
2	208.0	488.8
3	169.0	450.2
4	164.0	463.0

Table 3.1: Summary of pulse height to energy conversion coefficients for neutron bars.

gamma rays have energy of 4.4 MeV. The following equation gives the maximum amount of energy which can be transferred to an electron via the Compton process:

$$E_{max} = h\nu\frac{2\epsilon}{1+2\epsilon}, \qquad \text{where} \quad \epsilon = \frac{h\nu}{m_e c^2}. \tag{3.5}$$

In the above expressions, $h\nu$ gives the initial energy of a gamma ray, while m_e denotes the mass of an electron. According to equation 3.5, the maximum detected energy, or the "Compton edge" energy, for these gamma rays is 4.159 MeV.

To identify PuBe events in the data stream, an additional liquid scintillation neutron detector was placed about 1.5 meters behind the neutron wall such that the radioactive source was now between the neutron wall and the extra detector. A coincidence between any neutron bar and the stand-alone neutron detector formed the PuBe trigger. Similar to the cosmic trigger, the PuBe trigger was vetoed during beam bursts and the source data were collected only in the absence of beam neutrons to minimize the number of accidental coincidences.

Figure 3-20 shows a plot of TDC vs $\overline{\text{ADC}}$ values for PuBe events detected in the liquid scintillator. The horizontal locus at the top of the two-dimensional histogram corresponds to neutrons, while the bottom locus is populated by γ-rays. A simple rectangular cut (red) selected only those events in which a coincident neutron was detected in the PuBe liquid scintillator while its conjugate γ-ray hit the neutron wall. Those events which passed this graphical cut comprise the neutron bar $\overline{\text{ADC}}$ spectrum in figure 3-21. The figure shows a well-defined Compton edge. The point half the way along the edge corresponds to the energy of 4.159 MeV, [13].

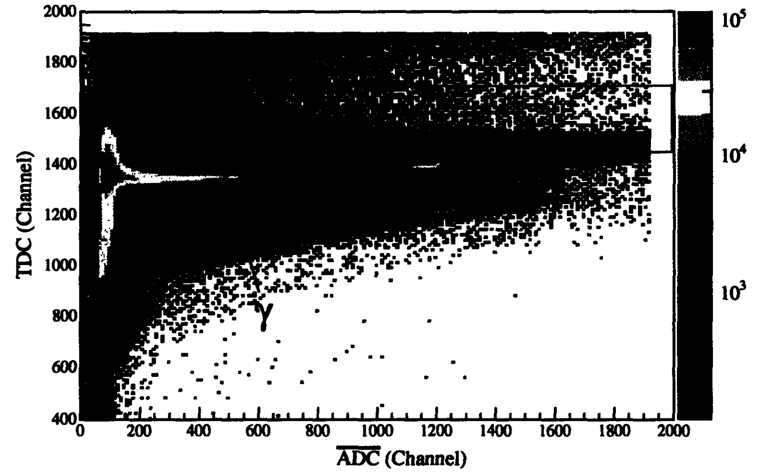

Figure 3-20: TDC vs $\overline{\text{ADC}}$ for PuBe events in the PuBe liquid scintillator. The red rectangle shows the cut used to select coincident neutrons.

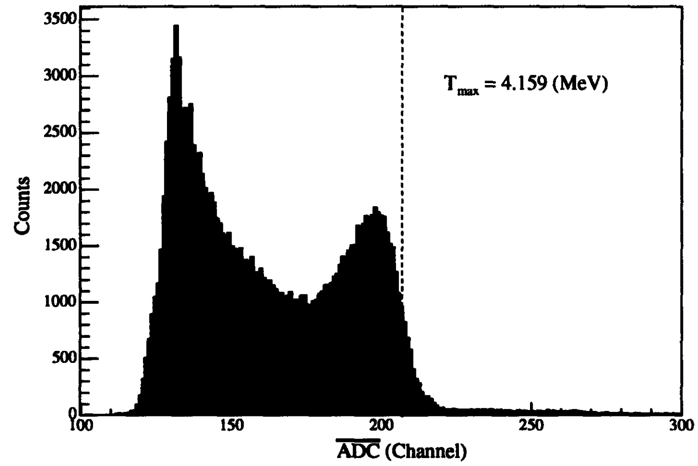

Figure 3-21: Compton edge spectrum for 4.4 MeV γ-rays from PuBe source detected in the middle neutron bar. These are γ-ray events whose conjugate neutron passed the graphical cut shown in figure 3-20.

Chapter 4

Data Analysis

4.1 Incident Neutron Flux

The ability to reliably and continuously monitor the neutron beam flux allows one to extract an absolute cross section from the experimental data. In the present experiment this measurement was facilitated by a fission ionization detector, or *fission chamber*, (see section 2.3). This detector was placed in the incident neutron beam roughly 1.5 meters upstream from the cryogenic target. The fission chamber itself was made up of several thin stainless steel foils with deposits of a fissionable material, such as ^{238}U. To measure the neutron flux, one relies on detecting the signals from fission fragments produced by the neutron induced fission of ^{238}U. The device is able to monitor the flux of neutrons of incident energies in the range of a few MeV up to 800 MeV. Fission chamber yields are readily converted to the incident neutron flux, provided that one knows the areal density and the energy-dependent fission cross section of ^{238}U with sufficient accuracy.

4.1.1 Fission Chamber Data

During the experiment, the fission chamber generated a separate trigger type. Each fission event consisted of two pieces of information: the incident neutron time of flight and the pulse height of the fission chamber output.

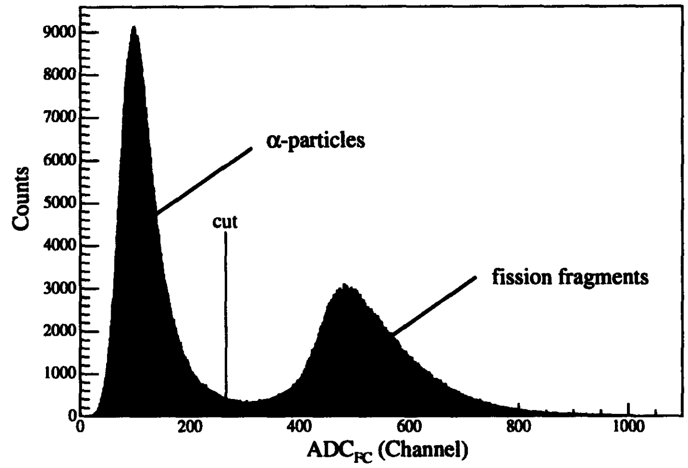

Figure 4-1: Fission chamber pulse height spectrum.

The pulse height information helped separate neutron-induced fission events from the background due to time-random alpha decays of the fissionable material and alpha knockout reactions which occur in the stainless steel backing foil. Figure 4-1 shows a plot of the fission chamber pulse height. The detected fission fragments form the wider peak on the right. To isolate it from the background events populating the peak on the left, we devised an adaptive mechanism. The mechanism is based on fitting a second degree polynomial to the region between the two peaks on a run-by-run (2 hours) basis. Each time the parabola is fitted, the code finds the location of its minimum and sets a cut just to the left of it. The cut was offset by 40 channels to the left of the location of the minimum to ensure that no fission fragment events would be eliminated by the cut. Figure 4-2 shows the same cut in the plot of correlation of fission chamber pulse height to the incident neutron time of flight. This figure verifies that no events of interest were discarded by the cut.

A comment about the stability of the ADC_{min} location is in order. To verify that the performance of the fission chamber did not vary noticeably with time, we measured the location of the ADC minimum for each 2-hour run and plotted it as a function of time in figure 4-3. The red open circles represent these measurements. Their error bars reflect the uncertainty in the parameters of the parabolic fit. These data are compared to the prediction of the location of the ADC minimum based on the cumulative fission chamber ADC histogram, collected over the entire run period (dark gray curve). The light gray band marks the uncertainty in the

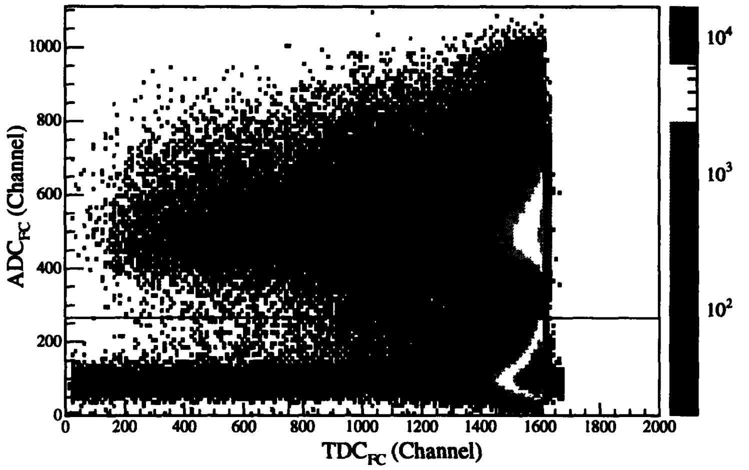

Figure 4-2: ADC vs TDC spectrum for fission events. The red line marks a cut based on the pulse height information. Every event above the line is counted toward the incident neutron beam flux.

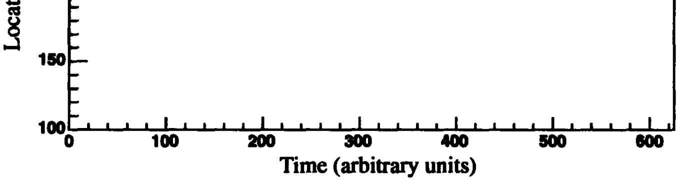

Figure 4-3: Stability of the fission chamber ADC cut.

parameters of the fit to the cumulative histogram. As expected, this uncertainty diminishes over time with improving statistics. The figure tells us that the location of the ADC$_{min}$ for each 2-hour run did not vary significantly from the value calculated using cumulative fission ADC histogram. Therefore, our use of the cumulative histogram for this purpose in the analysis is justified.

The time of flight information, also contained in each fission event, was crucial in the evaluation of the kinetic energy of incident neutrons. A raw TDC spectrum from the fission chamber is shown in figure 4-4. The timing electronics were setup so that the fission chamber started the timer while a delayed copy of the t_0 signal from the accelerator stopped it. This made the raw TDC$_{FC}$ spectrum appear inverted, with larger TDC channel numbers corresponding to shorter times of flight. The conversion from TDC channel number to particle time of flight is a linear map and, therefore, requires two independent coefficients. The multiplicative scaling coefficient was determined at the end of the run period using a high-precision time-calibrator. Each TDC channel was found to correspond to 0.617 nsec. Besides this conversion factor, we need the correct offset to find the absolute time of flight. The offset depends on many factors, including the amount of delay of the associated t_0 signal, the electronic delays, etc. This fact made calculating the offset impractical. A direct measurement of this coefficient was needed instead. The "γ flash" facilitated such a measurement. These are photons which originate at the spallation target and propagate through to our apparatus just ahead of the fastest neutrons. The "γ flash" can be clearly seen in the raw TDC spectrum of figure 4-4. Knowing that the fission chamber is located 1545.0 cm away from the spallation target, it becomes a trivial matter to constrain the time offset. A plot of beam neutron absolute time of flight is shown in figure 4-5.

In addition to aiding in the TDC calibration the "γ-flash" peak gives an estimate of the fission chamber energy resolution. Figure 4-6 shows a plot of the difference of computed and measured times of flight for the "γ-flash" events seen by the fission chamber. The sigma of the Gaussian function fitted to the peak is 1.073 (nsec), which translates to energy resolution of roughly 5 MeV at 200 MeV beam energy. Therefore, 5 MeV is the low bound on the width of the energy bin which can be used in extracting experimental cross sections. A compromise of 10 MeV-wide energy bins, which gave us adequate energy resolution without hurting statistical accuracy, was used in the actual analysis.

The incident energy of the beam neutrons can now be calculated using the following equation:

$$E_{n_0} = \gamma m_n = \frac{m_n}{\sqrt{1 - \left(\frac{L_{FC}}{t_n c}\right)^2}}. \tag{4.1}$$

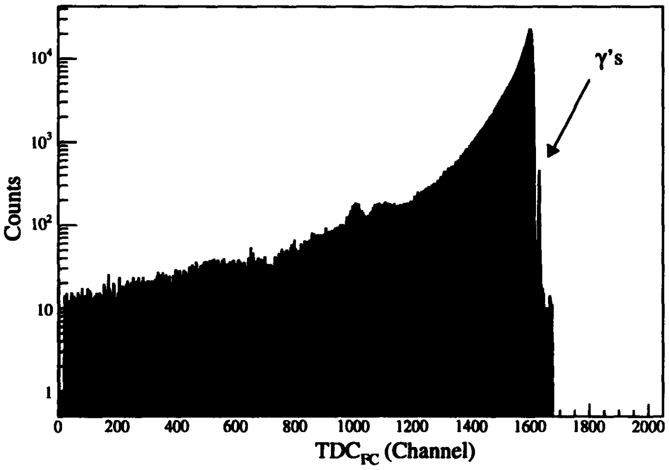

Figure 4-4: Fission chamber TDC spectrum.

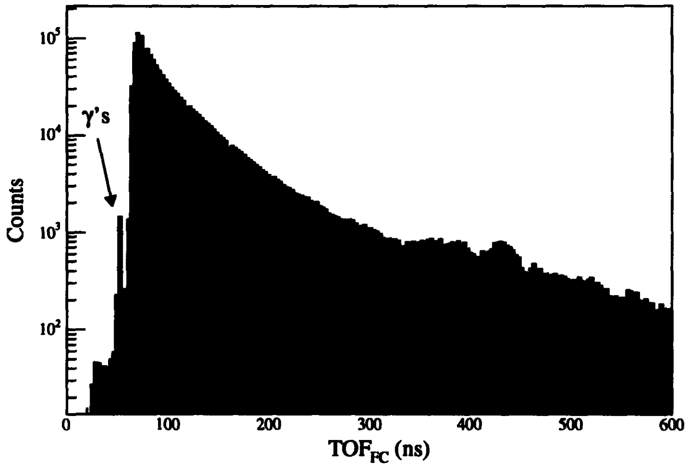

Figure 4-5: Fission chamber time of flight spectrum.

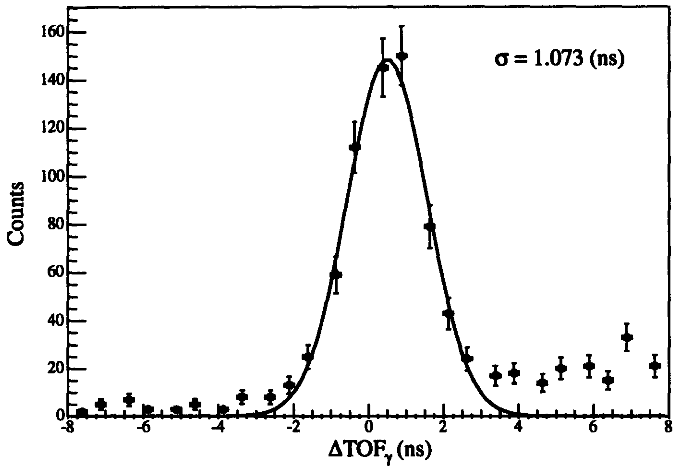

Figure 4-6: Timing resolution of the fission chamber.

where L_{FC} is the distance of the fission chamber from the spallation target, 1545.0 (cm), m_n is the energy equivalent of the neutron mass in (MeV), and c is the speed of light in (cm/nsec). Figure 4-7 shows a plot of fission chamber yield as a function of incident neutron kinetic energy.

4.1.2 Integrated Beam Flux

The relation between the number of fission events and the number of beam neutrons is given by the following equation:

$$N_f(E) = N_i(E) \cdot \rho_f \cdot \epsilon_f \cdot \sigma(E) \tag{4.2}$$

where $N_f(E)$ is the number of fission events, $N_i(E)$ is the number of incident neutrons, ρ_f is the areal density of ^{238}U, ϵ_f is the efficiency with which fission fragments are detected, and $\sigma(E)$ is the fission cross section. The areal density was measured directly by looking at the yield of the alpha particle spectrum with a silicon surface-barrier detector, along with the known decay rates of ^{238}U. The measured value for ρ_f is $0.9080 \cdot 10^{-6}$ atoms/barn, as reported in [11]. The detection efficiency, ϵ_f, is high but not unity: this is because some of the fission fragments are released nearly parallel to the plane of the foil and escape without being detected. This efficiency was estimated to be 0.98 by [11] from analysis of detector geometry.

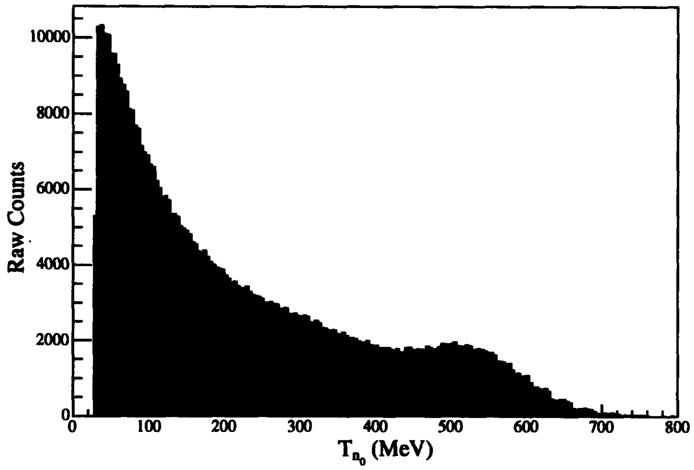

Figure 4-7: Fission chamber yield as a function of incident beam energy.

The most significant source of systematic uncertainty in the experiment is the fission cross section of ^{238}U. Figure 4-8 shows a plot of this cross section as a function of the incident neutron kinetic energy. For beam energies up to around 100 MeV the cross section is known to better than 5%. Most of the *n–p* and *n–d* elastic data, however, were analyzed at beam energies near 200 MeV, where there are no fission cross section data. The spline interpolation between the data points at 120 MeV and 380 MeV leads to an uncertainty of about 10% in the overall normalization of the elastic *n–d* cross section. This uncertainty was further minimized by normalizing the *n–d* elastic cross section to the measured *n–p* elastic cross section. Section 4.4 offers details of the *n–p* elastic cross section calculation and normalization.

4.2 Detector Efficiencies

The detection efficiencies of neutron and charged particle detectors, ϵ_n and $\epsilon_{p,d}$, appear directly in the equations for differential scattering cross sections 4.10 and 4.13. Since charged particles lose their energy in a detector continuously, primarily via Coulomb interactions with atomic electrons, the efficiency with which they can be detected nears 100%. At the same time, neutrons rely on the strong interaction to be detected. This results in a low detection efficiency for neutrons, roughly of the order of 10%. The methods used to determine exact values of the detector efficiencies are described in the following sections.

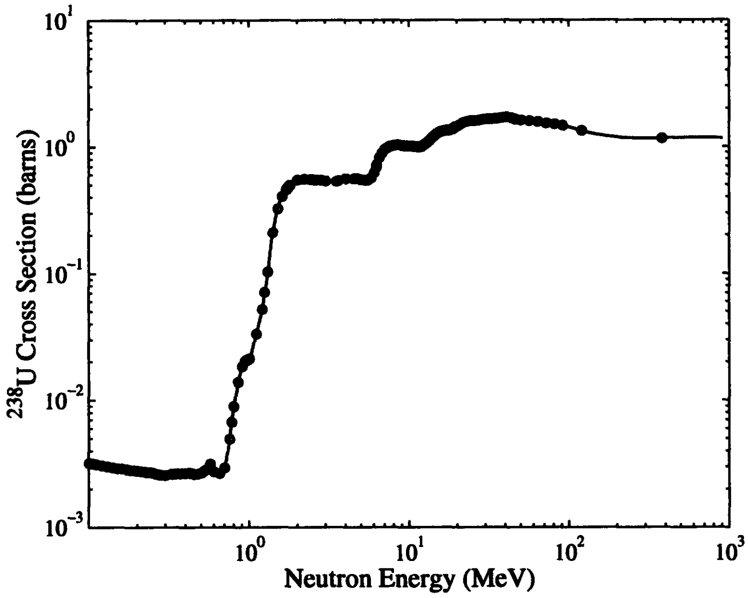

Figure 4-8: ^{238}U fission cross section from [10].

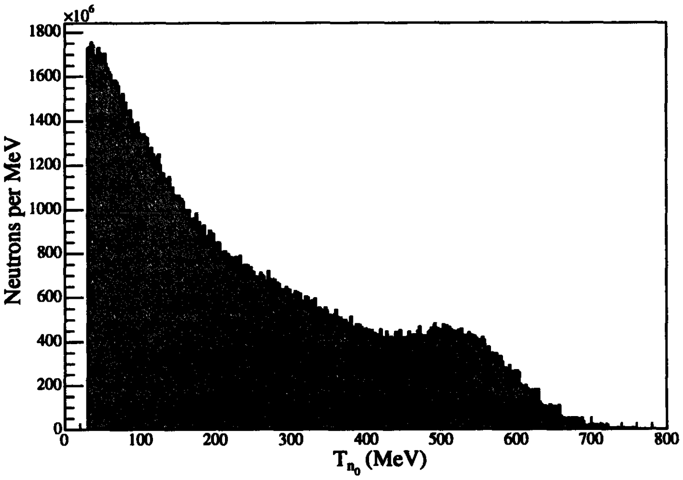

Figure 4-9: Integrated neutron beam flux.

4.2.1 Proton Detectors

The probability of detecting a charged particle in a detector is close to unity. Therefore, when we speak of the charged particle detection efficiency, we refer primarily to the efficiency of the PID (particle ID) cuts in identifying this particle as a good event.

In the *n–p* elastic analysis the procedure to find the efficiency of the E vs ΔE cut (see figure 4-15) is rather straightforward. Things are made easier by the fact that the *n–p* elastic is by far the dominant process and any contribution due to secondary processes can be neglected. Therefore, the efficiency is the ratio of the number of events which pass the cut to the total number of events in the histogram. For the case of *n–p* elastic scattering at 200 MeV, this efficiency was about 94%.

In the *n–d* elastic analysis the matters are complicated by the possible presence of quasielastic *n–p* events, e.g. in figure 4-17. However, the *n–d* kinematic cuts, applied to the data, eliminate most of the unwanted events and make the task of setting the graphical PID cut easier and more reliable. For instance, the PID cut in figure 4-17 is quite unambiguous and its efficiency can be estimated by the ratio of the number of events which pass the cut to the number of events in the *n–d* locus. For the case of *n–d* elastic scattering at 200 MeV into 36° telescope, presented in section 4.5, the efficiency of the PID cut was around 98%. This number represents the probability that a given recoil deuteron which made it to the CsI counter intact will be counted as a good *n–d* event. The actual detection efficiency is smaller than this number, however, because there exists a finite probability that the said deuteron will break up en-route, never reaching the detector. The break up is most likely to happen inside the liquid deuterium target flask. Even though the remnants of the deuteron may reach a charged particle telescope, the event they trigger will be most likely discarded on the grounds of unrecognizable kinematics.

4.2.2 Neutron Detectors

Unfortunately, neutron detectors sport only a fraction of the detection efficiency of charged particle detectors. They rely on the interactions of neutrons with the nuclei in the scintillating material via the strong nuclear force. Compared with small-angle Coulomb scattering, such interactions have a relatively low probability of occurring. Neutron detectors depend on detection of the scintillation light produced by recoil protons, primarily from elastic *n–p* scattering.

Since elastic *n–p* scattering can produce a recoil proton at any angle in the range 0° – 90° with energies ranging continuously from $E_p = E_n$ (for 0°) to $E_p = 0$ (for 90°), the neutron detection efficiency will depend on the recoil proton detection threshold. Figure 4-10 illustrates the integral efficiency of one 4 in.×4 in.×80 in. bar as a function of the threshold energy. The most interesting feature of this plot is that when the threshold energy is at around 4 MeVee[1] the integral efficiency of the neutron bar stays close to 10% independent of neutron energy. This regime is very attractive for our measurement in which the energies of the scattered neutrons vary greatly.

The most direct way of securing this condition for all neutron bars was to set hardware thresholds for all neutron detectors well below 4 MeVee and subsequently apply software thresholds at the 4 MeVee level. The hardware thresholds needed to be set low enough to allow for light propagation attenuation inside a 2 meter long BC408 scintillator bar. The software thresholds were applied to the geometric mean of the ADC values of the left and right phototubes for each bar. Section 3.2 gives more details on the pulse height to energy calibration and light attenuation in the bars.

4.3 Elastic Kinematics

The form of the kinematic relations, presented in this section, is that given by T. Akdoğan in [10] for *n–p* elastic scattering. The equations have been slightly modified to extend their use to *n–d* elastic scattering, i.e. the case of unequal masses of the incident and target particles. These equations assume only that the two particles are scattered elastically, and, therefore, are applicable to both *n–p* and *n–d* elastic scattering, provided that appropriate value for the mass of recoil charged particle, m_r, is specified. Of great interest to us is the relation which maps the incident beam kinetic energy, T_{beam}, and the recoil angle of the charged particle, θ_r, to the energy of the charged particle, E_r. We proceed by writing the condition of total four-momentum conservation before and after the reaction has taken place:

---

[1] 1 MeVee (1 MeV electron equivalent) is defined by the amount of light produced in a scintillating material when an incident electron deposits 1 MeV of its energy in the material.

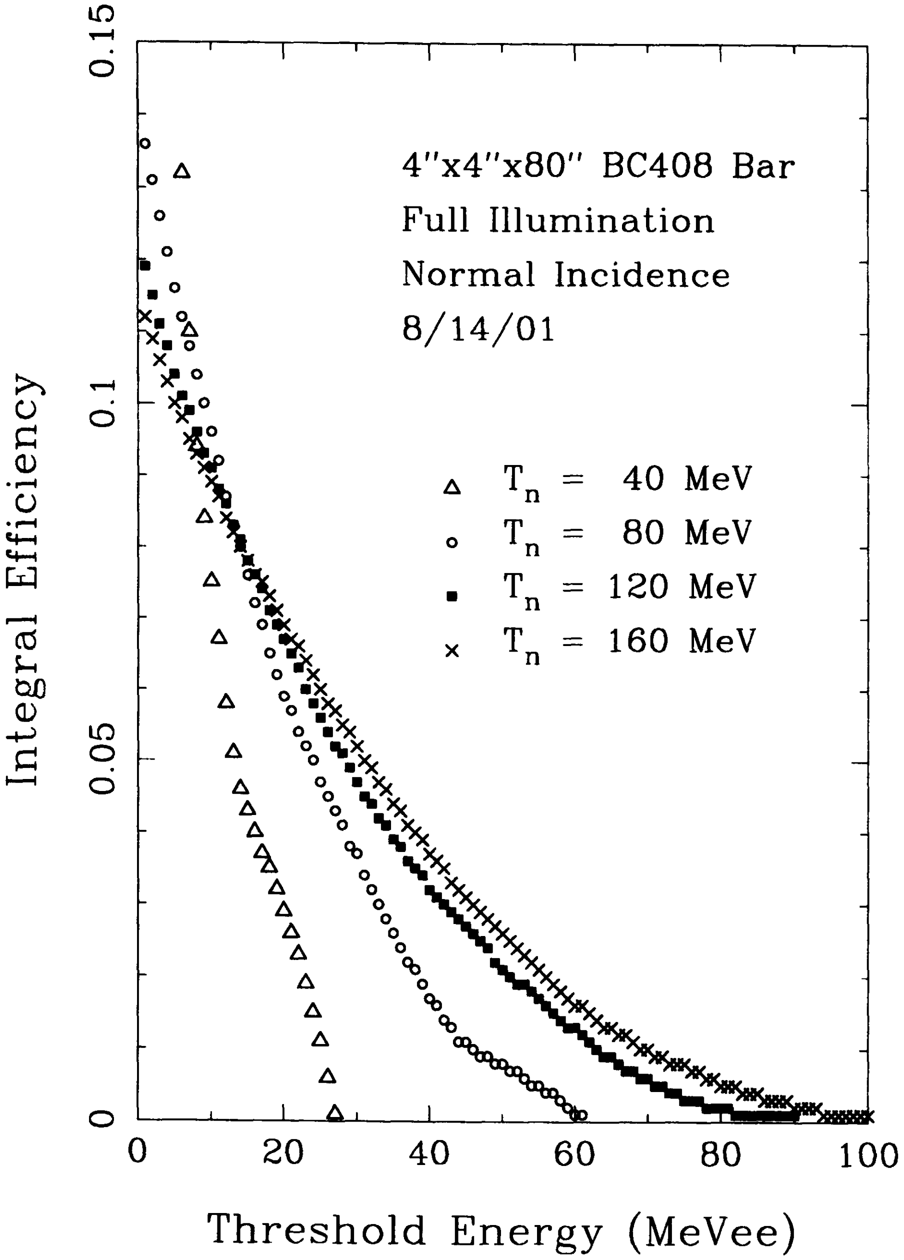

Figure 4-10: Neutron bar integral efficiency from [13].

$$\begin{aligned} P^{\nu}_{n_0} + P^{\nu}_{t} &= P^{\nu}_{n} + P^{\nu}_{r} \\ P^{\nu}_{n} &= P^{\nu}_{n_0} + P^{\nu}_{t} - P^{\nu}_{r} \\ [P^{\nu}_{n}]^2 &= \left[P^{\nu}_{n_0} + P^{\nu}_{t} - P^{\nu}_{r}\right]^2 \\ 0 &= m_r(E_{n_0} + m_r) - E_r(E_{n_0} + m_r) + P_r P_{n_0} \cos\theta_r \\ E_r &= m_r \frac{\alpha^2 + 1}{\alpha^2 - 1} \qquad \alpha \equiv \frac{E_{n_0} + m_r}{P_{n_0} \cos\theta_r}. \end{aligned} \tag{4.3}$$

Furthermore, it is often necessary to calculate the conjugate neutron scattering angle if T$_{beam}$ and E$_r$ are known. The following equation should do the job:

$$\tan\theta_n = \frac{P_r \sin\theta_r}{P_{n_0} - P_r \cos\theta_r}. \tag{4.4}$$

By symmetry, the neutron parameters and the conjugate charged particle angle can be calculated by using the beam energy and the neutron angle as follows:

$$\alpha \equiv \frac{E_{n_0} + m_r}{P_{n_0} \cos\theta_n} \qquad E_n = m_n \frac{\alpha^2 + 1}{\alpha^2 - 1} \quad , \quad \tan\theta_r = \frac{P_n \sin\theta_n}{P_{n_0} - P_n \cos\theta_n} \tag{4.5}$$

It is often necessary to express the measured elastic cross section as a function of the center of mass angle θ^* in order to compare it with the data in the literature. To accomplish this, one needs an expression for Jacobian, $\frac{d\Omega}{d\Omega^*}$. We start by writing an expression for a boost, which facilitates transformation into the center of mass frame

$$\vec{\beta}_{c.m.} = \frac{\vec{P}_{n_0} + \vec{P}_t}{E_{n_0} + E_t} \qquad \gamma_{c.m.} = \frac{1}{\sqrt{1 - \vec{\beta}_{c.m.} \cdot \vec{\beta}_{c.m.}}}, \tag{4.6}$$

where $\vec{P}_t$ and E_t are momentum three-vector and energy of target nucleus. Having computed the value of $\gamma_{c.m.}$ it is, then, possible to relate recoil angle in lab and center of mass frames as follows

$$\begin{aligned} \tan\theta_r &= \frac{\sin\theta^*_r}{\gamma_{c.m.}(\cos\theta^*_r + 1)} \\ \tan\frac{\theta^*_r}{2} &= \gamma_{c.m.} \tan\theta_r. \end{aligned} \tag{4.7}$$

What remains is to take the derivative of the above equations with respect to θ. Using the definition of solid angle differential $\mathrm{d}\Omega = 2\pi \sin\theta \mathrm{d}\theta$ we obtain the following expressions for Jacobian, both as a function of lab angle and center of mass angle:

$$\frac{\mathrm{d}\Omega}{\mathrm{d}\Omega^*} = \frac{(1+\gamma_{\text{c.m.}}^2 \tan^2\theta_r)^2 \cos^3\theta_r}{4\gamma_{\text{c.m.}}^2} \tag{4.8}$$

$$\frac{\mathrm{d}\Omega}{\mathrm{d}\Omega^*} = \frac{\gamma_{\text{c.m.}}\left[1+\tan^2(\theta_r^*/2)\right]^2}{4[\gamma_{\text{c.m.}}^2 + \tan^2(\theta_r^*/2)]^{3/2}} \tag{4.9}$$

4.4 Elastic *n–p* Scattering

Elastic *n–p* scattering provides the largest contribution to the number of background events in our experiment. It also, however, serves as an excellent check of the experimental apparatus and analysis techniques. The elastic *n–p* cross section is large in magnitude and is well known. Elastic *n–p* kinematics differ from that of the *n–d* scattering only in the mass of recoil particle. Although due to proton's smaller mass the opening angle between the scattered and recoil particles is reduced compared to *n–d* , the use of the neutron wall, which continuously spans 33.9° to 108.1° on the neutron side, has allowed us to form four coincidence pairs with the charged particle telescopes at their nominal positions. The advantage of measuring the *n–p* cross section in coincidence mode is that the parameters of the neutron arm, such as detector efficiency, measured geometry, timing coefficients, and ADC calibration constants, can be verified.

The following equation gives an expression for the cross section we would like to measure:

$$\frac{d\sigma}{d\Omega_p} = \left(\frac{N_p}{N_i \cdot \epsilon_p \cdot \epsilon_n}\right) \cdot \left(\frac{k}{\Delta\Omega_p \cdot \rho_t \cdot l}\right), \tag{4.10}$$

where N_p is the number of detected protons, N_i is the number of incident neutrons, ϵ_p and ϵ_n are proton and neutron detection efficiencies. In proton singles mode, ϵ_n is set to unity. While these four parameters are energy dependent, the rest are constants: k is the electronic pre-scaler factor for a particular event type (1 for coincidence events, 9 for proton singles), $\Delta\Omega_p$ is the solid angle of the proton telescope ($8.464 \cdot 10^{-3}$ sr) [2], l is the live time of the electronics,

---

[2] The size and placement of the neutron wall guarantees that neutrons conjugate to all detected charged particles (protons/deuterons) will scatter within the solid angle of the wall. Therefore, the solid angle of this measurement is defined solely by the solid angle of the charged particle telescopes, $\Delta\Omega_p$.

estimated by the ratio of the number of recorded triggers to the total number of triggers (85%) as measured by scalers, and ρ_t is the areal density of the liquid hydrogen target. The density of liquid hydrogen is 0.0708 g/cm^3. The effective thickness of the hydrogen target rotated by 50° with respect to the incident beam is assumed to be 1.97 cm. Then, the areal density of target protons, ρ_t, is:

$$\begin{aligned}\rho_t &= \frac{\rho_{H_2} \cdot N_A}{A_{H_2}} \cdot \Delta x \\ &= \frac{0.0708\ \mathrm{g/cm^3} \cdot 6.02 \cdot 10^{23}\ \mathrm{atom/mol}}{1.00794\ \mathrm{g/mol}} \cdot 1.97\ \mathrm{cm}\ \cdot 10^{-24}\ \mathrm{cm^2/barn} \qquad (4.11) \\ &= 8.33 \cdot 10^{-2}\ \mathrm{atom/barn}.\end{aligned}$$

To measure the *n–p* elastic scattering cross section, the target flask is filled with liquid hydrogen. Since our detector geometry allows for valid singles and coincidence trigger types, we will compute the *n–p* elastic scattering cross section for both cases. Let us begin by considering proton singles events.

All events with a ***psingles*** bit set by the DAQ hardware and having acceptable ADC and TDC values (no under- or over-flows) are admitted. The kinetic energy of the incident neutron, T_n, is deduced from the total time of flight of the recoil proton via elastic kinematics maps. A cut on the incident beam energy is applied to select a subset of events with T_n inside an admissible energy bin, e.g. $T_{beam} = 200 \pm 5$ MeV. Events which successfully pass the beam energy cut form a clear locus in a ΔE-E histogram. Figure 4-11 shows a ΔE-E plot for the 42° telescope.

Events which pass a graphical cut denoted by the red oval placed around the locus of *n–p* elastic events, comprise the total number of detected protons, N_p in equation 4.10.

Upon the completion of the analysis of target-full data, target-empty runs are replayed with the same cuts active. The cross section for the target-empty background is computed in a similar way and, once properly scaled by the fission chamber counts to the full-target *n–p* cross section, is subtracted from the target-full data. Figure 4-12 shows the resulting *n–p* elastic scattering cross section. The statistical uncertainty of our measurement is smaller than the size of the symbols. A generous arbitrary systematic error of 10% has been added to each data point. Our results agree well with the prediction of the SAID analysis and the results of previous measurements. This gives us confidence that we understand the systematic parameters of the proton arm of the apparatus.

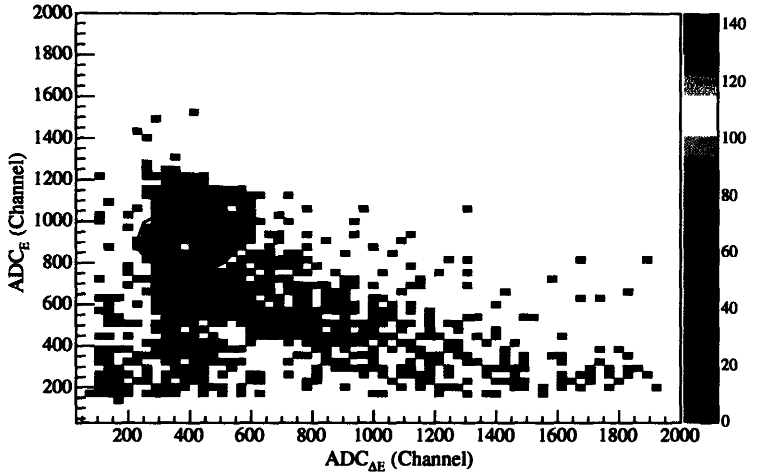

Figure 4-11: ΔE-E plot for proton singles events for n–p elastic scattering at 200 MeV. The amount of energy deposited in a CsI counter by a recoil proton is plotted vs the amount of energy left by the proton in conjugate ΔE detector.

To verify our understanding of the systematic parameters associated with the neutron arm, we repeat the calculation of the n–p elastic scattering cross section in coincidence mode. This regime allows us several additional kinematic observables per each interaction, such as the scattering angle and energy of the neutron. Since all events of interest must obey elastic kinematics, we can significantly reduce the number of background events by requiring that all coincidence neutrons pass scattering angle and total time of flight cuts prior to validating the event as a good n–p event. First, coincidence events are selected from the data stream according the value of *coinc* bit, which is set by DAQ hardware. A coincidence event is one in which one or more proton telescopes have fired in coincidence with one or more neutron bars and no neutron vetos. Such an event should also have valid ADC and TDC values for both proton and neutron arms. Note, that both phototubes of a triggered neutron bar must satisfy this condition. Next, only those events which were generated by an incident neutron of appropriate kinetic energy are selected. As in the proton singles case, we accepted all events with T_{beam} = 200 ± 5 MeV. Making use of the new kinematic observables, we select events based on the total time of flight of the scattered neutron. A typical TOF$_n$ spectrum is shown in figure 4-13. Since each neutron bar has two phototubes, one at each end separated by 200 centimeters, what is actually computed is the mean of the neutron total time of flight. The following equation gives

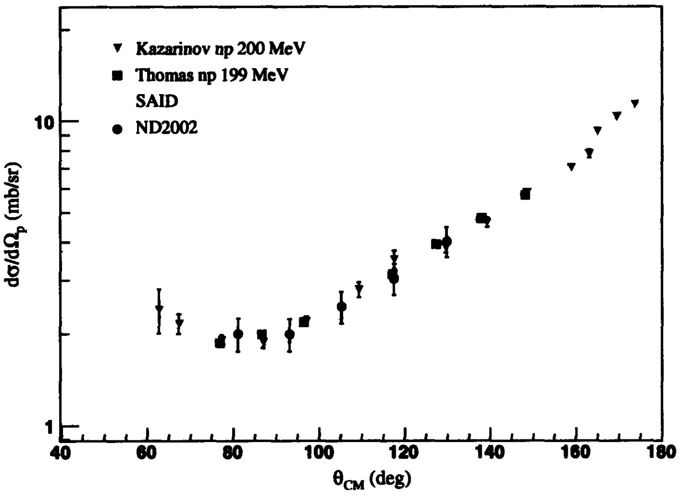

Figure 4-12: n–p elastic cross section at 200 MeV. Proton singles data from present measurement (red circles) are compared with the SAID prediction (gray band) and previous data, found in [14] and [15]. The width of the SAID band reflects the variation in predicted cross section for our beam energy window of 200 ± 5 MeV. During ND2002, the target density ρ_t was multiplied by a factor of 1.45 to correct for bulging of the target windows and the presence of bubbles in the liquid hydrogen.

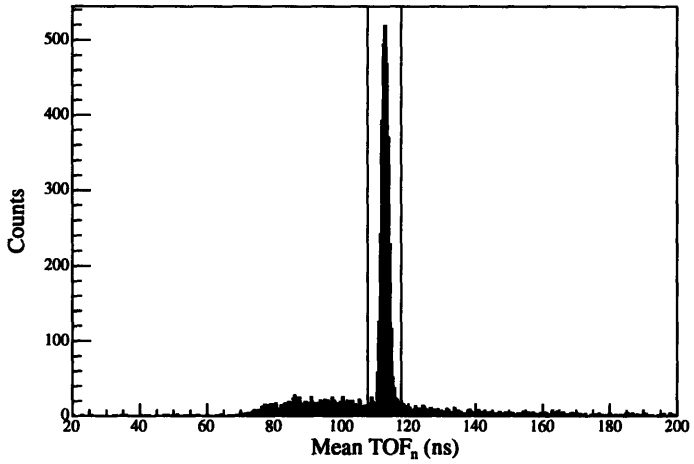

Figure 4-13: Scattered neutron $\overline{\mathrm{TOF}_n}$ for 30° coincidence pair at 200 MeV. Only those events which fall between two red lines satisfy this kinematic cut.

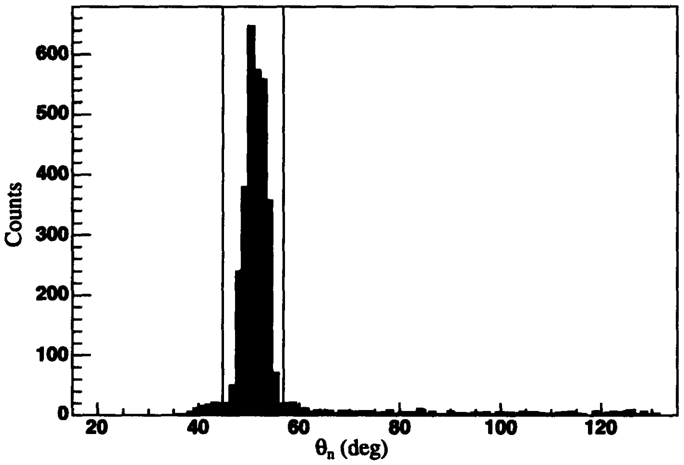

Figure 4-14: Neutron scattering angle for 30° coincidence pair at 200 MeV. Those events which fall between the red lines are admitted as good n–p coincidence events.

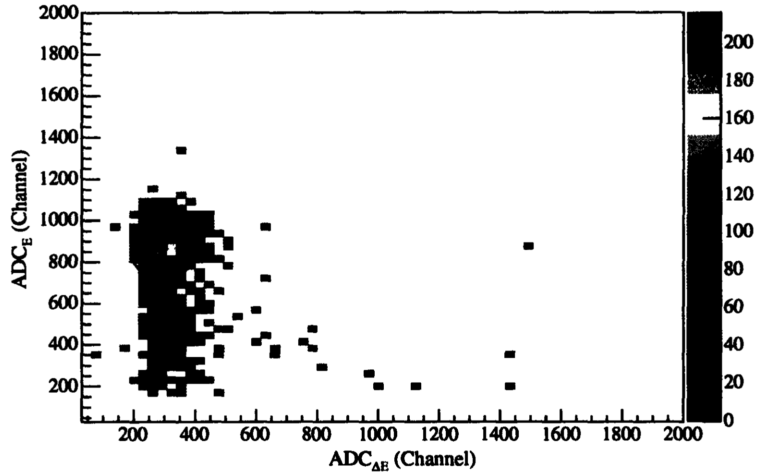

Figure 4-15: ΔE-E plot for coincidence events for *n–p* elastic scattering at 200 MeV.

a more precise definition of the quantity plotted in figure 4-13:

$$\overline{\text{TOF}}_n = \frac{1}{2}\left[\text{TOF}_{left} + \text{TOF}_{right}\right], \tag{4.12}$$

where TOF_{left} and TOF_{right} are times recorded by left and right phototubes. Section 3.2.1 gives a more detailed description of the neutron time of flight calculation. In order to be tagged as a good *n–p* elastic coincidence event, those events which satisfy the neutron time of flight cut must also pass a cut on neutron scattering angle.

Figure 4-14 shows the neutron scattering angle cut for neutrons which belong to the 30° *n–p* coincidence pair. The angle of a scattered neutron is determined from the timing information for the left and right phototube of the struck neutron bar, as per the instructions of section 3.2.2.

Finally, those events which pass the neutron scattering angle cut are counted toward the total number of detected *n–p* events, N_p. A ΔE-E plot for these events is shown in figure 4-15. The kinematic cuts have cleaned up this plot as compared to figure 4-11: all of the inelastic background events were removed from this spectrum. Most of the remaining events form a tight locus of *n–p* elastic events, encircled by the red oval. Those outside the oval, most likely, are legitimate *n–p* elastic events in which detected proton suffered strong interaction losses in the CsI counter.

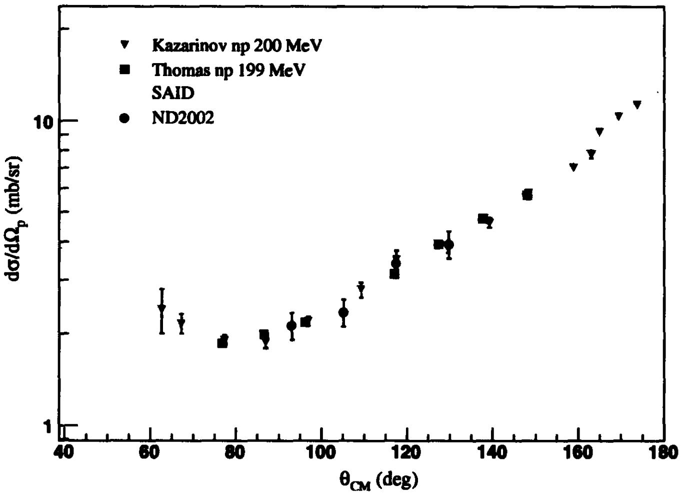

Figure 4-16: n–p elastic cross section at 200 MeV. During ND2002, the target density ρ_t was multiplied by a factor of 1.45 to correct for bulging of the target windows and the presence of bubbles in the liquid hydrogen. Coincidence data from present measurement (red circles) are compared with the SAID prediction (gray band) and previous data, found in [14] and [15]. The width of the SAID band reflects the variation in predicted cross section for our beam energy window of 200 ± 5 MeV.

During a careful visual examination of the cryogenic target upon the completion of the data collection stage of this measurement, we observed that the 2 mil mylar windows of the target flask were permanently deformed. The deformation has most likely happened during the initial stages of the experiment, such that the windows had reached the new equilibrium state relatively quickly and remained there for the duration of the experiment. No significant time variation of the scattered particle rates in the detectors, a sure sign of a varying target thickness, has ever been observed. The bulging forced us to treat the target thickness as a free parameter, whose value could be constrained by the *n–p* elastic cross section. Comparison of the measured *n–p* elastic cross section with the prediction of the partial wave analysis from the SAID database yielded a factor of 1.45, which was consistent with the degree of bulging observed. This figure implicitly includes a correction to the target thickness due to boiling of the liquid hydrogen. Unlike the bulging, the presence of bubbles inside the target flask tends to lower the effective target thickness.

Figure 4-16 shows the differential *n–p* elastic cross section. The data shown were obtained using the corrected target thickness.

4.5 Elastic *n–d* Scattering

The primary goal of this experiment is to measure *n–d* elastic cross section for six recoil angles at several incident beam energies:

$$\frac{d\sigma}{d\Omega_d} = \left(\frac{N_d}{N_i \cdot \epsilon_d \cdot \epsilon_n}\right) \cdot \left(\frac{k}{\Delta\Omega_d \cdot \rho_t \cdot l}\right). \tag{4.13}$$

The meaning of the symbols in the equation above is similar to that in equation 4.10 with the charged particle subscripts changed to reflect the fact that the recoil particle is now a deuteron. The liquid deuterium density of 0.1690 (g/cm^3) and atomic weight of 2 (g/mol) yield a value of 0.1002 (atom/barn) for the areal target density, ρ_t. During the *n–p* elastic analysis of section 4.4 we found experimentally that the actual target thickness was a factor of 1.45 larger than the nominal value. The increase was largely due to the bulging of the target windows, countered only partially by the presence of the bubbles in the boiling liquid hydrogen. With this correction applied, the value of 0.1452 (atom/barn) should be used for the areal target density of the liquid deuterium target, assuming the bulging of target windows and the bubbling the cryogenic liquid were identical for hydrogen and deuterium. The charged particle pre-scale factor, k, was set to 1.

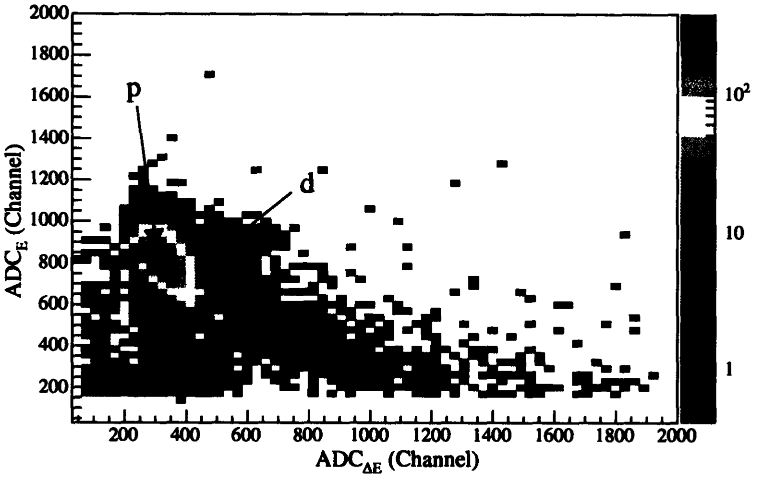

Figure 4-17: E vs ΔE for 200 MeV events in 36° telescope before neutron kinematic cuts.

In principle, elastic *n–d* cross section could be measured by detecting only the recoil deuterons, since the knowledge of the deuteron time of flight and recoil angle fully define elastic kinematics of this reaction. In practice, however, deuteron particle identification is obscured by the large number of quasielastic protons. The cross section for quasielastic *n–p* scattering is roughly sixty times larger than that for the *n–d* elastic scattering. Therefore, this measurement must be done in coincidence mode with both recoil deuteron and scattered neutron being detected. The additional kinematic constraints applied to the scattered neutron significantly ease the event identification and help reduce the number of accepted background events.

The strategy used in the analysis of *n–d* data took on an iterative character. The data were analyzed in several passes. Initially, loose cuts were applied to the data. With each successive pass these cuts were tightened according to the information revealed by the preceding pass. The order in which the cuts were applied was also changed from pass to pass so as to allow tightening of one cut based on a looser version of the other just to have their order switched in the next pass and the process continue. At the end, the procedure was streamlined so that only three passes were needed to establish all of the cuts in their final form. The following is a step by step example of the analysis used to obtain the *n–d* scattering cross section at 200 MeV.

First, we selected coincidence events by considering the value of the *coinc* trigger bit for each event. Those events in which this bit was set by the DAQ hardware were tested to have

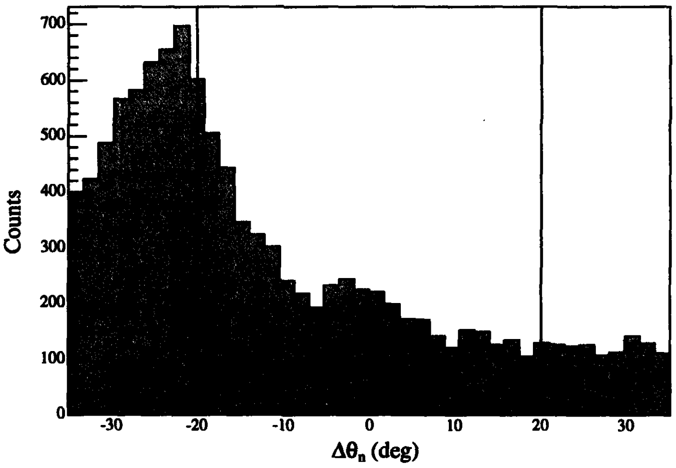

Figure 4-18: A difference of measured and expected neutron scattering angles, $\Delta\theta_n$, is plotted for neutrons conjugate to 36° telescope. The generous cut of *pass 1* is shown by red lines.

valid ADC and TDC values. If passed, these events were plotted on the E vs ΔE histogram. Figure 4-17 shows a typical E vs ΔE histogram. While a cluster of elastic deuterons is certainly visible in the plot, the spectrum is dominated by elastic and quasielastic *n–p* events. Drooping down from the main proton locus are the events which suffered strong interaction losses in the CsI counter.

To enhance the *n–d* elastic cluster, generous cuts were applied to neutron angle and neutron time of flight spectra, figures 4-18 and 4-19, during *pass 1*. The quantities plotted in these histograms, $\Delta\mathrm{TOF}_n$ and $\Delta\theta_n$, are differences of the actual measured values and the expected values for *n–d* elastic scattering. Therefore we anticipate a peak near zero in both plots to correspond to the real *n–d* events. These initial cuts were deliberately set extra wide so as to eliminate the possibility of excluding any of the interesting events. The neutron angle cut was applied first. The histogram of $\Delta\theta_n$, dominated by *n–p* scattering events, shows only a hint of what might be an *n–d* peak near zero. Since the events in the $\Delta\mathrm{TOF}_n$ histogram have been filtered through the $\Delta\theta_n$ cut, albeit a wide one, the *n–d* elastic peak is a prominent feature in the $\Delta\mathrm{TOF}_n$ histogram. Finally, a new E vs ΔE plot is assembled from the events that pass both neutron angle and neutron time of flight kinematic cuts. Figure 4-20 shows the new histogram with the deuteron cluster clearly identifiable. The placement of a graphical cut around the deuterons, made unambiguous by the preceding analysis, completes *pass 1*.

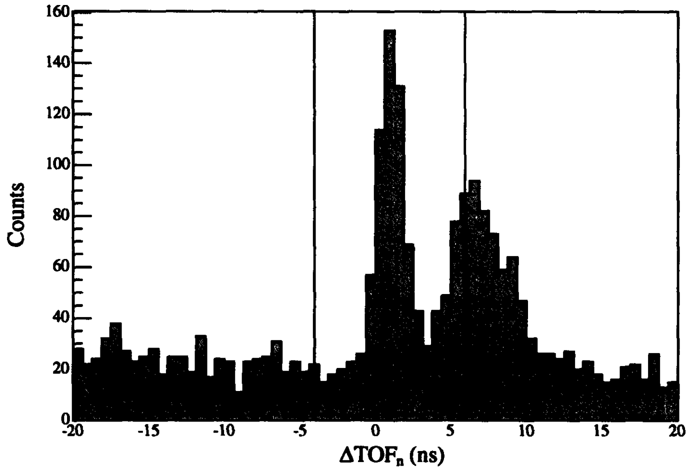

Figure 4-19: A difference of measured and expected neutron times of flight, ΔTOF_n, is plotted for neutrons conjugate to 36° telescope. The generous cut of *pass 1* is shown by red lines. A still appreciable number of the quasielastic protons form the peak on the right.

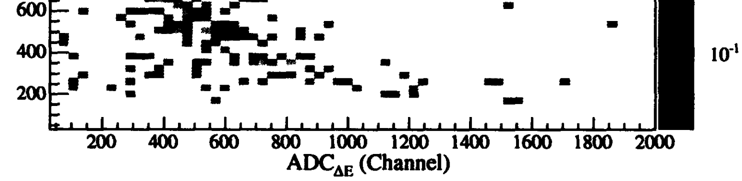

Figure 4-20: E vs ΔE for 200 MeV events in 36° telescope after neutron kinematic cuts. The strong *n–p* elastic locus has been removed by the cuts; only a trace of inelastic background events remain in addition to a well-isolated *n–d* elastic cluster.

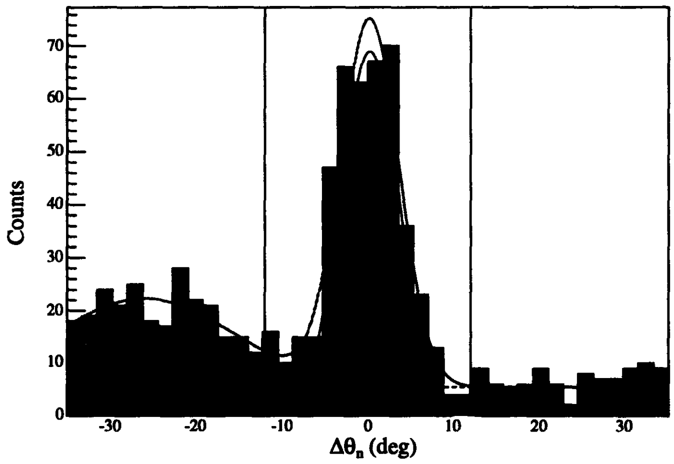

Figure 4-21: A difference of measured and expected neutron scattering angles, $\Delta\theta_n$, is plotted for neutrons conjugate to 36° telescope. A tighter cut of *pass 2* is shown by red lines.

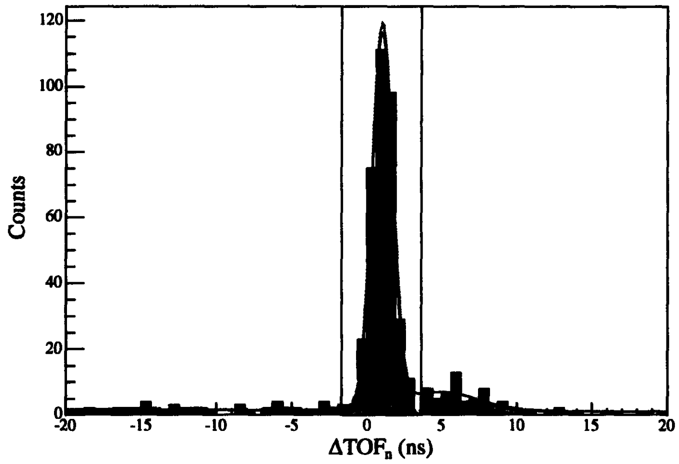

Figure 4-22: A difference of measured and expected neutron times of flight, ΔTOF_n, is plotted for neutrons conjugate to 36° telescope. A tighter cut of *pass 2* is shown by the red lines. This plot also gives an idea of the accidental coincidence background amplitude. The spectrum was fitted with a function (green) which is a sum of linear accidental background (black), Gaussian quasielastic contamination (yellow) and a Gaussian signal peak (blue).

During the next stage, *pass 2*, we partly reverse the order of the cuts. The first cut to be applied is the freshly set two-dimensional cut on E vs ΔE histogram. Coincident events which satisfy this condition make up the new plot of neutron scattering angles. Figure 4-21 shows an example of the $\Delta\theta_n$ plot for neutrons conjugate to 36° telescope. At this point, the number of background events is significantly reduced from that found in figure 4-18, and the *n–d* elastic peak is clearly seen. The bounds of a new, stricter $\Delta\theta_n$ cut, are established based on the analysis of the shape of the peak and background distribution. We fitted the spectrum with a sum of a second-degree polynomial background and a Gaussian signal function. The cut was then set using the bounds of the signal Gaussian distribution as guidelines.

Events that made it through the new angle cut are shown in figure 4-22. The ΔTOF$_n$ cut deserves a special attention as it is the last condition applied to the data before the evaluation of the cross section. As was done with the $\Delta\theta_n$ histogram, the spectrum shown in the figure was also fitted with a sum of a linear background, a Gaussian quasielastic contamination peak, and a Gaussian signal peak. The bounds of the Gaussian signal peak helped define the limits of the cut. The linear function gives an estimate of the number of accidental coincidence events, which is quite small in this case.

This marks the end of the *pass 2*. During the next pass, *pass 3*, the cuts remained unchanged while we replayed the data. The number of coincidence events which passed all three cuts was then used to compute *n–d* elastic differential scattering cross section. Figure 4-23 shows our results for $T_{beam} = 200 \pm 5$ MeV. Also plotted are the results of several previous measurements of Nd systems and the theoretical predictions for the cross section with and without three nucleon forces by Witala et al., [5].

Having completed the evaluation of the *n–d* elastic differential scattering cross section at 200 MeV we repeated this process for $T_{beam} = 95$ MeV and 135 MeV. The results of these analyses are presented in Chapter 6.

4.6 Quasielastic *n–p* Scattering

Having a relatively large cross section, the quasielastic *n–p* process offers additional systematic cross checks of our apparatus and measuring techniques. In this section we estimate the nucleon separation energy E_s and extract the quasielastic *n–p* scattering cross section, to be compared with accepted values.

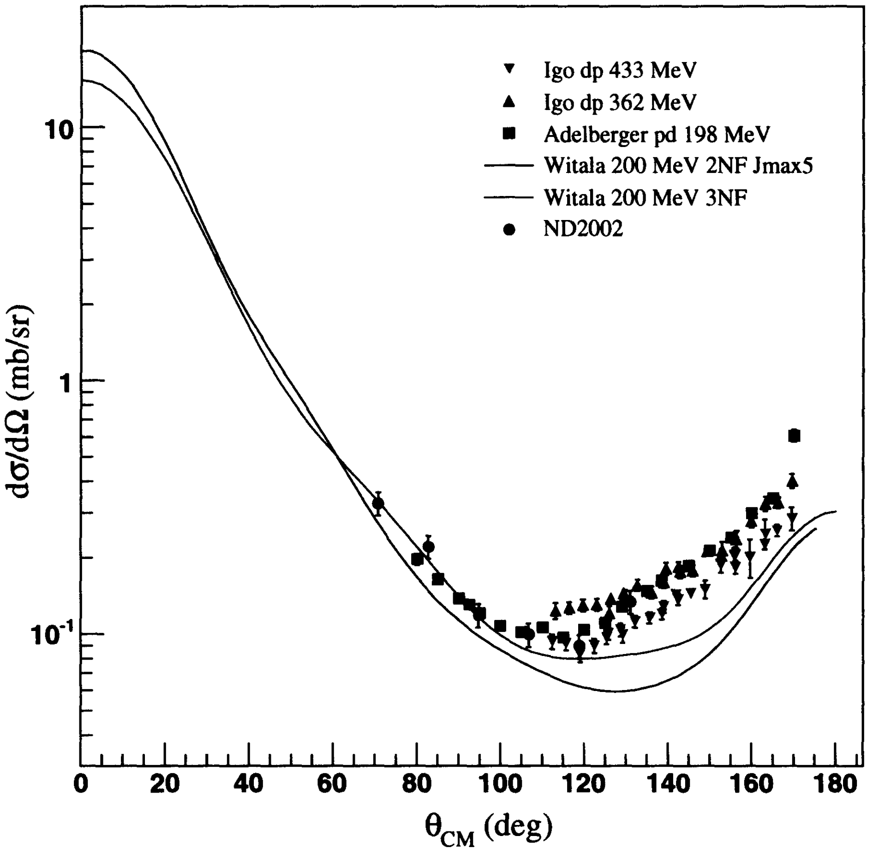

Figure 4-23: The differential Nd cross section at E_N^{lab} = 200 MeV.

4.6.1 Nucleon Separation Energy

The nucleon separation energy E_s – the energy needed to remove a proton or a neutron from the deuterium nucleus – is 2.224 MeV. It can be easily defined in terms of our experimental observables, as in the following equation:

$$E_s = T_{beam} - T_p - T_n - T_{residual}. \tag{4.14}$$

The kinetic energies of the recoil proton, T_p, and scattered neutron, T_n, are measured directly using time of flight techniques, while the determination of the kinetic energies of incident neutron, T_{beam}, and that of residual nucleus – residual neutron in case of a deuterium target – $T_{residual}$, requires additional considerations.

Due to the presence of a third body in the final state of this interaction, the total time of flight of the recoil proton, TOF_p, alone no longer yields T_{beam}, as it did during the true elastic *n–p* and *n–d* measurements of sections 4.4 and 4.5. In order to determine the incident neutron kinetic energy unambiguously, one must also consider the CsI pulse height information. Using the results of the Monte Carlo simulation, discussed in section 5.1, it is then possible to map CsI ADC channel number to TOF_{rec}, a time required by the recoil proton to go from the interaction vertex to the ΔE detector.[3] The difference of TOF_p and TOF_{rec} yields the time taken by the incident neutron to traverse a distance of 1693 (cm) from the neutron production target to the interaction vertex inside the liquid deuterium target. This quantity maps directly into T_{beam} via standard relativistic kinematic equations. Having found T_{beam}, T_p, T_n, it becomes a straightforward matter to determine $T_{residual}$ by using conservation laws for energy and linear momentum.

We begin the analysis of experimental target-full data by selecting coincidence events. An additional software requirement that only a single neutron bar and a single CsI detector had fired reduces the probability of accidental coincidences. This requirement introduces some inefficiency by rejecting true coincidences enhanced with extra proton or neutron detector fires. When extracting the quasielastic *n–p* cross section we shall take special care to account for this effect. However, the only consequence of this inefficiency in the measurement of the nucleon separation energy is a small reduction in the total number of processed events, and therefore it can be safely ignored. A cut on T_{beam}, which is also applied at this point, limits the range of incident neutron energies to 200 ± 5 MeV.

---

[3] A thin plastic scintillator, known as ΔE, placed immediately in front of the CsI detector, provides much sharper timing signals than does the CsI crystal, and hence was used in the analysis for timing purposes instead of the associated CsI detector.

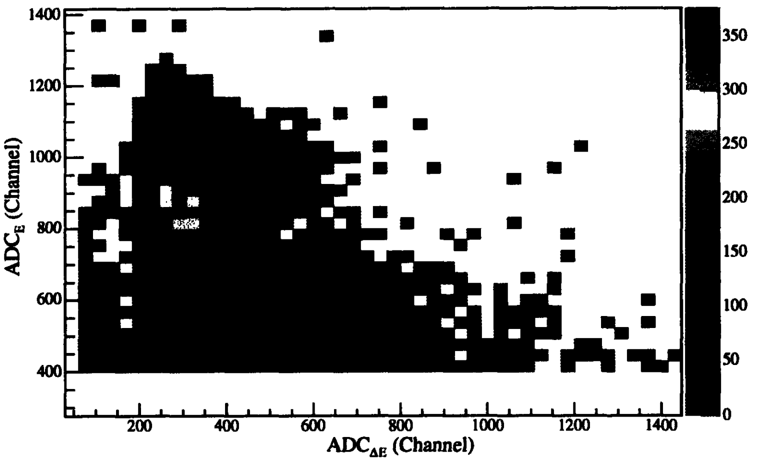

Figure 4-24: Locus of Quasielastic *n*–*p* events at 200 MeV incident beam energy.

Figure 4-24 shows a plot of CsI ADC vs ΔE ADC for events that have satisfied all of the above conditions. As before, the primary purpose of this histogram is to identify various particles and scattering processes. A two-dimensional cut is drawn to select the locus of quasielastic *n*–*p* events.

The quasielastic *n*–*p* events so identified can now be subjected to a series of kinematic cuts to further isolate them from background. The remaining kinematic variables are the mean time of flight of the scattered neutron, TOF_n, and the neutron angle with respect to the incident beam direction, θ_n. Figure 4-25 shows the neutron time of flight cut. A one-dimensional cut, depicted here by two red lines, rejects all events to the left and right of the quasielastic peak. Finally, we restrict the angle of the scattered neutrons, θ_n, by placing another one-dimensional cut to eliminate events outside $\theta_n = 50 \pm 5$ degrees, as in figure 4-26.

Events which pass both the neutron time of flight and the neutron angle cuts are cleared as 'good' quasielastic *n*–*p* events. Figures 4-27, 4-28, and 4-29 summarize kinetic energies of all particles in the final state of the interaction. As anticipated, the chosen geometry (θ_p, θ_n) of (36°, 50°) allows only for a few MeV of residual neutron kinetic energy.

We now have determined all the relevant quantities specified by equation (4.14), and can evaluate E_s. The spectrum of computed nucleon separation energy in figure 4-30 was fitted with a Gaussian function to yield the mean and sigma for the distribution. The mean value

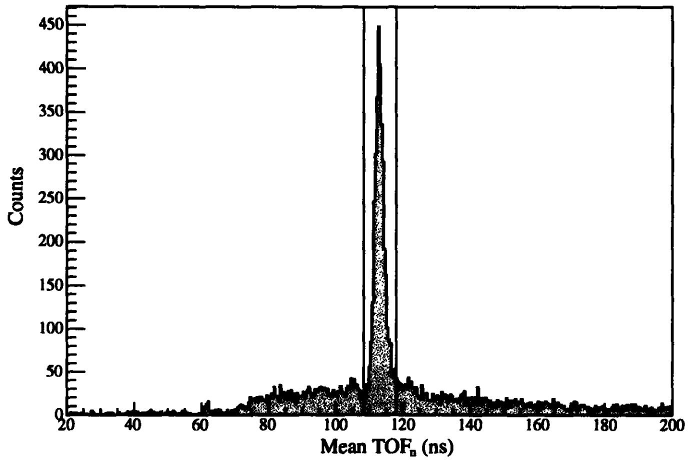

Figure 4-25: Scattered neutron mean time of flight.

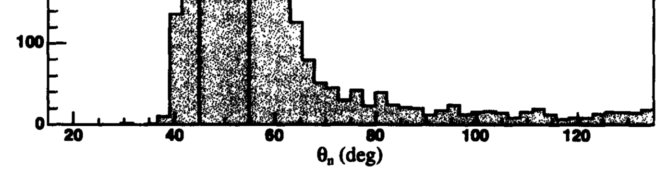

Figure 4-26: Scattered neutron angle.

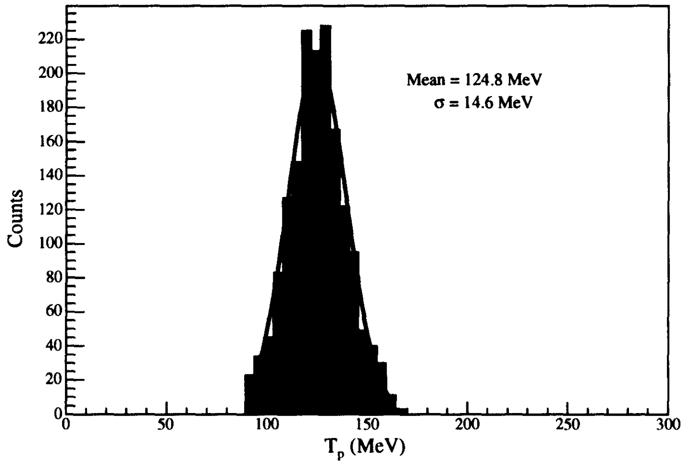

Figure 4-27: Kinetic energy of recoil protons.

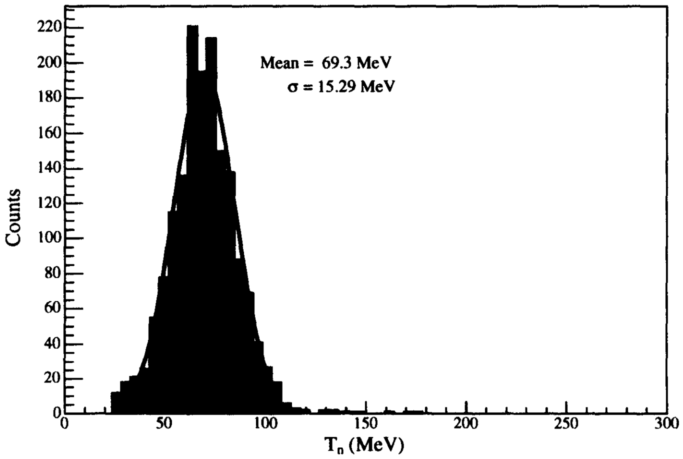

Figure 4-28: Kinetic energy of scattered neutrons.

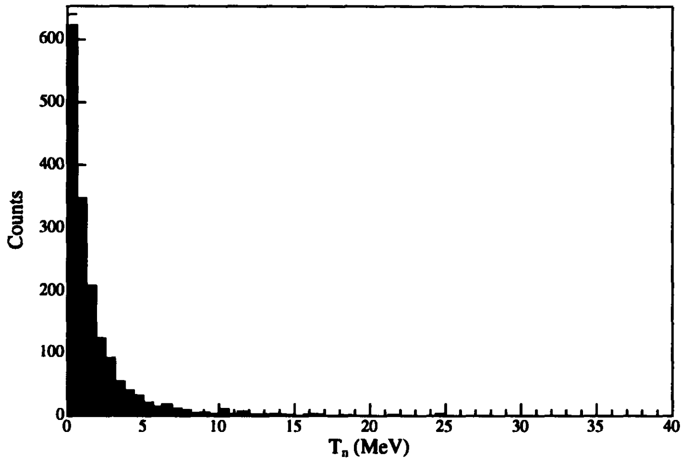

Figure 4-29: Kinetic energy of residual neutrons.

of 3.67 MeV with error of 0.37 MeV disagrees with the correct value of 2.224 MeV. Several limitations of the experimental setup may have resulted in an inaccuracy in this measurement. Among them are the finite sizes of the interaction region and detectors, proton energy loss and the experiments' acute sensitivity to small variations in the time and energy calibration constants. The poor energy resolution of both the proton and neutron arms, attributed to the short times of flight needed for relatively fast particles to cross short flight paths, revealed itself in the width of the E_s distribution.

4.6.2 Quasielastic *n–p* Scattering Cross Section

In addition to the nucleon separation energy, the quasielastic *n–p* scattering cross section was extracted from the *n–d* data. The quasielastic *n–p* process is fairly well understood and so could be easily modeled using Monte Carlo techniques. Section 5.4 describes the details of such a simulation. The ability to predict the shape of the cross section energy distribution along with the fact that the experimental determination of the quasielastic *n–p* cross section can be carried out concurrently with the measurement of the elastic *n–d* cross section makes this a highly desirable check of various systematics. For instance, target thickness can be monitored on a nearly run–by–run basis. The actual minimum acquisition time required for such monitoring is dictated by statistics.

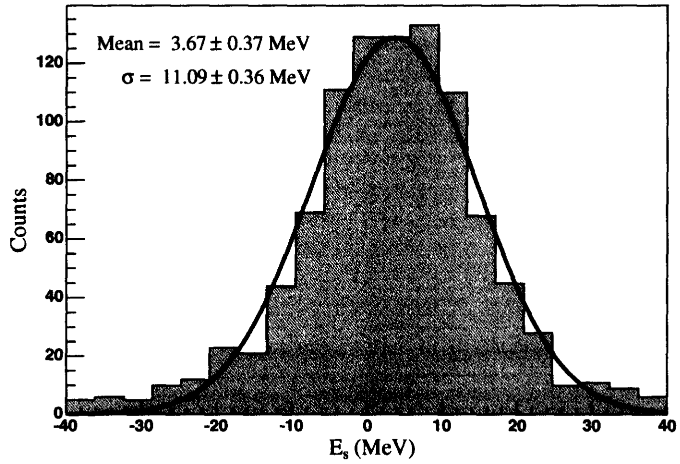

Figure 4-30: Measured nucleon separation energy, E_s.

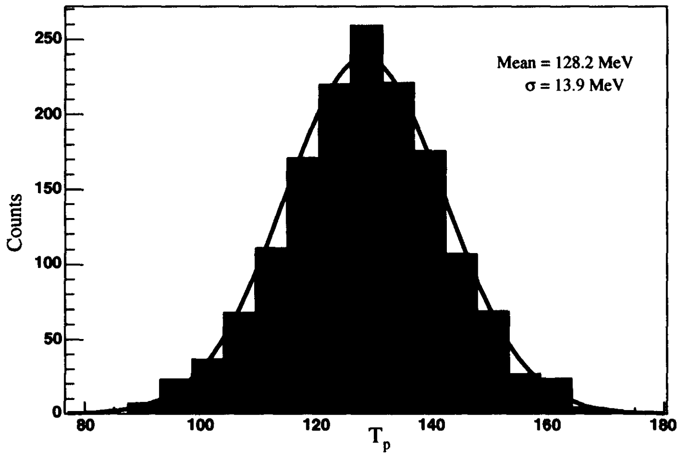

Figure 4-31: Recoil proton kinetic energy.

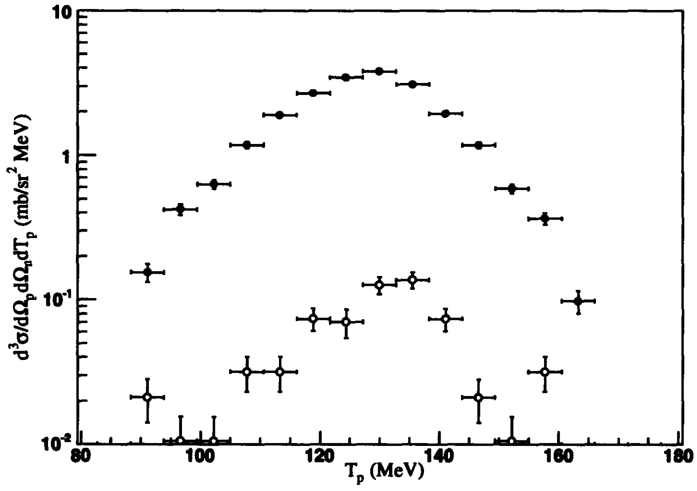

Figure 4-32: Triple differential quasielastic n–p cross section for (36°, 55°) pair at 200 MeV. Normalized empty target background (open circles) is shown together with the full target cross section (filled circles).

The overall flow of the analysis closely resembled that of section 4.6.1. All coincidence events were initially selected according to the value of their trigger bit. The restriction that only a single pair of detectors must have formed the coincidence was removed to eliminate possible associated inefficiency. The role of selecting true coincidences among multi-fire events fell on the kinematic cuts. All coincidence events were then subjected to a similar series of cuts. As before, a cut on the incident neutron kinetic energy restricted the range of beam energies to 200 ± 5 MeV. In addition, software thresholds were applied to the neutron bars via a cut on the geometric mean of ADC channel for left and right photo-tubes of each bar. This cut eliminated events which deposited less then 4 MeVee in a neutron detector and so enabled the determination of neutron detector efficiencies (see section 4.2.2). The ΔE-E, the neutron mean TOF cuts (figures 4-24 and 4-25) and the neutron scattering angle cut remained unchanged. The coincidence events which passed all of the above cuts comprised the histogram of recoil proton kinetic energy in figure 4-31.

Once all cuts were in place, we analyzed both full and empty target runs and extracted the experimental triple differential scattering cross section for each case. These are plotted as a function of recoil proton kinetic energy in figure 4-32; the solid circles represent full target cross section, while the open circles mark cross section measured with an empty target. Comparing

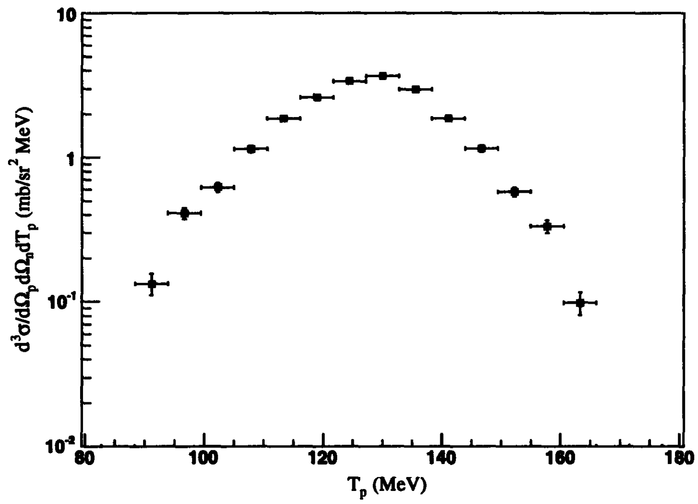

Figure 4-33: Triple differential quasielastic *n*–*p* cross section for $(\theta_p, \theta_n) = (36°, 55°)$ at 200 MeV. Normalized empty target background has been subtracted from the full target cross section.

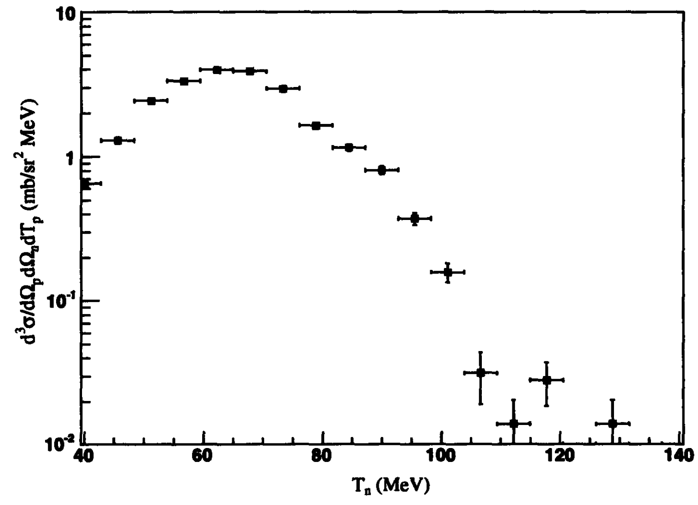

Figure 4-34: Triple differential quasielastic *n*–*p* cross section for $(\theta_p, \theta_n) = (36°, 55°)$ at 200 MeV. Normalized empty target background has been subtracted from the full target cross section.

full and empty target cross sections in this way allows for implicit normalization of runs to fission chamber yields, electronic live time, etc. Finally, the empty target background cross section was subtracted from the target full signal and the result plotted as a function of recoil proton and scattered neutron kinetic energies in figures 4-33 and 4-34.

4.7 Backgrounds

There are two main sources of background events which are common among the *n–p* elastic, *n–p* quasielastic, and *n–d* elastic measurements. They are the empty target and the accidental coincidences. The *n–d* elastic cross section may also be contaminated by a small number of quasielastic protons which result from a deuteron breakup inside the liquid deuterium target. The contributions of these background sources must be estimated and subtracted from the final results.

4.7.1 Empty Target Background

The events which are produced in secondary reactions outside of the liquid deuterium target are referred to as the empty target background events. They are mostly due to the (n, np) reactions in the target flask windows. Naturally, the number of such events is proportional to the incident neutron flux and does not depend on the presence or absence of liquid deuterium in the target flask. Hence, correcting the final results is simple: we must analyze the empty-target runs in exactly the same way as the full-target runs and subtract the resulting cross section. To ensure proper scaling of the empty target background prior to the subtraction, we normalized the number of the background events to the number of incident neutrons in full target runs. The neutron yield information is supplied for the full and empty target runs by the fission chamber. The following equation defines the scaling of the empty target data:

$$\frac{d\sigma_{norm}}{d\Omega} = \frac{N_{full}}{N_{empty}} \cdot \frac{d\sigma_{empty}}{d\Omega}, \tag{4.15}$$

where N_{full} and N_{empty} are the total neutron yields for full and empty target runs, $d\sigma_{empty}/d\Omega$ is the empty target cross section, and $d\sigma_{norm}/d\Omega$ is the normalized empty target cross section to be subtracted from the full target data.

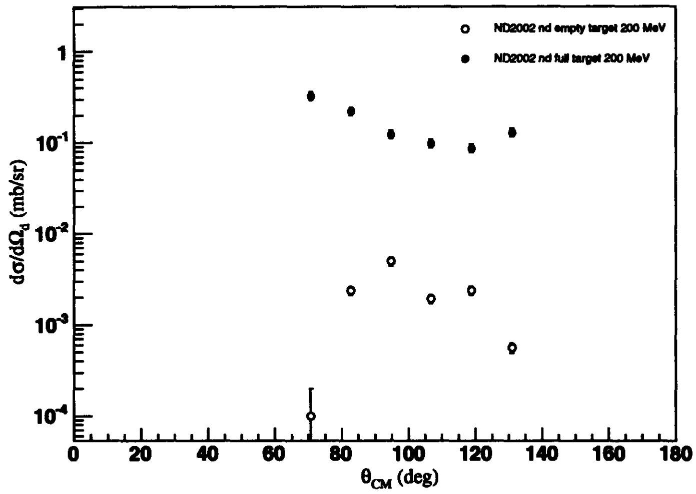

Figure 4-35: Differential elastic *n–d* cross section at 200 MeV. Normalized empty target background (open circles) is shown together with the full target cross section (filled circles).

Figure 4-32 shows both full and empty target cross sections for the quasielastic *n–p* pair at 200 MeV. The empty target background cross section is one order of magnitude smaller than that of the true quasielastic *n–p* scattering.

Figure 4-35 shows a comparison of magnitudes for full and empty target elastic *n–d* cross section. The full target data is two orders of magnitude larger than the empty target data. Such low background is a result of the rigorous kinematic constraints applied to the data to select *n–d* events.

4.7.2 Accidental Coincidence Background

Another source of background is accidental coincidences. These are uncorrelated events which generate a legitimate coincidence trigger by mimicking the appropriate timing behavior in the neutron and charged particle arms of the apparatus. We aimed to minimize the number of accepted accidentals by establishing tight coincidence timing windows in the electronics and by applying a series of strict kinematic cuts to the data. Figure 4-22 gives an idea of the magnitude of the accidental coincidence background. This is a plot of the last in the series of kinematic conditions applied to the *n–d* elastic data. All events which appear between the red markers are accepted as good *n–d* coincidences. As designated by the black dashed line, about 1-2% of the accepted events is due to the accidentals.

Chapter 5

Monte Carlo Simulation

A need for a comprehensive Monte Carlo simulation arises soon after one realizes that any real-life apparatus with its finite size beam, target and detectors, a host of secondary, often unwanted, processes, and a set of rather stringent detector resolution limitations can yield nothing more than a smeared picture of an otherwise theoretically-crisp, or at least Heisenberg-crisp, world. To help untangle the effects of particle energy loss, timing and energy detector resolutions as well as to optimize the performance of the experimental setup we created a complete Monte Carlo simulation of our experiment, which is the main subject of this chapter.

The inherent flexibility of our Monte Carlo code allowed us to use essentially the same core engine for simulating n–p , quasielastic n–p , and n–d interactions by substituting reaction-specific routines where appropriate. The following is an overview of this common simulation environment.

The flow of the Monte Carlo simulation closely resembles the sequence of events during the actual experiment. The data are processed one event at time. Each Monte Carlo event begins with event generation. During this stage two things are set at random: the kinetic energy of a beam neutron and the location of the interaction vertex inside the target volume. The kinetic energy of the incident neutron is selected from a specified range of possible energies, e.g. 5.0 – 800.0 MeV, while the probability of having such a beam neutron is reflected in the corresponding weighting factor. The weighting factor itself is computed in advance using the energy distribution of the incident neutron flux and the beam intensity profile, registered on a photographic plate during the actual experiment, see figure 2-3. Next, the coordinates of the interaction vertex are selected. Special care is taken to ensure that the selected point belongs to a volume which is defined by the union of the target volume and the cylindrical volume of all possible incident beam vectors; the latter is defined by the size of the beam collimator employed during the experiment. The interaction vertex and the beam energy define the incident beam four-momentum. The assumption that all beam neutrons travel parallel to the beam axis is implied. The time of flight of the incident neutron of a given kinetic energy across $L_0 = 1693.0$ centimeters constitutes the first tracking parameter written to a log.

The next order of business is to generate the initial four-momentum of a target nucleus. When simulating true n–p or n–d elastic processes, this task is rather trivial, as the target nucleus is assumed to be at rest with respect to the lab frame. In these cases, the four-momentum can be immediately specified as

$$P^{\nu}_{target} = (M_{target}, \vec{0}). \tag{5.1}$$

For quasielastic n–p calculation, however, the four-momentum of the target nucleon is modified to reflect the fact that this bound nucleon possesses some Fermi momentum, $\vec{p}_f$. This formulation, therefore, gives away the very meaning of the quasielastic n–p interaction from the simulation standpoint: a quasielastic n–p event can be simulated by modifying a true n–p event so as to allow the target nucleon to carry a non-zero momentum in the lab frame. The probability distribution of such momentum must be known in advance and, in our case, must reflect the momentum distribution of a constituent proton inside a deuterium nucleus.

One such distribution is shown in figure 5-1. Equation 5.2 gives a more general form of the target nucleus four-momentum.

$$P^{\nu}_{target} = (\sqrt{M^2_{target} + \vec{p}_f \cdot \vec{p}_f}, \vec{p}_f). \tag{5.2}$$

One other distinction between simulating true and quasielastic n–p events concerns the recoil particle energy loss. Here we must only note that during n–p elastic runs the target is filled with liquid hydrogen, while it contains liquid deuterium during the quasielastic n–p measurement. The amount of energy lost by a recoil proton in hydrogen will differ from that lost by the same proton in deuterium. The rest of the experimental apparatus is unchanged between these two measurements and, hence, the rest of the simulation is identical in both cases.

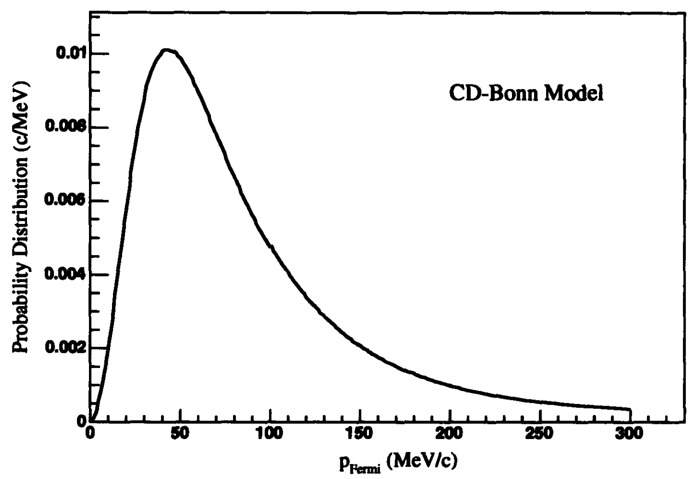

Figure 5-1: CD-Bonn Nucleon Momentum Distribution, [16].

This marks the end of the event generation stage. It is convenient to describe the interaction itself in the center-of-mass frame of the interacting particles and then switch back to the lab frame for the tracking of any outgoing particles.[1] The advantage is two-fold. While in the center-of-mass frame, the direction of the momentum vector of an outgoing charged particle can be randomly selected from a spherically symmetric distribution, and its magnitude from a uniform distribution of, say, 1 to 300 MeV/c, as in [16]. At the same time, the momentum vector of the scattered neutron must obey relation (5.3) to conserve linear momentum. In addition, the center-of-mass formulation simplifies modeling of realistic scattering probabilities as the *n*–*p* elastic scattering cross sections are readily available from SAID database [17] and can be used directly to set appropriate weighting factors for each event.

$$\vec{p}_{scat} = -\vec{p}_{recoil} \tag{5.3}$$

Once the four-momenta of both outgoing particles are determined and the weighting factors are assigned to the event, we transform all momentum four-vectors back to the lab frame. To speed up the simulation, we process only those events which would cause a legitimate trigger

---

[1] The four-momentum description of the system makes such transformations especially straightforward: all conversions are accomplished via simple Lorentz boosts.

during an experimental run, i.e. events in which trajectories of particles with non-zero final kinetic energies terminate in appropriate detectors. All other events are discarded. In the following sections we give detailed descriptions of the event processing that takes place.

5.1 Particle Energy Loss Estimation

The recoil particle energy loss, which occurs during a passage of charged particles through various media, such as the cryogenic target itself, target windows, tape, plastic scintillators and even air, is a significant factor that needs to be known well for proper cross section determination. In cases of elastic scattering, e.g. elastic *n–p* and *n–d* , the recoil proton energy loss, if not taken into account, would cause an underestimation of the incident neutron kinetic energy at the interaction vertex as well as that of scattered neutron and recoil proton, while also introducing an error in the predicted scattered neutron angle. For the case of quasielastic *n–p* scattering the effect of proton energy loss on kinematic variables is similar in essence, although the actual calculation is further obscured by the necessity to use proton pulse height information in order to unambiguously define the three body final state of this interaction.

Therefore, our first order of business is to estimate the amount of energy a recoil particle of given initial kinetic energy, either a proton or a deuteron, would lose during its voyage to a proton telescope, and to do this for various experimental configurations. The three cases of interest are:

- *n–p* elastic – proton through liquid hydrogen target and rest of the apparatus,
- *n–p* quasielastic – proton through liquid deuterium target and rest of the apparatus,
- *n–d* elastic – deuteron through liquid deuterium target and rest of the apparatus.

5.1.1 Proton and Deuteron Range Tables

The implementation of the energy loss calculation of section 5.1.2 relies on particle range tables to estimate the amount of energy deposited in each traversed medium. Proton tables for most materials comprising the experimental apparatus are available from NIST PSTAR database [18]. Still, tables for several desirable combinations (incident particle – material) are not included

Symbol	Definition	Units or Value
M	Incident particle mass	MeV/c^2
E	Incident particle energy γMc^2	MeV
T	Kinetic energy	MeV
m_ec^2	Electron mass × c^2	0.510 999 06(15) MeV
r_e	Classical electron radius $e^2/4\pi\epsilon_0 m_ec^2$	2.817 940 92(38) fm
N_A	Avogadro's number	6.022 136 7(36) × 10^{23} mol^{-1}
ze	Charge of incident particle	
Z	Atomic number of medium	
A	Atomic mass of medium	g mol^{-1}
K/A	$4\pi N_A r_e^2 m_ec^2/A$	0.307 075 MeV g^{-1}cm^2 for $A = 1$ g mol^{-1}
I	Mean excitation energy	eV
δ	Density effect correction to ionization energy loss	

Table 5.1: Summary of variables used in this section. The kinematic variables β and γ have their usual meanings. See [19] for a complete treatment of passage of particles through matter.

in the database. An example of a missing combination is a proton in liquid deuterium. In addition, deuteron tables are not available for any of relevant materials. This section describes methods for generating the missing range tables. Note that by 'range' we really mean a CSDA range, that is, a range computed in the Constant Slowing Down Approximation.

Charged particles of moderate kinetic energies other than electrons lose energy primarily by ionization. The mean rate of energy loss (or stopping power) is given by the Bethe-Bloch equation,

$$-\frac{dE}{dx} = Kz^2\frac{Z}{A}\frac{1}{\beta^2}\left[\frac{1}{2}\ln\frac{2m_ec^2\beta^2\gamma^2T_{max}}{I^2} - \beta^2 - \frac{\delta}{2}\right]. \tag{5.4}$$

Here T_{max} is the maximum kinetic energy which can be imparted to a free electron in a single collision; the rest of the variables are defined in table 5.1. The stopping power is normalized by the density of the propagation medium so that dx has units of mass per unit area, e.g., $g \cdot cm^{-2}$. For a particle with mass M and momentum $M\beta\gamma c$, T_{max} is given by

$$T_{max} = \frac{2m_e c^2 \beta^2 \gamma^2}{1 + 2\gamma m_e/M + (m_e/M)^2}. \tag{5.5}$$

To obtain an expression for the range, i.e. the maximum distance traveled by a charged particle of initial energy E in a given medium, one simply integrates the inverse of stopping power over available energy:

$$R = -\int_E^0 \frac{dx}{dE} d\epsilon. \tag{5.6}$$

The Monte Carlo code first computes dE/dx according to the Bethe-Bloch equation 5.4 and then performs the above integration numerically to obtain the CSDA range. The density effect correction, δ, is sufficiently small for incident protons in our energy range and is omitted from the calculation.

In addition to the energy loss in media which are made up of a single chemical element, such as liquid hydrogen target cell and aluminum foil, it is also necessary to calculate the energy loss in mixtures. A mixture can be thought of as made up of thin layers of pure elements in the right proportion (Bragg additivity). In this case,

$$\frac{dE}{dx} = \sum_j w_j \left.\frac{dE}{dx}\right|_j, \tag{5.7}$$

where, $dE/dx|_j$ is the mean rate of energy loss (in MeV g cm^{-2}) in the j$^{\text{th}}$ element. An abundance of a particular element in a mixture, w_j, is available from the NIST PSTAR database.

To test this calculation, we first generated proton ranges for various elements and mixtures. Figures A-3 and A-2 demonstrate a good agreement between the computed ranges for protons in material made up of pure elements and corresponding ranges available from the NIST PSTAR database. Figures A-1 and A-4 show similarly acceptable agreement for proton ranges in mixtures.

Having so verified the validity of this approach, we extended it to combinations not available from the PSTAR database. Figure 5-6 shows proton and deuteron ranges in deuterium while Appendix A sports a collection of proton and deuteron ranges for all relevant materials.

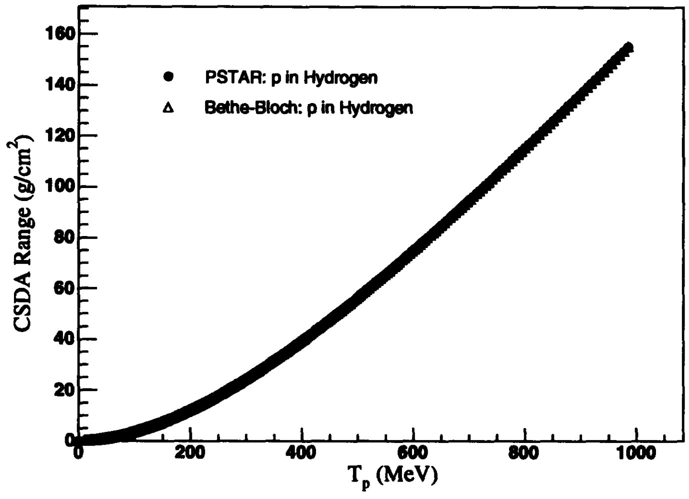

Figure 5-2: Proton CSDA range in liquid hydrogen. Bethe-Bloch calculation for proton range in the lightest of elements is in good agreement with PSTAR database prediction.

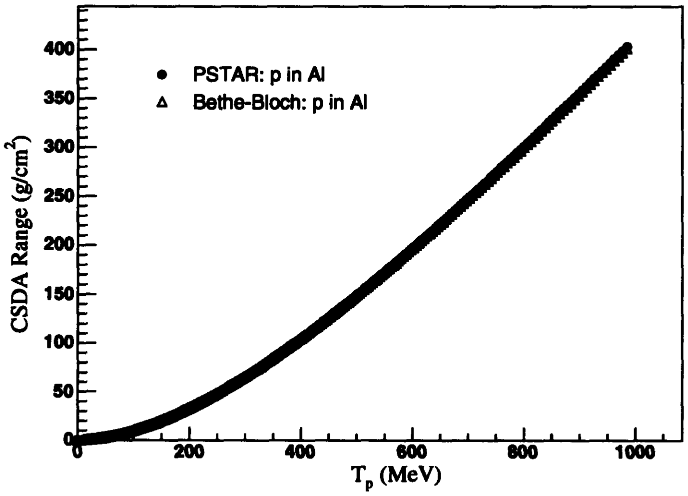

Figure 5-3: Proton CSDA range in aluminum. Bethe-Bloch calculation for proton range in ^{13}Al, one of the heavier elements encountered by recoil protons, is in good agreement with PSTAR database prediction.

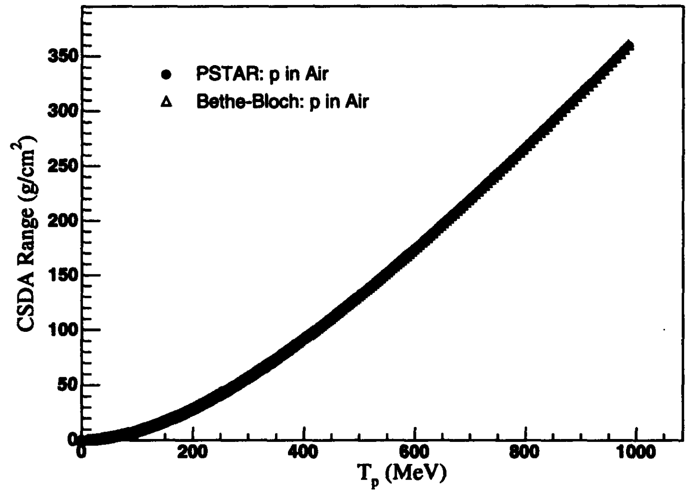

Figure 5-4: Proton CSDA range in air. Bethe-Bloch calculation for proton range in air (mixture composed of 75.52% Nitrogen, 23.17% Oxygen, 1.28% Argon, and 0.01% Carbon) is in good agreement with PSTAR database prediction.

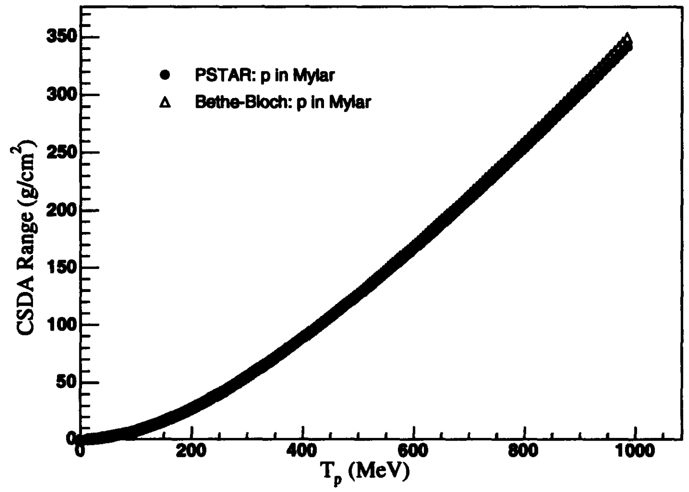

Figure 5-5: Proton CSDA range in mylar. Bethe-Bloch calculation for proton range in mylar (mixture composed of 62.50% Carbon, 33.30% Oxygen, and 4.19% Hydrogen) is in good agreement with PSTAR database prediction, especially for proton energies below 600 MeV.

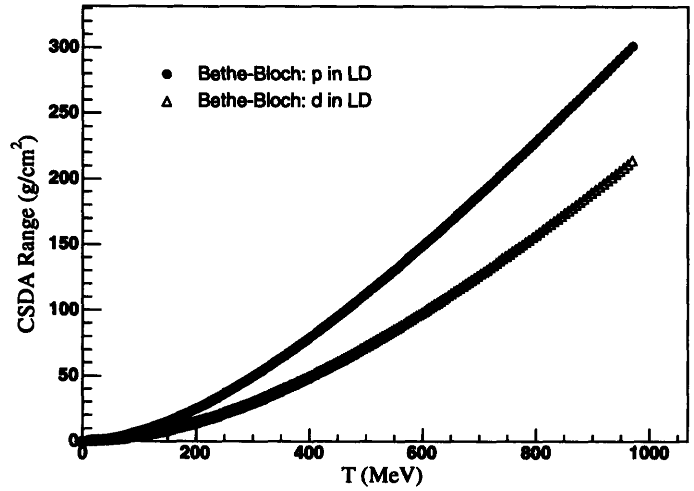

Figure 5-6: CSDA ranges for protons and deuterons in liquid deuterium.

5.1.2 Energy Loss Calculation

We are now ready to proceed with the energy loss calculation. First, consider the problem of energy loss in n–p elastic scattering. Figure 5-7 shows Monte Carlo prediction of the amount of kinetic energy lost by a recoil proton on its way from the interaction vertex to the 24° ΔE.

Let's assume that the event generation stage has alread been completed according to the steps outlined in the beginning of this chapter. The four-momenta of the two outgoing particles at the interaction vertex have been computed and all necessary range tables have been compiled as per instructions of section 5.1.1. We are faced with the task of propagating the charged particle through all materials which separate it from a given ΔE scintillator.

At this point, a quick check of the particle's final destination ensures that it will end up in one of the proton telescopes, else the event is discarded and we begin anew with event generation. Figure 5-8 gives a schematic view of one successful trace with all the relevant materials named.

We begin by recording the initial kinetic energy of the recoil charged particle. This value will be the independent variable in several expressions for energy loss. Next, the exact distances traversed by a charged particle in each medium are computed. Root class *TGeometry* facilitates

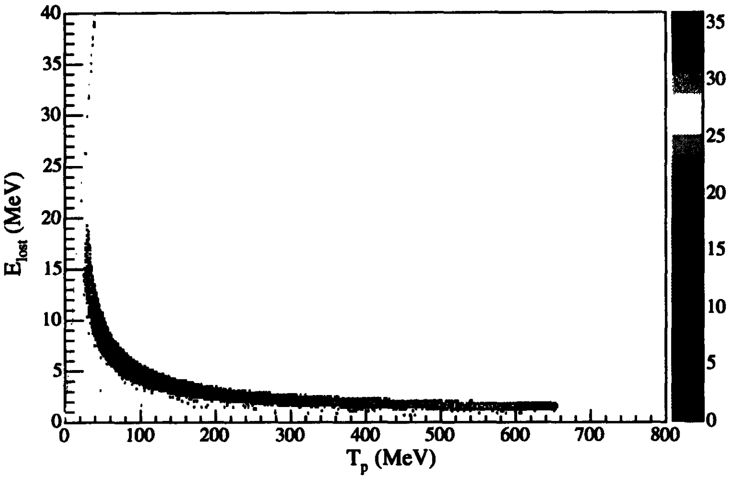

Figure 5-7: Energy loss for protons at 24°. The thickness of the band is due to the uncertainty in the interaction vertex. Thin target cell and small diameter beam both help minimize this uncertainty.

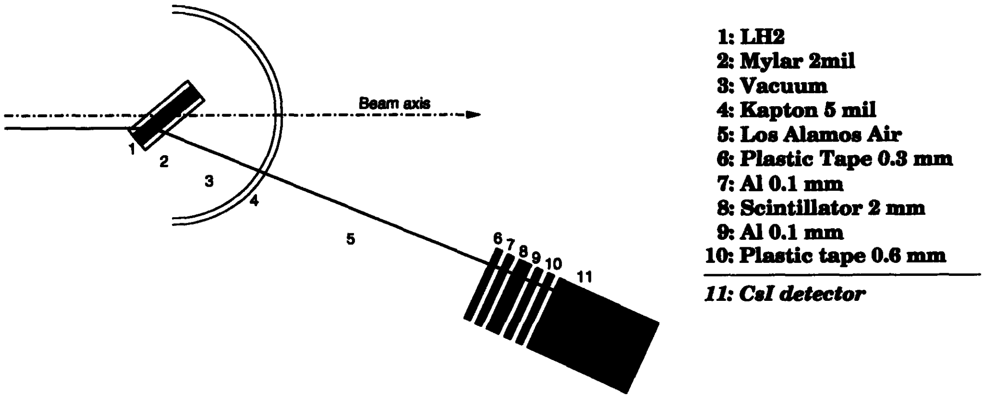

Figure 5-8: Volumes in which recoil charged particles are expected to lose energy.

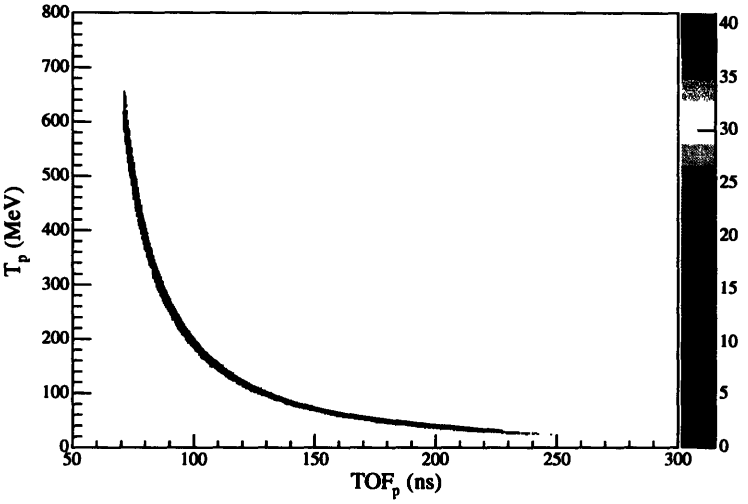

Figure 5-9: Map of total time of flight to initial kinetic energy of recoil proton.

this computation in three-dimensional space. The path of the particle in each medium is broken down into small steps of size *dl*. After each such step, the particle's remaining kinetic energy and its cumulative time of flight are determined using a range table for appropriate material. First, a total range of the particle in this material is computed. Then, the amount of energy required for a range which is *dl* shorter is found using a reverse range table. This method yields a precise value for the final energy. The propagation is completed when the particle reaches the ΔE detector, at which point the particle's final kinetic energy and total time of flight are recorded. Figure 5-9 shows a plot relating total time of flight and initial kinetic energy of the recoil particle. By cutting this two-dimensional histogram into slices parallel to the x-axis and fitting each resultant slice with a Gaussian function, we find the position of the mean, as well as the sigma for each slice's distribution. These facilitate compilation of a map of TOF_p to T_p.

We can use the TOF_p to T_p relation to correct n–p kinematic maps for proton energy loss. As noted earlier, the kinematic maps are used in offline analysis to specify T_p, T_{beam}, T_n, and θ_n, provided the recoil proton total time of flight and its scattering angle are known. All calculations assume elastic n–p kinematics. Since the only effect of proton energy loss on kinematic variables is to extend TOF_p, while keeping all others unchanged, a simple way to apply this correction is to offset the TOF_p column by an appropriate amount with respect to all other columns in the kinematic map files. A comparison of a newly created map to an original,

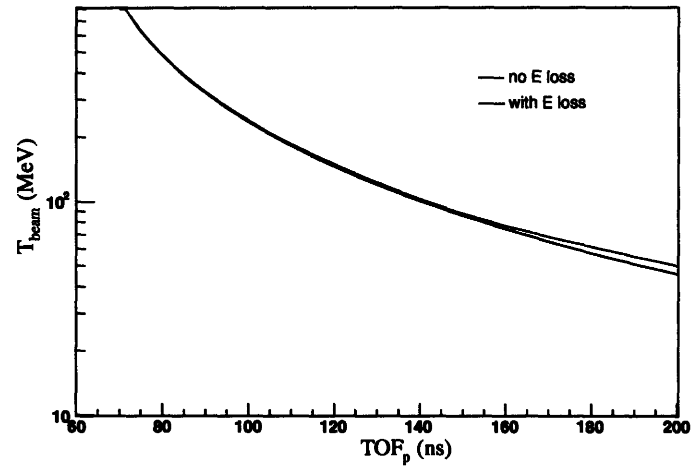

Figure 5-10: Effect of proton energy loss on values of calculated kinematic variables, e.g. T_{beam}, for the 24° telescope. This correction becomes appreciable for lower energy particles.

not corrected, version reveals the discrepancy in figure 5-10. As expected, the correction is especially noticeable for lower energy particles.

The next process of interest is *quasielastic n–p scattering.* As we mentioned earlier, a sole[2] knowledge of the proton total time of flight, TOF_p, is not sufficient to uniquely define the three-body final state of this interaction, as we can no longer assume *n–p* elastic kinematics. To determine the recoil proton kinetic energy at the interaction vertex on an event-by-event basis, we must also use the CsI pulse height information. Therefore, our goal shall be to obtain a map of CsI pulse height to T_p, T_{beam}, T_n, and θ_n. This can be accomplished in two steps. First, use the Monte Carlo simulation to map the proton kinetic energy at the interaction vertex, T_p, to total time of flight, TOF_p. Second, obtain a map between TOF_p and CsI ADC channel number from the analysis of experimental data. Combined, these two maps relate CsI ADC channel number to all other kinematic variables, i.e. T_p, T_{beam}, etc. Technically, in addition to the TOF_p to T_p map one also needs to generate a TOF_{rec} to T_p, where TOF_{rec} is the time it takes a recoil proton to go from the interaction vertex to ΔE detector. This supplementary map, however, is easily generated by our Monte Carlo code. Figure 5-11 shows a plot of this relation for the 36° proton telescope.

---

[2] It is assumed that the recoil proton scattering angle, θ_p, is always known by specifying which telescope caused the event trigger.

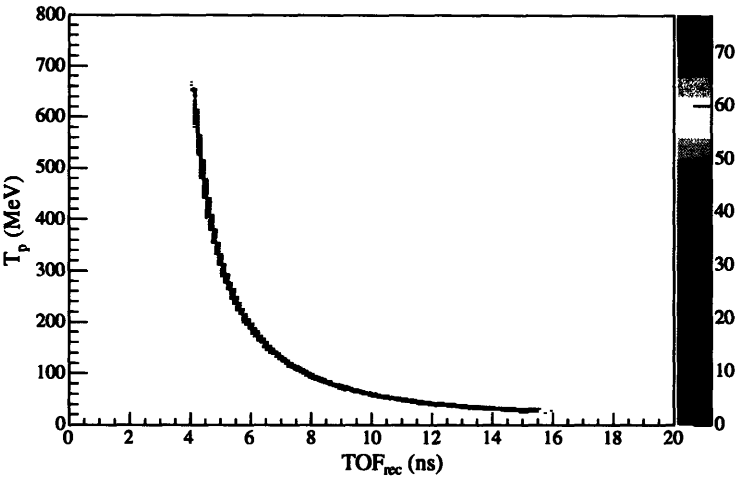

Figure 5-11: A plot of T_p vs TOF_{rec} for quasielastic events at 36°.

The first part of this procedure is identical to the energy loss calculation for *n*–*p* elastic events, with the exception of having to propagate recoil protons through a liquid deuterium target. The result is nearly identical to figure 5-9 and, therefore, is not reproduced here.

In the second part, a replay of experimental *n*–*d* data yields a map of CsI pulse height to total time of flight of a recoil proton, as in figure 5-12. Together, these maps are sufficient to link CsI pulse height to all kinematic variables of interest.

The remaining task is to calculate the amount of energy loss for *n*–*d* elastic scattering. The result is shown in figure 5-13. We are, once again, dealing with a true elastic process, so the general procedure will closely resemble that used in the *n*–*p* energy loss calculation. However, a few things will have to be modified. For instance, deuteron range tables, generated in section 5.1.1, should replace proton range tables, as the recoil particle is now a deuteron, not a proton. Since the cryogenic target contains liquid deuterium, an appropriate range table must be selected to propagate deuteron through the target volume. With all adjustments in place, the Monte Carlo simulation generates a TOF_d to T_d map by slicing and fitting T_d vs TOF_d histograms for each charged particle telescope. Figure 5-14 shows the map superimposed onto one such histogram for the 24° telescope.

We can use the TOF_d to T_d maps to correct *n*–*d* kinematic tables for energy loss. Again, the most straightforward way to apply this correction is to offset the TOF_d column with respect

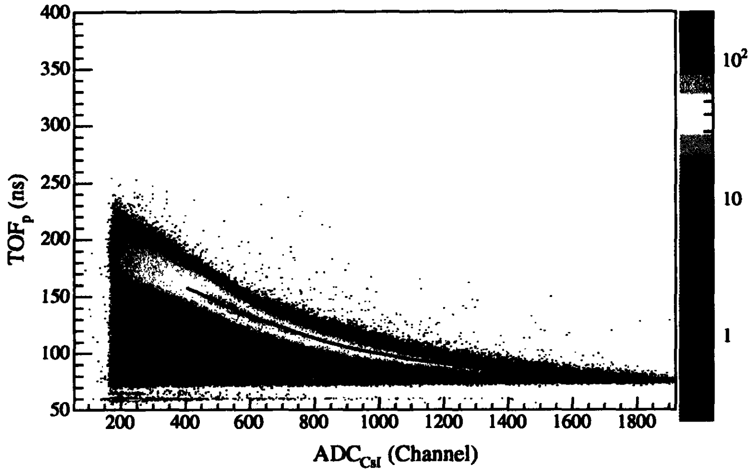

Figure 5-12: Map of CsI pulse height to recoil proton total time of flight. The red curve shows a fit to Gaussian means of individual slices of this histogram along x-axis.

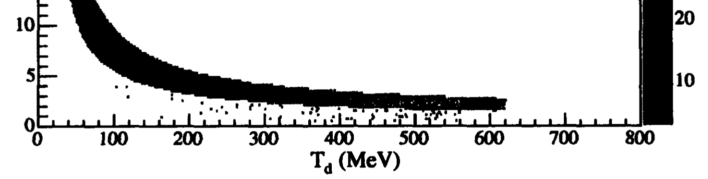

Figure 5-13: Energy loss for deuterons at 24°.

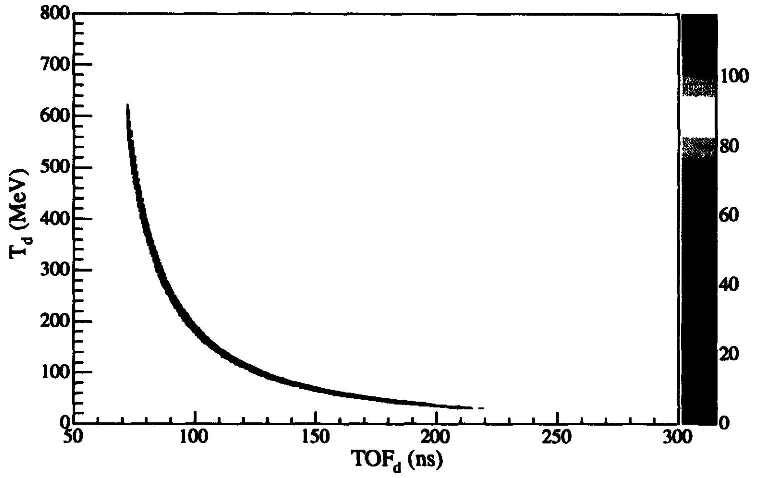

Figure 5-14: Map of total time of flight to initial kinetic energy of recoil deuteron at 24°.

to all dependent kinematic variables in these tables, much like what was done in correcting the *n–p* tables. The length of time by which to offset each entry of the kinematic maps is specified by the TOF_d to T_d maps.

5.2 Target Angle Optimization

It is evident from the above calculations, that most of the energy lost by charged particles is deposited in the cryogenic target. In the effort to minimize the energy loss suffered by recoil particles in the target volume, we wish to optimize the target angle with respect to the incident neutron beam. The target angle shall be called optimal when the average energy lost in the apparatus by deuterons at all detectable recoil angles is minimized. The non-uniform angular distribution of recoil deuterons, see figure 5-15, suggests that such an average should be weighted according to the elastic *n–d* scattering cross section. Also, the optimal target angle depends on the incident neutron energy. We chose to determine the optimum target angle for $\text{T}_{beam} = 200$ MeV, as this energy is the mean of the energy range of interest.

The function to be minimized, then, is $\overline{E}_{lost}(\theta_{target})$, where $\overline{E}$ is the energy lost by deuterons averaged over all detectable deuteron angles and weighted by the angular distribution 5-15.

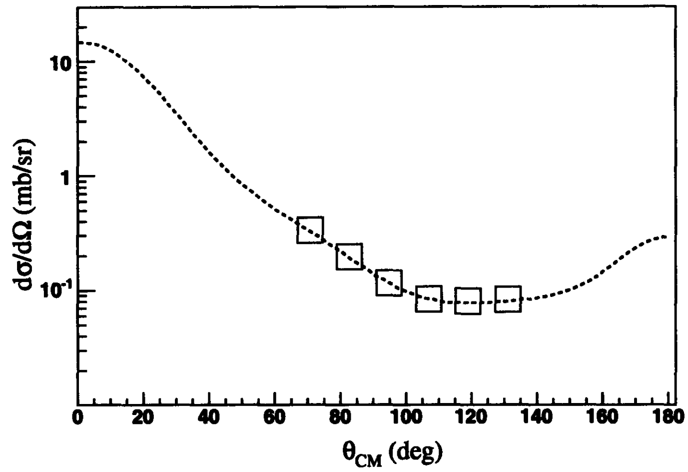

Figure 5-15: Theoretical prediction of the angular distribution of *n–d* elastic scattering cross section at 200 MeV by Witala, et al. [5]. The red boxes mark the locations of proton telescopes.

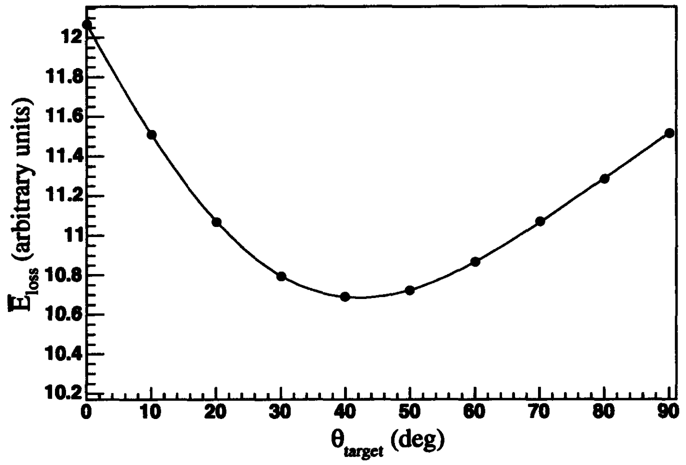

Figure 5-16: Weighted average of deuteron E_{loss} as a function of target angle. The target angle is the angle between a normal to the target plane and the beam direction. $\overline{E}_{loss}$ is shown for $0° < \theta_{target} < 90°$ with respect to the incident beam in increments of 10 degrees. The blue line is a sixth-degree polynomial fit.

We repeat the *n–d* energy loss simulation for various target angles in the range from 0° to 90° with respect to the downstream direction of the incident neutron beam in increments of, say, 10 degrees. For each target angle, the number of hits in each telescope and the total energy lost by these deuterons are recorded. We allow approximately one million events to be distributed over the six charged particle telescopes each time the target angle is changed. To eliminate a possible dependence of our results on the total number of processed events, it is useful to express E_{loss} as amount of energy lost per event per telescope. It is then a straightforward matter to obtain the average energy lost in the apparatus by summing contributions of each telescope scaled with appropriate weighting factors. The resulting quantity, plotted in figure 5-16, is, therefore, independent of the number of processed events and closely reflects the dependence of E_{loss} on target angle:

$$\overline{E}_{loss}(\theta_{target}) = \sum_{\theta_d} w_{cs} \cdot \frac{E_{tot}(\theta_d)}{N_{tot}(\theta_d)}, \tag{5.8}$$

where w_{cs} is the weighting factor based on the *n–d* elastic scattering cross section, N_{tot} is total number of deuterons detected by the telescope at θ_d, and E_{tot} is the total amount of energy lost by these deuterons.

The value of θ_{target} which minimizes energy loss for *n–d* elastic scattering at 200 MeV is roughly 42 degrees. Due to mechanical constraints of the target flask assembly, the value of 50 degrees was used in the experimental setup. The shallow minimum of the energy loss curve in figure 5-16 shows that there is little gain in the amount of energy loss compared to the nominal value at 42 degrees.

5.3 Estimation of Uncertainty in T_{beam}

It is interesting to know what degree of uncertainty in the measured energy of the incident beam, T_{beam}, is due to finite sizes of the beam, cryogenic target and detectors. For elastic scattering the energy of the incident beam neutron is derived via kinematic relations from the total time of flight of the charged particle. Therefore, variations in the energy loss and scattering angle of the charged particle translate directly into uncertainty in the beam energy. Having implemented both the energy loss and the correct geometry of our setup in the Monte Carlo simulation we are in a good position to evaluate this effect.

Figure 5-17 shows a plot of the simulated variation in the beam energy as a function of beam energy for elastic *n–d* scattering into the 36° telescope. On the vertical axis we plot

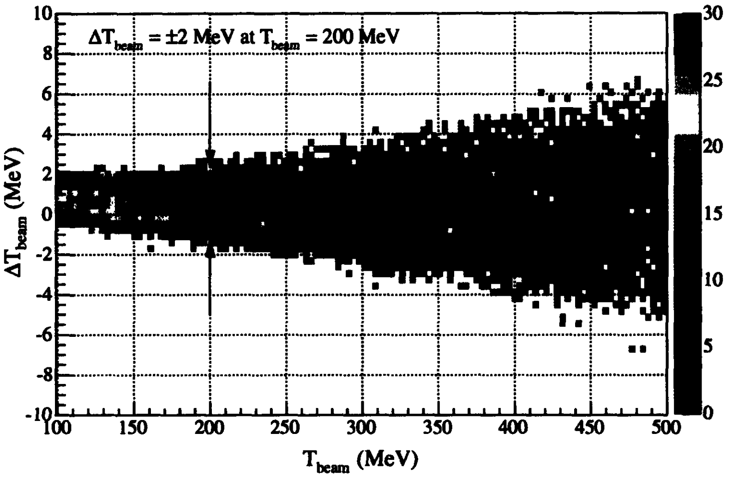

Figure 5-17: Uncertainty in T_{beam}.

the difference of the generated T_{beam} and measured T_{beam}. The measured beam energy was obtained from the deuteron time of flight using the same kinematic map which is used in the offline analysis. The result suggests that an uncertainty in the beam energy of about 1% should be expected for elastic *n–d* scattering at 200 MeV.

5.4 Quasielastic *n–p* Scattering Cross Section

Next, we extend the use of this Monte Carlo simulation to calculate the quasielastic *n–p* scattering cross section. The goal is to be able to generate the triply differential cross section, $\frac{d^3\sigma}{d\Omega_p d\Omega_n T_p}$, as a function of the recoil proton kinetic energy. This allows one to further verify the validity of the Monte Carlo by comparing these results to theoretical predictions for the quasielastic *n–p* scattering cross sections in [20]. A more compelling reason for this calculation, however, is that it enables a robust way of monitoring various systematic parameters of the *n–d* elastic measurement, e.g. target thickness. Quasielastic *n–p* events come as a bi-product of the *n–d* elastic measurement, they are a part of the same *n–d* data set and are subject to the same systematic conditions. Therefore, having a handle on the quasielastic *n–p* cross section corresponds to keeping a concurrent check on the *n–d* elastic measurement.

5.4.1 Simulation Cross Check using *n–p* Elastics

Major parts of the simulation code, such as the event generation and particle propagation, have been already developed for the energy loss calculation of section 5.1. What remains to be implemented is a mechanism which would ensure correct angular and energy distributions of the recoil protons. The approach used in our Monte Carlo included a weighting system, in which each event is assigned a weighting factor. This factor represents an overall probability of occurring for such an event. The factor is comprised of two main parts: beam weight and recoil weight. The former reflects the probability of having an incident neutron of a given four-momentum and is largely determined by the measured beam profile and the energy distribution of the incident neutron flux. The latter contains most of the information on energy and angular distributions of the scattering process at hand. In other words, it is proportional to the magnitude of the scattering cross section. For quasielastic *n–p* scattering, the recoil weight is also a function of the Fermi momentum of the target proton.

Let's start with a special case of the quasielastic *n–p* process, one in which the lab Fermi momentum is set to zero. This, of course, is identical to elastic *n–p* as far as the simulation is concerned, as described in the beginning of this chapter. If a scattering cross section is calculated while this condition is active, the result should be identical to the *n–p* elastic scattering cross section. In this way all of the simulation code, with the exception of the nucleon momentum generation part, can be verified. Figure 5-18 shows simulated *n–p* elastic scattering cross sections for six proton telescopes as a function of beam kinetic energy. The red curve in each plot represents the SAID fit. A good agreement between the simulated cross section and the fit is evident. This fact gives us confidence that the simulated angular and energy distributions are correct.

5.4.2 Comparison with PWIA Calculation

Turning on the Fermi momentum generator yields a simulation of quasielastic *n–p* scattering. Here we used the nucleon momentum distribution of [16], depicted in figure 5-1. First, the three-momentum of a target proton in the lab frame is selected. Its magnitude is chosen from a uniform distribution in the range of 0 to 300 MeV/c, while its direction is selected from a spherically symmetric distribution. The nucleon momentum distribution, then, gives a weight associated with this momentum magnitude. Next, the four-momentum of the target proton in (equation 5.2) is found. This four-vector, together with that of the incident neutron, define

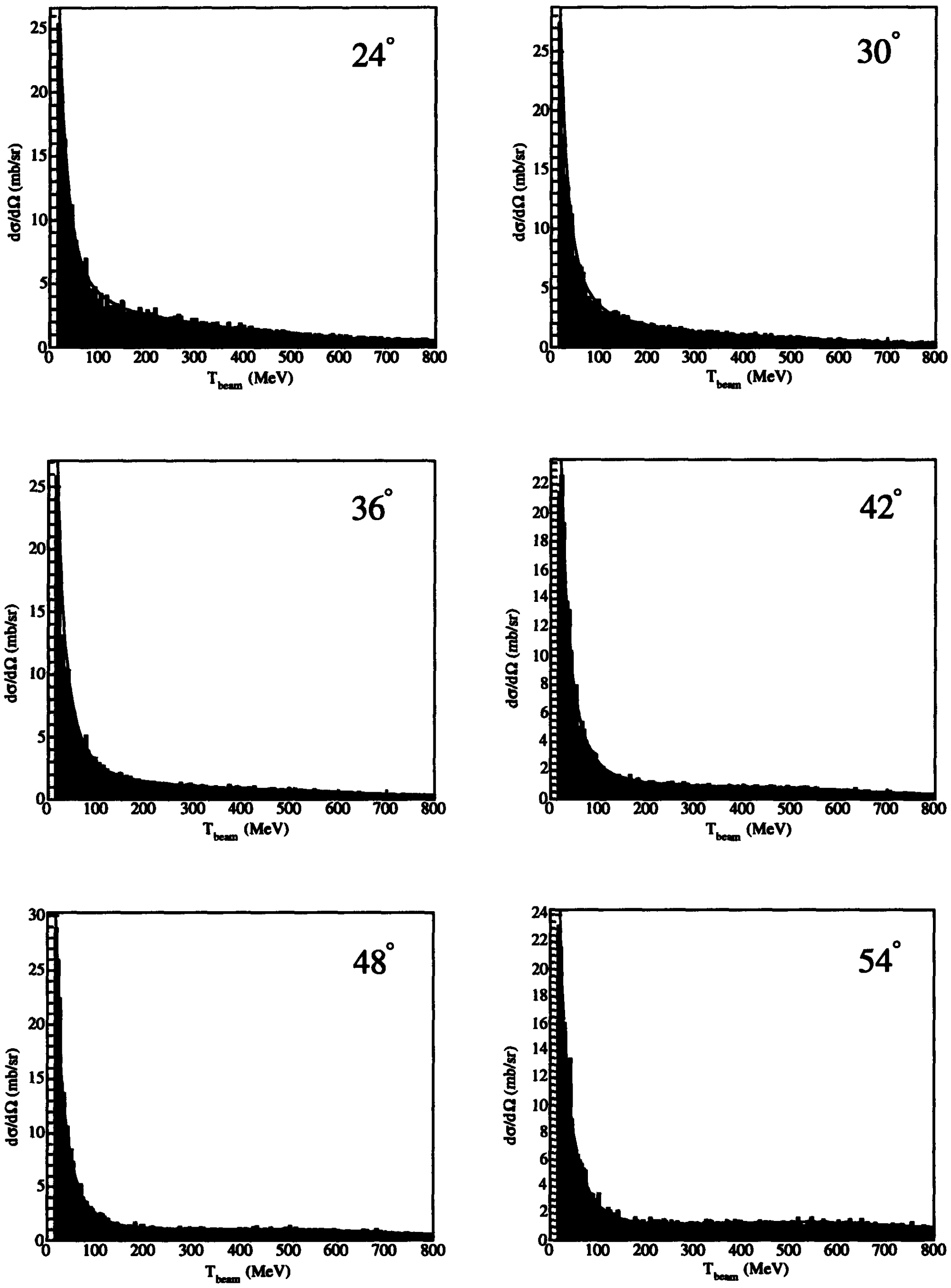

Figure 5-18: Simulated n–p elastic cross section.

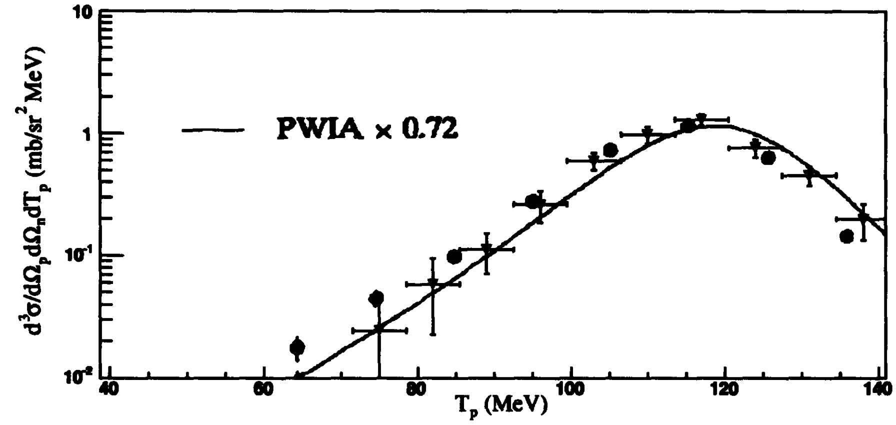

Figure 5-19: Simulated triple differential cross section for quasielastic *n*–*p* at 200 MeV with θ_p=35° and θ_n=45° (blue triangles). Experimental data (black circles) and PWIA curve are from [20]

a boost, needed to transform to the center of mass frame. Once in the center of mass, the direction of the recoil proton is selected from a spherically symmetric distribution, while the weighting factor based on the nucleon momentum distribution is combined with that based on the *n*–*p* elastic scattering cross section for a given angle and beam energy. The rest of the simulation proceeds unchanged from the *n*–*p* case discussed above.

Simulated quasielastic *n*–*p* scattering cross sections were compared to the prediction of plane-wave impulse-approximation (PWIA) for ^{2}H($\vec{p}$,*pn*)^{1}H reaction at 200 MeV, see [20]. Figures 5-19 through 5-22 show the results for (θ_p, θ_n) = (35°, 45°), (45°, 45°), (45°, 35°), (36°, 55°) coincidence pairs. Our simulation is in good agreement with the PWIA calculation and previous experimental data, also plotted in the figures.

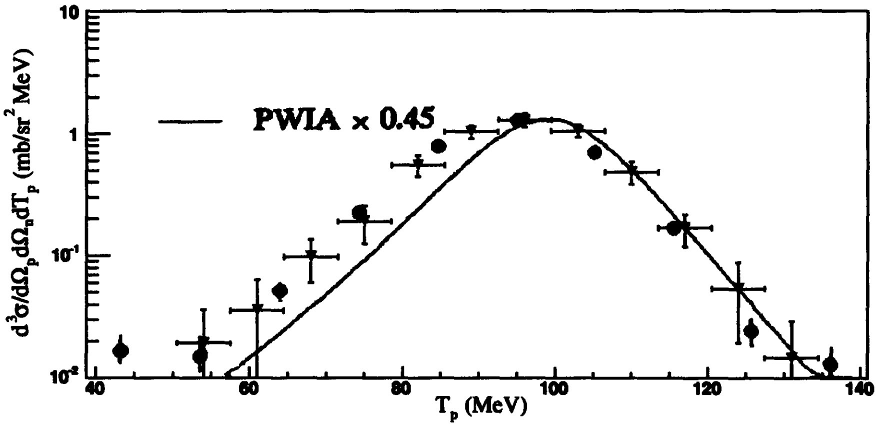

Figure 5-20: Simulated triple differential cross section for quasielastic n–p at 200 MeV with θ_p=45° and θ_n=45° (blue triangles). Experimental data (black circles) and PWIA are from [20].

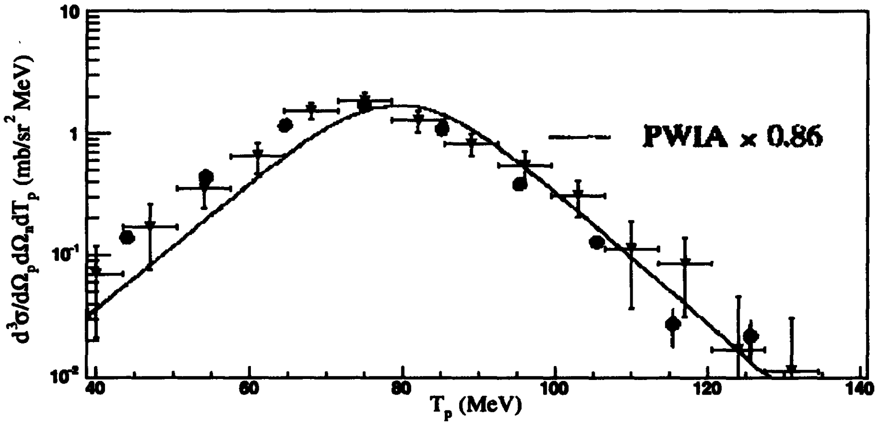

Figure 5-21: Simulated triple differential cross section for quasielastic n–p at 200 MeV with θ_p=45° and θ_n=35° (blue triangles). Experimental data (black circles) and PWIA are from [20].

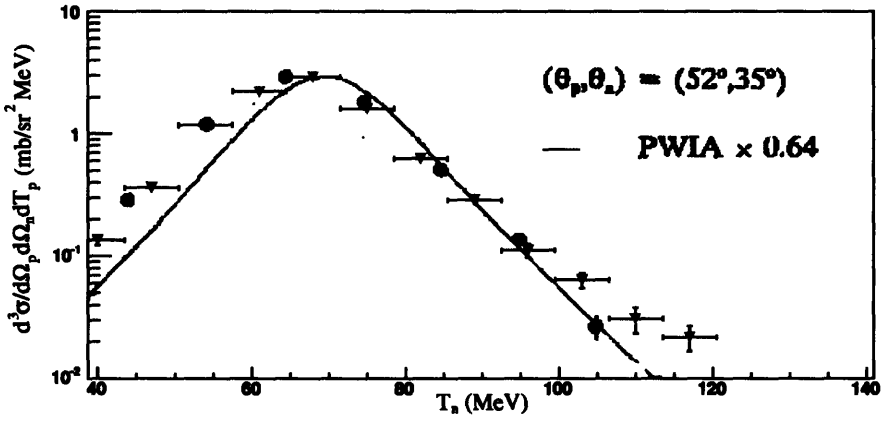

Figure 5-22: Simulated triple differential cross section for quasielastic n–p at 200 MeV with θ_p=36° and θ_n=55° (blue triangles), plotted as a function of scattered neutron kinetic energy, is compared with experimental data (black circles) and PWIA for the $^2\mathrm{H}(\vec{p},pn)$ reaction at 200 MeV with θ_p=52° and θ_n=36°, see [20].

Chapter 6

Cross Section Results

This chapter summarizes the results of the present measurement. The discussion of the sources of systematic uncertainties is followed by the results for the *n–p* and *n–d* differential elastic cross sections. The cross sections are presented as functions of the c.m. angle for beam energies 100 – 300 MeV for the *n–p* and 140 – 240 for the *n–d* measurements in increments of 20 MeV. The *n–p* data are compared to the predictions of the SAID [17] and to the previous measurements where such experimental data exist. The *n–d* data are compared to the previous *p–d* , *n–d* and *d–p* measurements and to the theoretical calculations with and without the contributions of 3NF by Witala *et al.* [5].

6.1 Systematic Errors

Several uncertainties which are summed in quadrature comprise the total systematic error in our measurement. Each source of systematic uncertainty is discussed in turn below.

Incident beam flux. The systematic error in the incident neutron beam flux stems primarily from the uncertainty in the ^{238}U fission cross section at higher energies. While this cross section is known rather precisely at lower energies, there are only two known values in our energy range, see figure 4-8. We estimated the missing values by interpolation. The algorithm used relied on fitting splines to portions of the spectrum. Reference [10] has the details. The close agreement between our results for the elastic *n–p* cross section and the SAID prediction provided justification for this procedure. We estimate that we have a systematic error of 8% in the measurement of the incident beam flux.

Target thickness. The areal target thickness is proportional to the density of liquid deuterium (hydrogen) and the effective thickness of the target flask in the direction of the incident beam. Both of these quantities contain uncertainties. While the nominal density of liquid deuterium (hydrogen) is well known, an uncertainty in this value is introduced by the presence of gas bubbles. During one of the beam-off periods we observed that the liquid inside the target was in a state of constant slow boiling. It looked similar to a glass of champagne. The net effect of gas bubbles is to diminish the effective density of liquid deuterium (hydrogen). After the experiment was completed and the target emptied, we disassembled the vacuum chamber and examined the target flask. We found that the mylar windows of the target flask were permanently deformed (bulged) by the vacuum environment. A comparison of the charged particle detector yields for several liquid hydrogen runs revealed that the deformation of the windows must have been a one-time event which took place at the beginning of the experiment. After that the window geometry, and hence the target thickness, did not change over time as suggested by the stability of the detector yields. The deformation of the windows and the presence of the gas bubbles prevented us from being able to calculate the target thickness. Instead, its value was left as a free parameter of the experiment and was fixed by normalizing our elastic *n–p* cross section at 180 MeV to the SAID fit. The same normalization constant was then applied to the rest of our data.

Neutron detection efficiency. Section 4.2.2 provides the details of the determination of the neutron detection efficiency. According to figure 4-10 the efficiency is a strong function of the detection threshold energy. Moreover, the efficiency of 10% is roughly independent of the incident neutron energy for threshold energy of about 4 MeVee. We artificially kept the value of the neutron detection efficiency at 10% by setting the 4 MeVee software thresholds for all neutron bars. Due to the steep slopes of the efficiency curves in figure 4-10 we estimate that an uncertainty of 0.5 MeV in the threshold energy leads to an uncertainty of up to 20% in the neutron detection efficiency. This, in turn, yields an uncertainty of 5% in the elastic cross section.

Charged particle detection efficiency. The uncertainty in the charged particle detection efficiency is negligible compared to the rest of the errors and was ignored.

Solid angle. While we employed a coincidence method for measuring the elastic *n–d* and *n–p* reactions, the geometry of the neutron wall guaranteed that the solid angles were defined by the charged particle telescopes. The detector positions were measured several times using various references. All measurements were then confirmed using a CAD drawing of the apparatus. The uncertainties in the solid angles which resulted from the uncertainties in the detector positions are negligible compared to the rest of the errors and were ignored.

6.2 *n–p* Elastic Cross Section

The following is the summary of our results for the *n–p* elastic scattering cross section. Our data (full red circles) are compared to the prediction of the SAID for beam energies 100 - 300 MeV in the increments of 20 MeV. In addition, our data are compared to the existing experimental data for 160 and 200 MeV. We observed a good agreement with the SAID fit for all incident beam energies. At lower energies, i.e. 100, 120, and 140 MeV, our results underestimate the SAID prediction at the highest c.m. angle. This is believed to be a manifestation of the energy-dependent neutron detection efficiency; see Chapter 7 for a discussion of this effect.

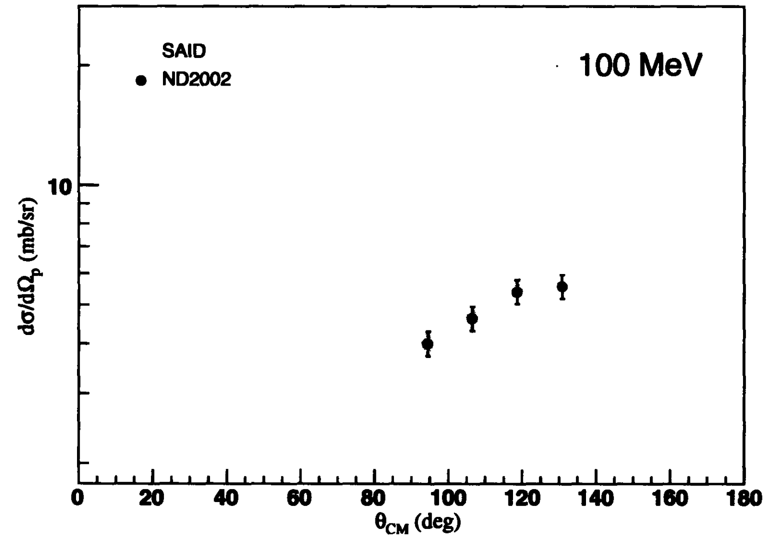

Figure 6-1: *n–p* elastic scattering cross section for 100 MeV incident neutron energy.

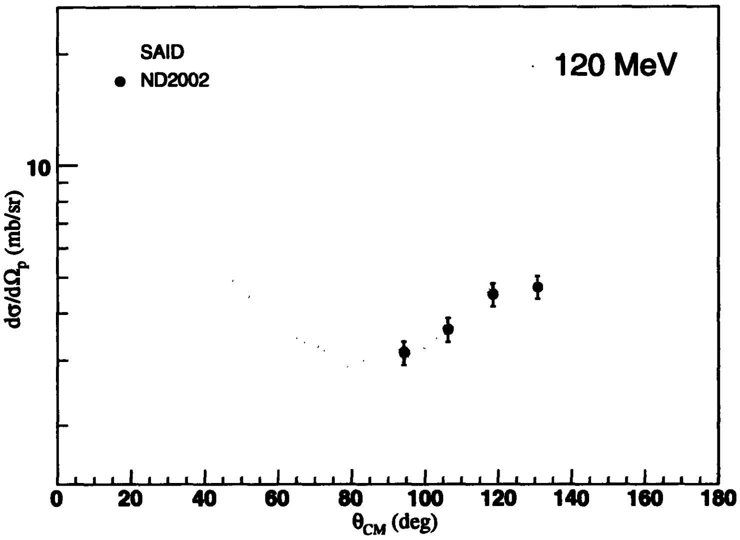

Figure 6-2: *n–p* elastic scattering cross section for 120 MeV incident neutron energy.

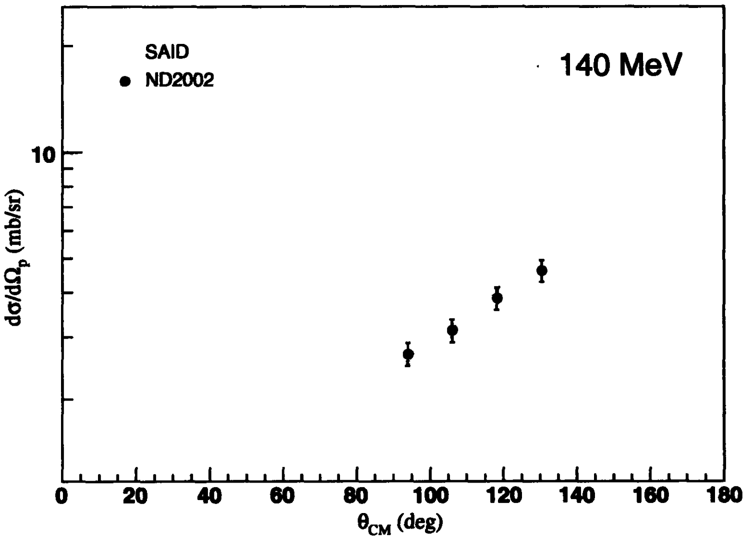

Figure 6-3: *n–p* elastic scattering cross section for 140 MeV incident neutron energy.

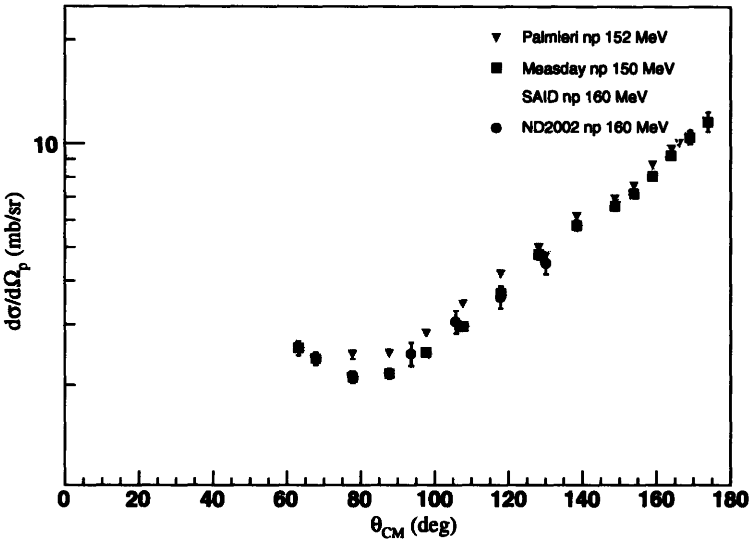

Figure 6-4: n–p elastic scattering cross section for 160 MeV incident neutron energy.

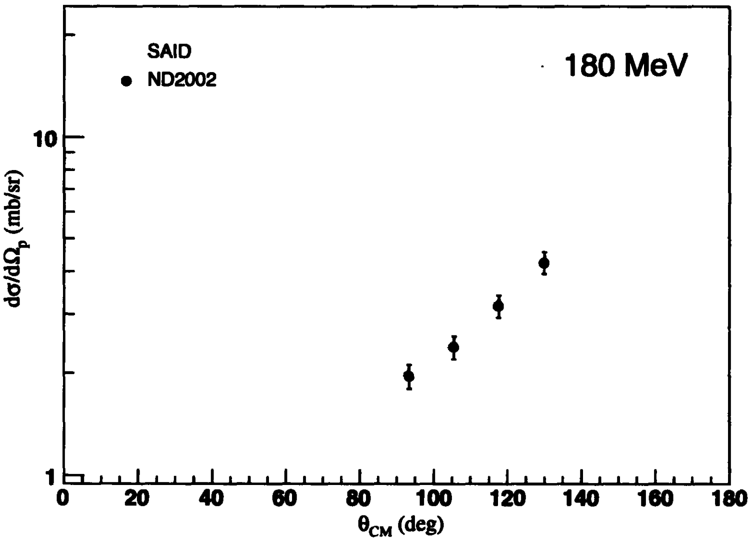

Figure 6-5: n–p elastic scattering cross section for 180 MeV incident neutron energy.

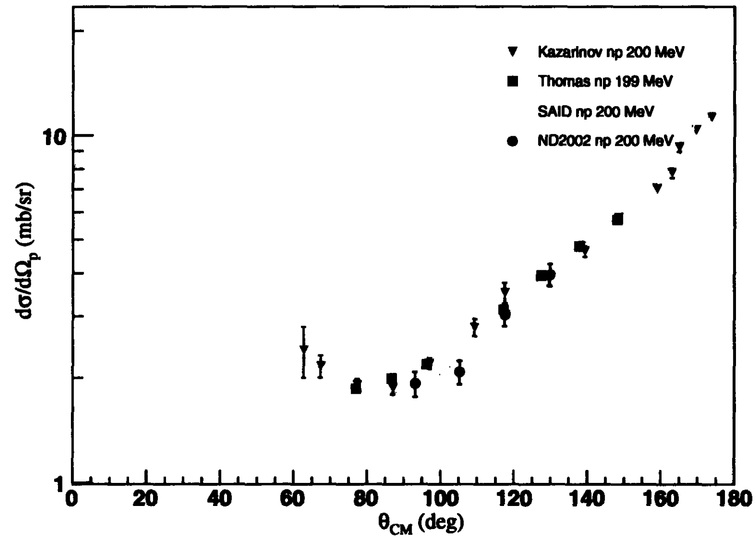

Figure 6-6: n–p elastic scattering cross section for 200 MeV incident neutron energy.

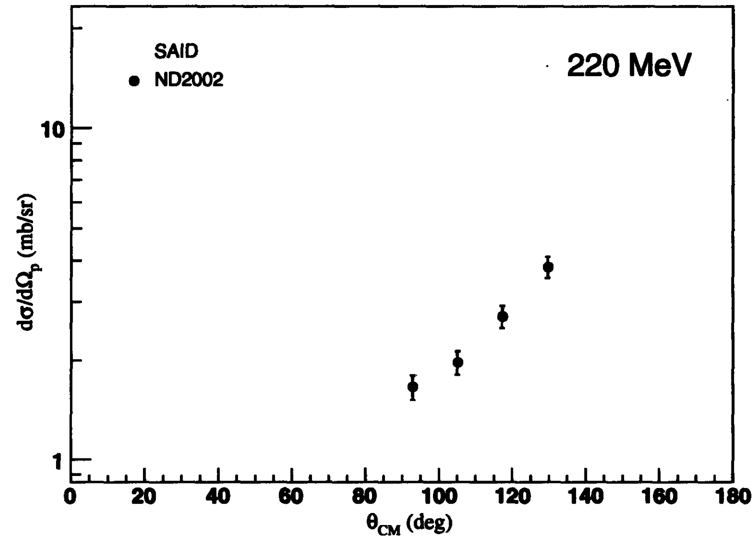

Figure 6-7: n–p elastic scattering cross section for 220 MeV incident neutron energy.

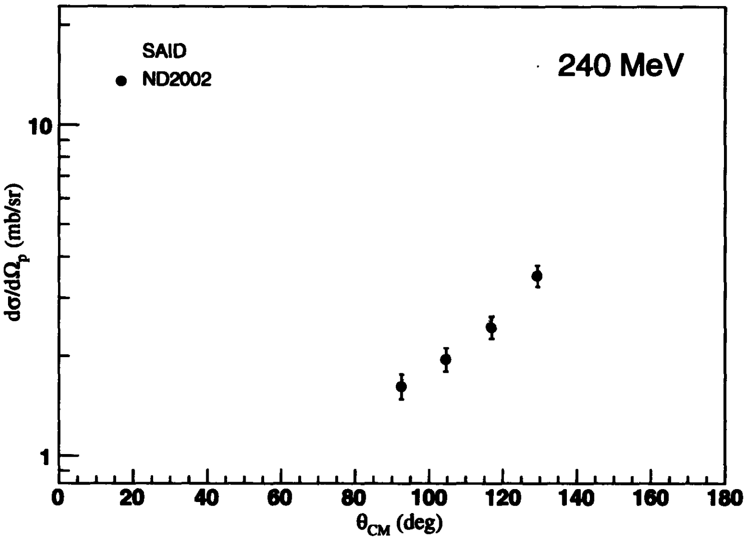

Figure 6-8: n–p elastic scattering cross section for 240 MeV incident neutron energy.

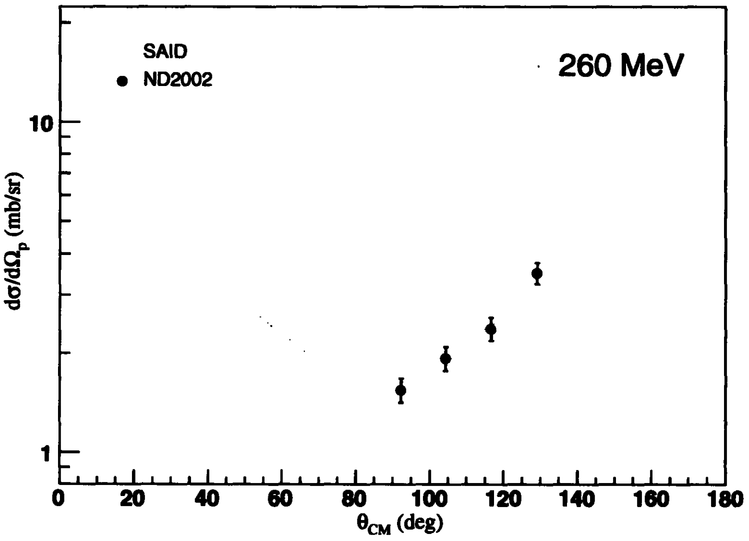

Figure 6-9: n–p elastic scattering cross section for 260 MeV incident neutron energy.

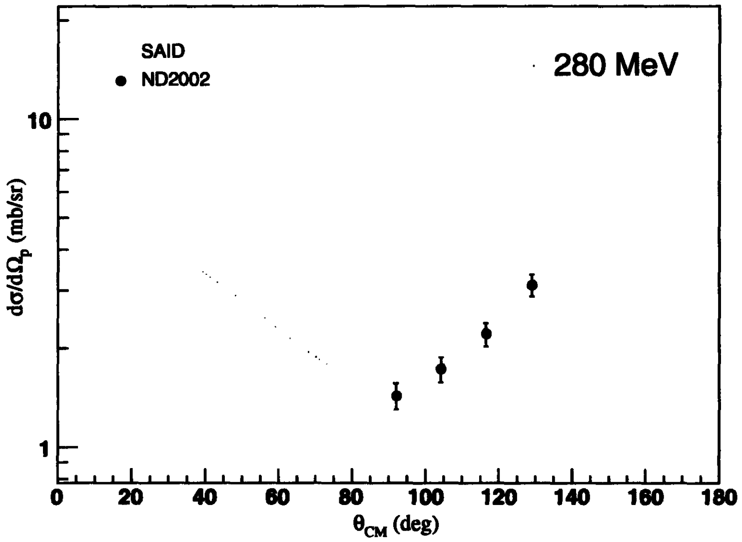

Figure 6-10: *n*–*p* elastic scattering cross section for 280 MeV incident neutron energy.

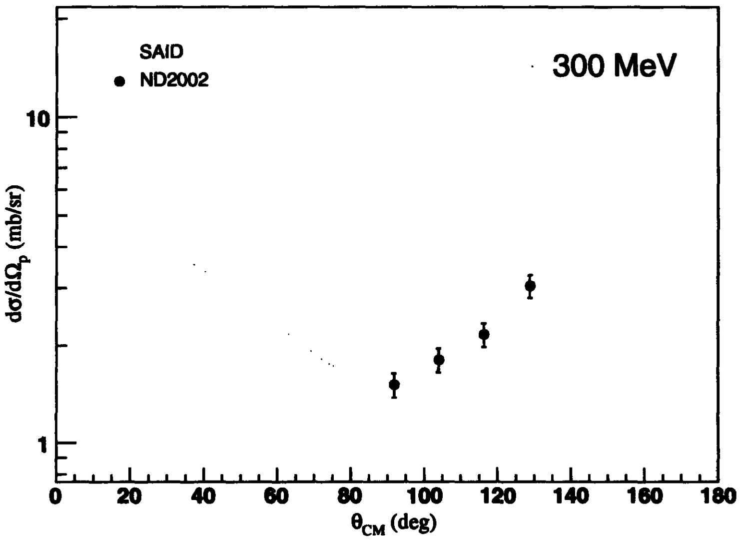

Figure 6-11: *n*–*p* elastic scattering cross section for 300 MeV incident neutron energy.

θ_{lab} (deg)	θ_{CM} (deg)	$(d\sigma/d\Omega)$ (mb/sr)	$\Delta(d\sigma/d\Omega)$ (mb/sr)
130.9	24.0	5.566	0.380
118.7	30.0	5.398	0.370
106.6	36.0	4.627	0.330
94.5	42.0	4.004	0.290

Table 6.1: *n–p* elastic scattering cross section at 100 MeV

θ_{lab} (deg)	θ_{CM} (deg)	$(d\sigma/d\Omega)$ (mb/sr)	$\Delta(d\sigma/d\Omega)$ (mb/sr)
130.7	24.0	4.702	0.330
118.5	30.0	4.492	0.320
106.3	36.0	3.624	0.260
94.2	42.0	3.138	0.230

Table 6.2: *n–p* elastic scattering cross section at 120 MeV

θ_{lab} (deg)	θ_{CM} (deg)	$(d\sigma/d\Omega)$ (mb/sr)	$\Delta(d\sigma/d\Omega)$ (mb/sr)
130.4	24.0	4.608	0.330
118.2	30.0	3.845	0.280
106.0	36.0	3.119	0.230
93.9	42.0	2.676	0.200

Table 6.3: *n–p* elastic scattering cross section at 140 MeV

θ_{lab} (deg)	θ_{CM} (deg)	$(d\sigma/d\Omega)$ (mb/sr)	$\Delta(d\sigma/d\Omega)$ (mb/sr)
130.2	24.0	4.506	0.320
117.9	30.0	3.601	0.260
105.8	36.0	3.056	0.230
93.7	42.0	2.466	0.190

Table 6.4: *n–p* elastic scattering cross section at 160 MeV

θ_{lab} (deg)	θ_{CM} (deg)	$(d\sigma/d\Omega)$ (mb/sr)	$\Delta(d\sigma/d\Omega)$ (mb/sr)
130.0	24.0	3.825	0.280
117.7	30.0	3.387	0.250
105.5	36.0	2.505	0.190
93.4	42.0	1.969	0.160

Table 6.5: *n–p* elastic scattering cross section at 180 MeV

θ_{lab} (deg)	θ_{CM} (deg)	$(d\sigma/d\Omega)$ (mb/sr)	$\Delta(d\sigma/d\Omega)$ (mb/sr)
129.8	24.0	3.963	0.290
117.5	30.0	3.037	0.230
105.2	36.0	2.074	0.160
93.1	42.0	1.922	0.160

Table 6.6: *n–p* elastic scattering cross section at 200 MeV

θ_{lab} (deg)	θ_{CM} (deg)	$(d\sigma/d\Omega)$ (mb/sr)	$\Delta(d\sigma/d\Omega)$ (mb/sr)
129.6	24.0	3.824	0.280
117.2	30.0	2.709	0.210
105.0	36.0	1.973	0.160
92.8	42.0	1.664	0.140

Table 6.7: *n–p* elastic scattering cross section at 220 MeV

θ_{lab} (deg)	θ_{CM} (deg)	$(d\sigma/d\Omega)$ (mb/sr)	$\Delta(d\sigma/d\Omega)$ (mb/sr)
129.4	24.0	3.504	0.260
117.0	30.0	2.449	0.190
104.7	36.0	1.959	0.160
92.6	42.0	1.621	0.140

Table 6.8: *n–p* elastic scattering cross section at 240 MeV

θ_{lab} (deg)	θ_{CM} (deg)	$(d\sigma/d\Omega)$ (mb/sr)	$\Delta(d\sigma/d\Omega)$ (mb/sr)
129.2	24.0	3.491	0.260
116.7	30.0	2.369	0.190
104.4	36.0	1.930	0.160
92.3	42.0	1.544	0.130

Table 6.9: *n–p* elastic scattering cross section at 260 MeV

θ_{lab} (deg)	θ_{CM} (deg)	$(d\sigma/d\Omega)$ (mb/sr)	$\Delta(d\sigma/d\Omega)$ (mb/sr)
129.0	24.0	3.119	0.240
116.5	30.0	2.210	0.180
104.2	36.0	1.728	0.150
92.0	42.0	1.434	0.130

Table 6.10: *n–p* elastic scattering cross section at 280 MeV

θ_{lab} (deg)	θ_{CM} (deg)	$(d\sigma/d\Omega)$ (mb/sr)	$\Delta(d\sigma/d\Omega)$ (mb/sr)
128.8	24.0	3.032	0.240
116.3	30.0	2.153	0.180
103.9	36.0	1.801	0.150
91.8	42.0	1.513	0.130

Table 6.11: *n–p* elastic scattering cross section at 300 MeV

6.3 *n–d* Elastic Cross Section

The following is a summary of our results (full red circles) for the *n–d* elastic scattering cross section for incident beam energies of 140 - 240 MeV in the increments of 20 MeV. Our data are compared to the existing data for the *n–d* , *p–d* , and *d–p* scattering and to the theoretical predictions by Witala *et al.* [5] at 140 and 200 MeV.

At 140 MeV our data are in good agreement with several existing data sets, including the data from Sakai *et al.* [6] (blue squares). Our cross section is consistently lower than that reported by Ermisch *et al.* [7] (black open circles). At this energy, our data agree consistently with the theoretical prediction which includes the contribution of the TM 3NF (green solid line).

At 200 MeV our data are in agreement with the existing data sets for *p–d* and *d–p* scattering, although our cross section is consistently lower than the *p–d* data reported by Ermisch *et al.* [7] (stars). Our data favor the theoretical prediction which includes the contribution of the TM 3NF (green solid line) for c.m. angles below about 120 degrees. Above this range the theory significantly underestimates all of the experimental results.

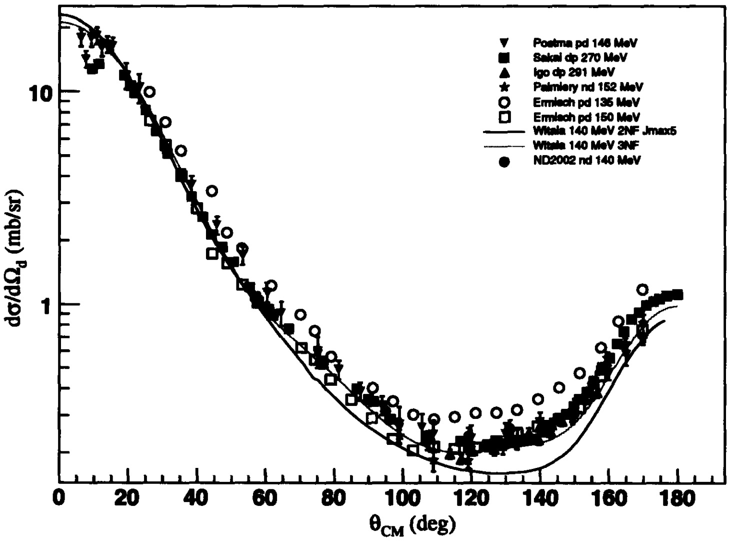

Figure 6-12: *n–d* elastic scattering cross section for 140 MeV incident neutron energy.

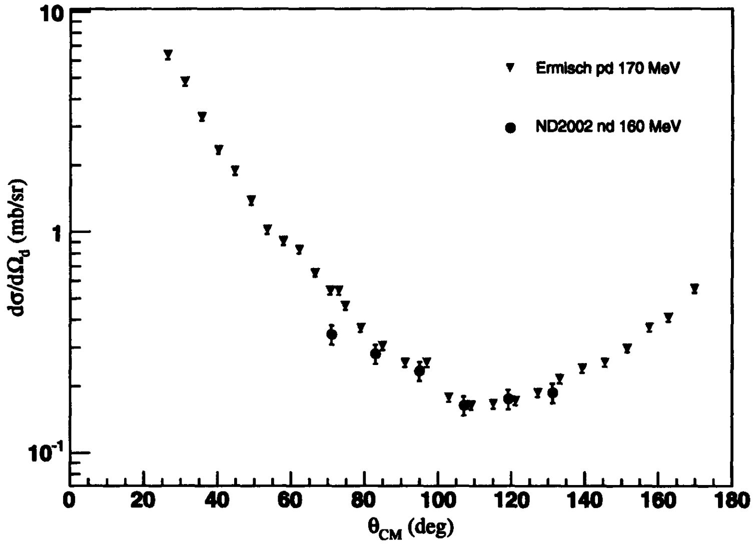

Figure 6-13: *n–d* elastic scattering cross section for 160 MeV incident neutron energy.

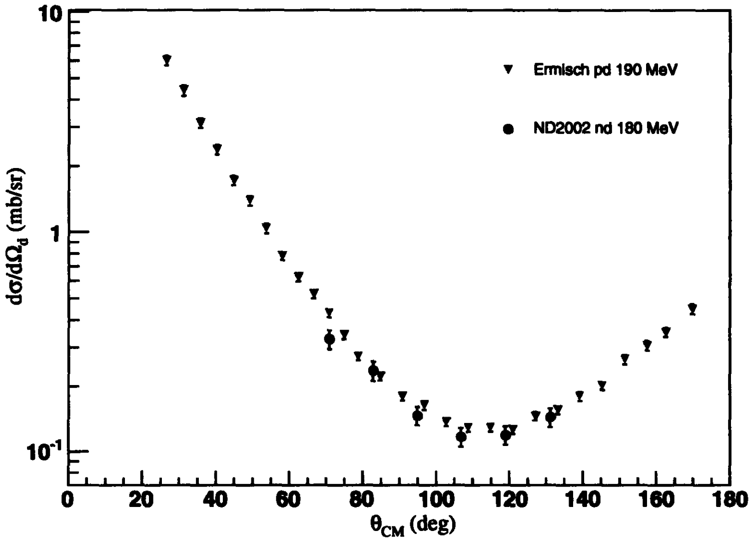

Figure 6-14: *n–d* elastic scattering cross section for 180 MeV incident neutron energy.

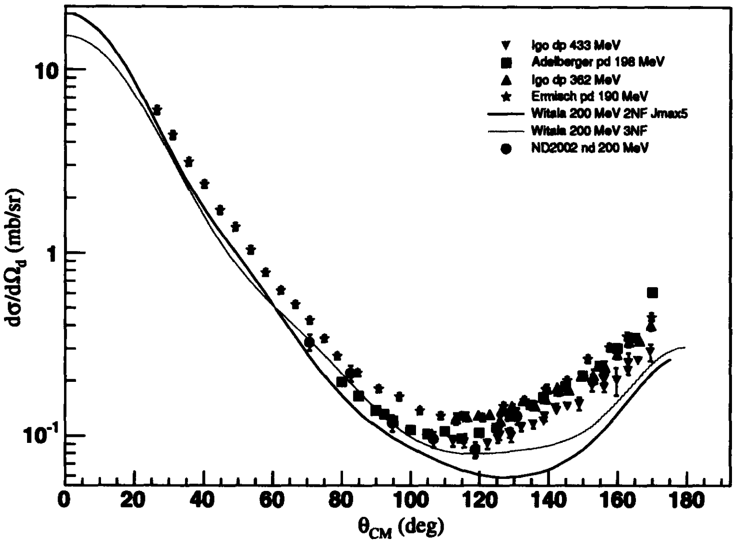

Figure 6-15: *n–d* elastic scattering cross section for 200 MeV incident neutron energy.

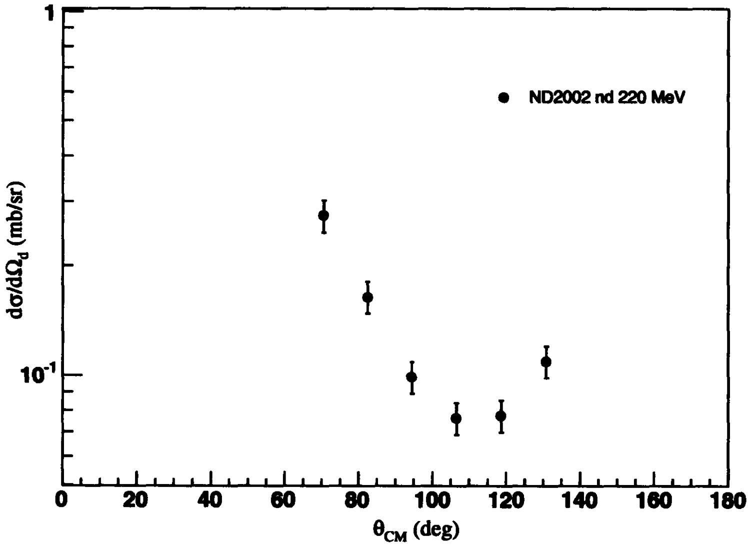

Figure 6-16: *n–d* elastic scattering cross section for 220 MeV incident neutron energy.

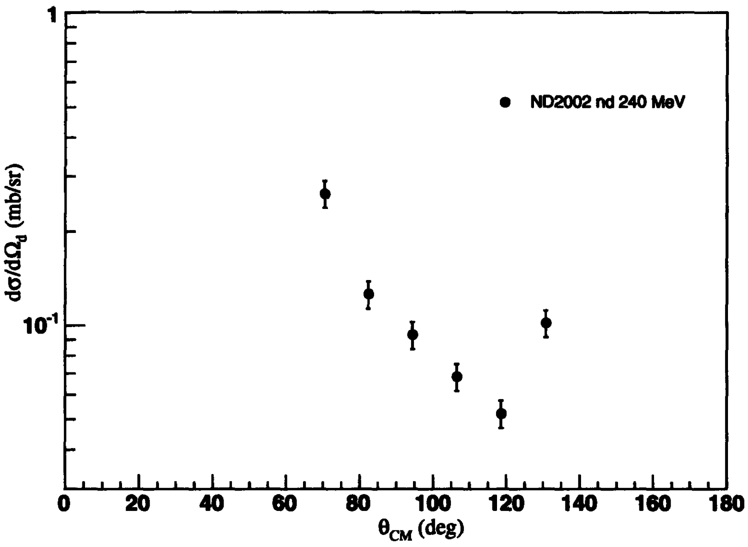

Figure 6-17: *n–d* elastic scattering cross section for 240 MeV incident neutron energy.

θ_{lab} (deg)	θ_{CM} (deg)	$(d\sigma/d\Omega)$ (mb/sr)	$\Delta(d\sigma/d\Omega)$ (mb/sr)
131.3	24.0	0.260	0.026
119.2	30.0	0.239	0.024
107.1	36.0	0.229	0.023
95.1	42.0	0.313	0.031

Table 6.12: *n–d* elastic scattering cross section at 140 MeV

θ_{lab} (deg)	θ_{CM} (deg)	$(d\sigma/d\Omega)$ (mb/sr)	$\Delta(d\sigma/d\Omega)$ (mb/sr)
131.2	24.0	0.187	0.019
119.1	30.0	0.175	0.017
107.0	36.0	0.164	0.016
94.9	42.0	0.234	0.023
82.9	48.0	0.280	0.028
71.0	54.0	0.344	0.034

Table 6.13: *n–d* elastic scattering cross section at 160 MeV

θ_{lab} (deg)	θ_{CM} (deg)	$(d\sigma/d\Omega)$ (mb/sr)	$\Delta(d\sigma/d\Omega)$ (mb/sr)
131.1	24.0	0.144	0.014
118.9	30.0	0.119	0.012
106.8	36.0	0.117	0.012
94.8	42.0	0.146	0.015
82.8	48.0	0.235	0.023
70.9	54.0	0.327	0.033

Table 6.14: *n–d* elastic scattering cross section at 180 MeV

θ_{lab} (deg)	θ_{CM} (deg)	$(d\sigma/d\Omega)$ (mb/sr)	$\Delta(d\sigma/d\Omega)$ (mb/sr)
131.0	24.0	0.128	0.013
118.8	30.0	0.084	0.008
106.7	36.0	0.096	0.010
94.7	42.0	0.117	0.012
82.7	48.0	0.220	0.022
70.7	54.0	0.325	0.033

Table 6.15: *n–d* elastic scattering cross section at 200 MeV

θ_{lab} (deg)	θ_{CM} (deg)	$(d\sigma/d\Omega)$ (mb/sr)	$\Delta(d\sigma/d\Omega)$ (mb/sr)
130.9	24.0	0.109	0.011
118.7	30.0	0.078	0.008
106.6	36.0	0.076	0.008
94.5	42.0	0.099	0.010
82.5	48.0	0.165	0.016
70.6	54.0	0.275	0.027

Table 6.16: *n–d* elastic scattering cross section at 220 MeV

θ_{lab} (deg)	θ_{CM} (deg)	$(d\sigma/d\Omega)$ (mb/sr)	$\Delta(d\sigma/d\Omega)$ (mb/sr)
130.8	24.0	0.102	0.010
118.6	30.0	0.052	0.005
106.5	36.0	0.068	0.007
94.4	42.0	0.093	0.009
82.4	48.0	0.126	0.013
70.5	54.0	0.264	0.026

Table 6.17: *n–d* elastic scattering cross section at 240 MeV

Chapter 7

Summary and Discussion

The neutron-deuteron elastic scattering process provides an important probe of the effect of three-nucleon forces (3NF) in the nucleon few-body problem. Its popularity rests on the fact that the scattering observables are accessible both theoretically and experimentally. Recent work by Witala *et al.* [5] includes calculations with and without the 3NF contributions for the *n–d* differential scattering cross sections at medium incident energies. The comparisons of these calculations with the available *p–d* and *d–p* data have shown that the inclusion of the three-nucleon force effects drastically improves the agreement between the theory and the experimental data in the regions of cross section minima. However, the calculations do not yet include the contributions of the Coulomb interactions and it is unclear if the remaining disagreement between the theory and the experiment, see figure 6-12, points to this omission of the Coulomb effects or is an indication that modern two- and three-nucleon potentials are still lacking the descriptions of important dynamics. Additionally, two of the most recent experimental measurements [6] and [7] disagree with each other.

To help resolve these questions we measured the *n–d* elastic scattering cross section at several c.m. angles for a range of incident beam energies. While our results are in closer agreement with the results from Sakai *et al.* [6] and in general appear to be quite definitive, there are several aspects which can be improved further to increase our confidence in our measurement.

The most important issue to be addressed is the precise calculation of the neutron detection efficiency for the neutron bar detectors. As was described in the analysis section of this paper, we used the value of 10% for the efficiency at all incident neutron energies. This was permissible because of the unique characteristic of the neutron bars. Namely, the efficiency stayed constant at roughly 10% independent of the incident neutron energy, provided that the threshold energy of each bar was set at 4 MeVee, see figure 4-10. However, the same figure reveals that the efficiency is constant only for a limited range of incident neutron energies, e.g. 120 – 160 MeV. Calculations show that during the n–d elastic measurement the actual energy range of the neutrons incident on the neutron wall was broader than the one permitted by the assumption of the energy-independent efficiency (i.e. 35 – 146 MeV). An uncertainty of as much as 20% in the neutron detection efficiency can be eliminated by using a more precise calculation of the efficiency.

Another unresolved issue is the question of the deuteron break-up in the target volume. There is a finite probability that a recoil deuteron will break up in the target, never reaching the charged particle telescope. According to a preliminary investigation such probability is low. Yet, this effect can manifest itself in two ways. First, it alters the charged particle detection efficiency. Even if, following a deuteron break-up, its constituent nucleon is detected in one of the telescopes, such an event will most likely be rejected by the kinematic cuts on the grounds of unrecognizable kinematics. Second, the quasi-elastic protons which result from such break-ups will contribute to the overall background and have to be identified and subtracted from the final results. A cleanly separable deuteron locus in figure 4-20 suggests that the number of such background events which pass all applied kinematic constraints is low.

Finally, it is still a mystery why the cosmic ray TOF_{left} - TOF_{right} spectra are not smooth but show a periodic structure, see figure 3-9. So far, everything seems to incriminate our measuring electronics. An effect such as electronic cross-talk or signal reflections can potentially create such a result. During the investigation we considered ideas such as optical reflections in the scintillator bars and timing inconsistencies due to multiple internal reflections of the scintillation light. These did not prove to be sufficient by themselves to be responsible for the observed bumpiness of the time-difference spectra. Special attention should be paid to avoid similar behavior in future experiments which utilize similar neutron detectors and electronics.

While the above named effects still await their resolution, this measurement of the n–d elastic scattering cross section yielded valuable data which will help to constrain present and future theoretical work related to the 3NF effects in few-nucleon systems.

Appendix A

Range tables

The results for computed proton and deuteron ranges in various materials are included here for completeness.

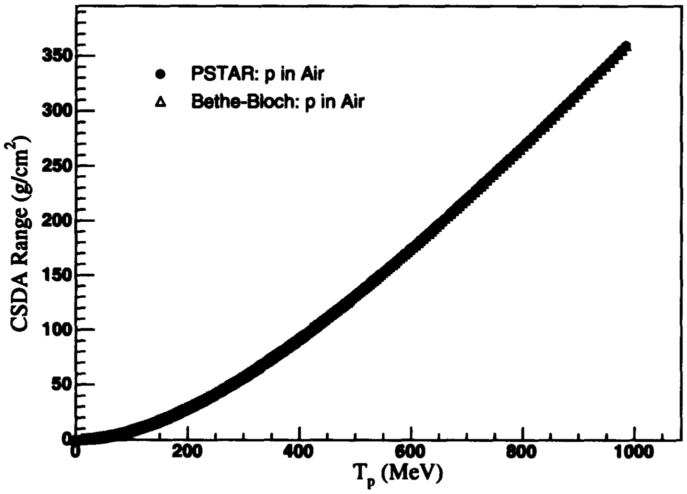

Figure A-1: Proton CSDA range in air.

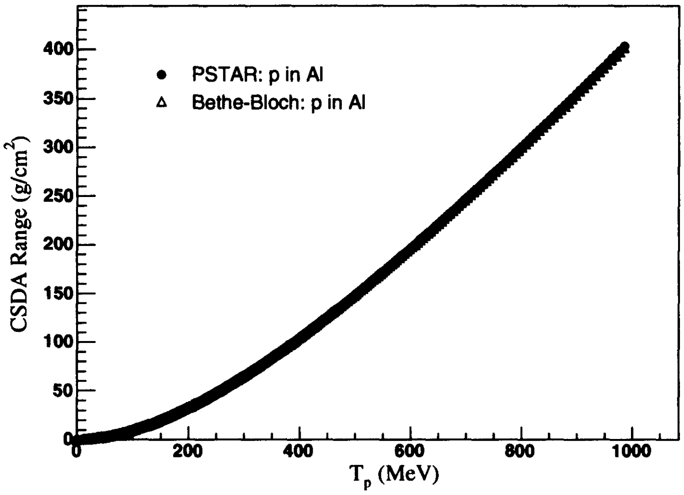

Figure A-2: Proton CSDA range in aluminum.

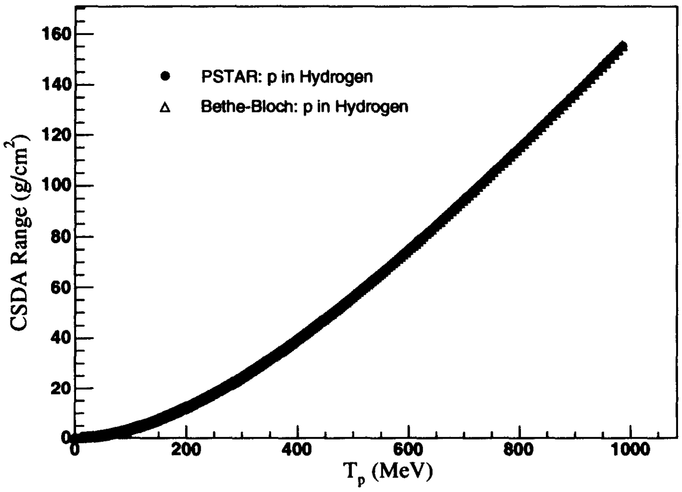

Figure A-3: Proton CSDA range in hydrogen.

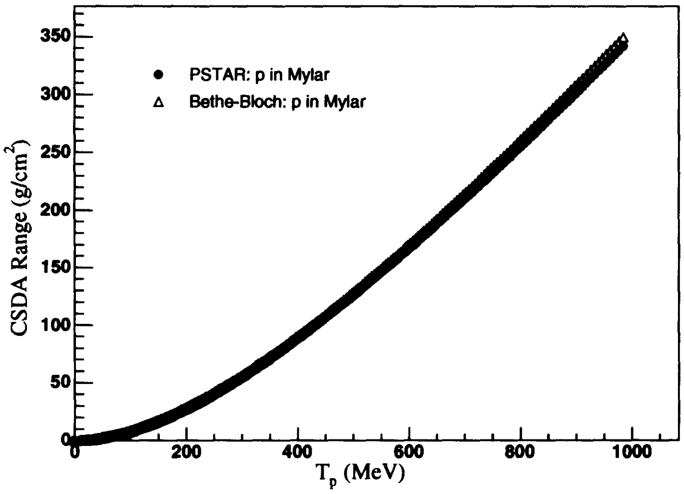

Figure A-4: Proton CSDA range in mylar.

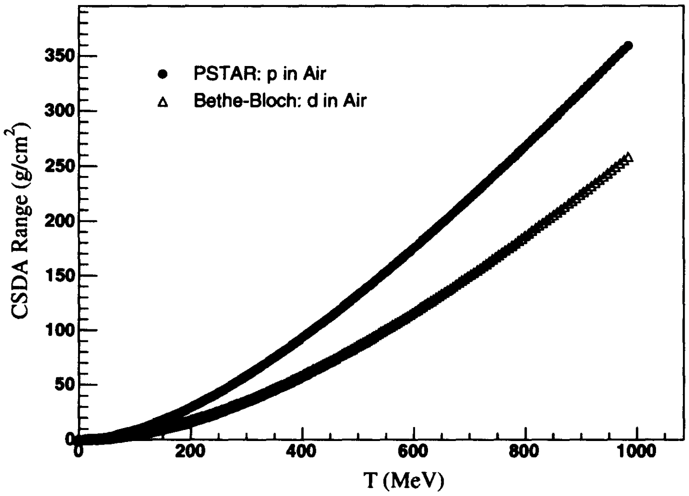

Figure A-5: Deuteron CSDA range in air.

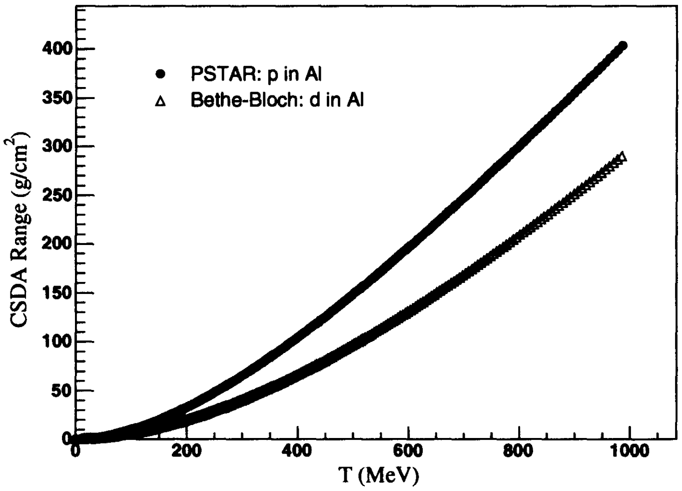

Figure A-6: Deuteron CSDA range in aluminum.

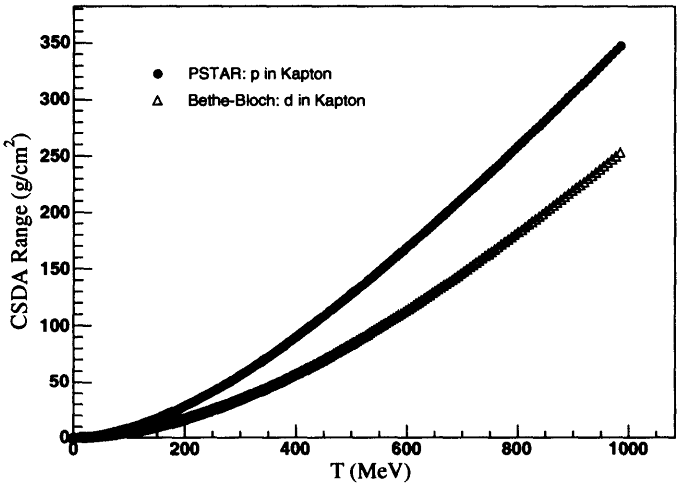

Figure A-7: Deuteron CSDA range in kapton.

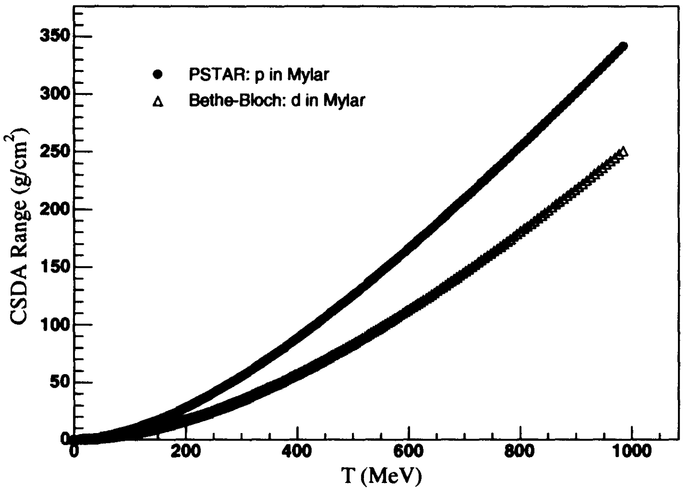

Figure A-8: Deuteron CSDA range in mylar.

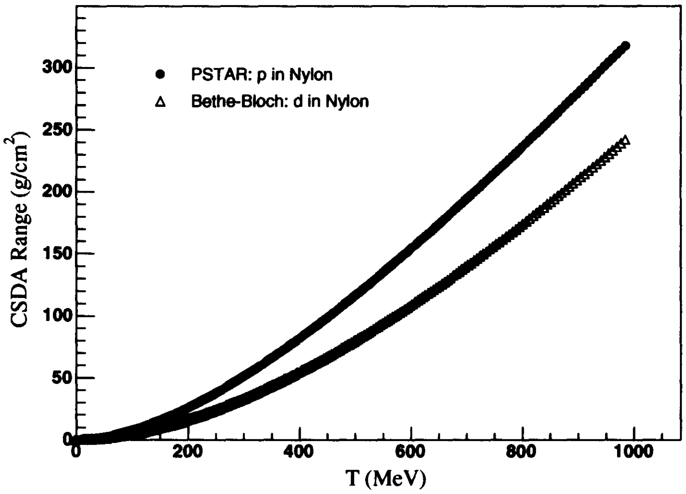

Figure A-9: Deuteron CSDA range in nylon.

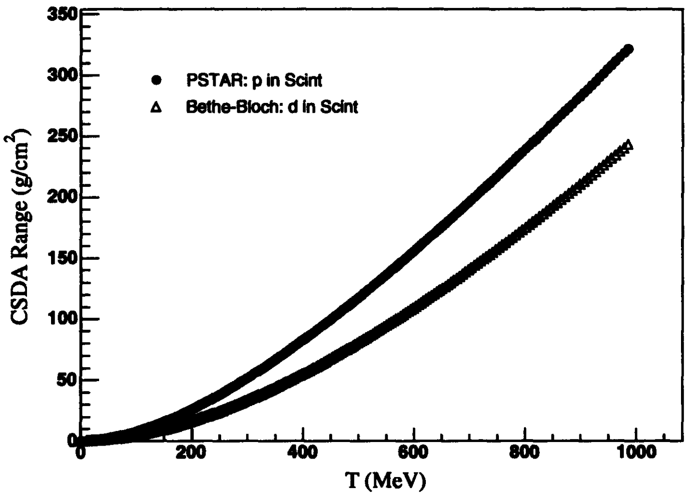

Figure A-10: Deuteron CSDA range in plastic scintillator (vinyltoluene-based).

Bibliography

[1] J. Carlson and R. Schiavilla. "Structure and dynamics of few-nucleon systems," *Reviews of Modern Physics*, **70**(3), 743 (1998).

[2] J. Fujita and H. Miyazawa *Prog. Theor. Phys.*, **17**, 360 (1957).

[3] S. Coon and M. Peña. "Momentum and coordinate space three-nucleon potentials," *Physical Review C*, **48**, 2559 (1993).

[4] B. Pudliner *et al.* "Quantum Monte Carlo calculations of nuclei with A<7," *Physical Review C*, **56**, 1720 (1997).

[5] H. Witala *et al.* "Cross section minima in elastic *nd* scattering: possible evidence for three-nucleon force effects," *Physical Review Letters*, **81**, 1183–1186 (1998).

[6] H. Sakai *et al.* "Precise measurement of *d–p* elastic scattering at 270 MeV and three-nucleon force effects," *Physical Review Letters*, **84**(23), 5288–5291 (2000).

[7] K. Ermisch *et al.* "Systematic investigation of the elastic proton-deuteron differential cross section at intermediate energies," *Physical Review C*, **68**, 051001 (2003).

[8] H. Postma and R. Wilson. "Elastic scattering of 146-MeV polarized protons by deuterons," *Physical Review*, **121**(4), 1229 (1961).

[9] R. Adelberger and C. Brown. "*p–d* elastic cross section and polarization at 198 MeV," *Physical Review D*, **5**(9), 2139 (1972).

[10] T. Akdoğan. *Pion production in the neutron-proton interaction.* PhD thesis, M.I.T., 2003.

[11] S. A. Wender, S. Balestrini, A. Brown, R. C. Haight, C. M. Layman, T. M. Lee, P. W. Lisowski, W. McCorkle, R. O. Nelson, and W. Parker. "A fission ionization detector for neutron flux measurements at a spallation source," *Nuclear Intrumentation and Methods in Physics Research A*, **336**, 226–231 (1993).

[12] C. Jiang. *A precision measurement of neutron-neutron scattering length a_{nn} via $\pi^- d \to \gamma nn$.* PhD thesis, University of Kentucky, 1996.

[13] M. Kovash. Private communication.

[14] Kazarinov *et al.* "finish this entry: np 200 MeV,".

[15] Thomas *et al.* "finish this entry: np 199 MeV," *PR*, **167**, 1240(68).

[16] R. Czyzykiewicz *et al.* "Dependence of the excess energy distribution for the quasi-free $pn \to pnpn\nu'$ reaction on the deuteron wave function model," *Nuclear Intrumentation and Methods in Physics Research A*, **336**, 226–231 (1993).

[17] R. A. Arndt, L. D. Roper, and R. L. Workman. "Nucleon-nucleon partial-wave analysis to 1.6 GeV," *Physical Review D*, **45**(11), 3995–4001 (1992).

[18] http://physics.nist.gov/PhysRefData/Star/Text/PSTAR.html.

[19] http://pdg.lbl.gov/1998/passagerppbook.pdf.

[20] W. Pairsuwan *et al.* "Analyzing powers for the $^2\mathrm{H}(\vec{p}, pn)^1\mathrm{H}$ reaction at 200 MeV," *Physical Review C*, **52**, 2552–2558 (1995).